

**Physics Sensitivity
Studies
at the ICAL detector**

By

Animesh Chatterjee

Enrolment Number : PHYS01200904011

Bhabha Atomic Research Centre, Mumbai

*A thesis submitted to the
Board of Studies in Physical Sciences
In partial fulfillment of the requirements
for the Degree of
DOCTOR OF PHILOSOPHY*

of

HOMI BHABHA NATIONAL INSTITUTE



September 2014

STATEMENT BY AUTHOR

This dissertation has been submitted in partial fulfillment of requirements for an advanced degree at Homi Bhabha National Institute (HBNI) and is deposited in the Library to be made available to borrowers under rules of the HBNI.

Brief quotations from this dissertation are allowable without special permission, provided that accurate acknowledgement of source is made. Requests for permission for extended quotation from or reproduction of this manuscript in whole or in part may be granted by the Competent Authority of HBNI when in his or her judgment the proposed use of the material is in the interests of scholarship. In all other instances, however, permission must be obtained from the author.

Date:

Animesh Chatterjee

(PhD Candidate)

DECLARATION

I, hereby declare that the investigation presented in the thesis has been carried out by me. The work is original and has not been submitted earlier as a whole or in part for a degree / diploma at this or any other Institution / University.

Date:

Animesh Chatterjee
(PhD Candidate)

List of Publications arising from the thesis

Journal

1. "A Simulations Study of the Muon Response of the Iron Calorimeter Detector at the India-based Neutrino Observatory", A. Chatterjee, K. K. Meghna, K. Rawat, T. Thakore, V. Bhatnagar, R. Gandhi, D. Indumathi and N. K. Mondal *et al.*, JINST 9 (2014) P07001 [arXiv:1405.7243]
2. "Octant sensitivity for large θ_{13} in atmospheric and long baseline neutrino experiments.", Animesh Chatterjee, Pomita Ghoshal, Srubabati Goswami, Sushant K. Raut, JHEP 1305 (2013) 010,[arXiv:1302.1370] [hep-ph]
3. "Probing Lorentz and CPT Violation in a Magnetized Iron Detector using Atmospheric Neutrinos", A. Chatterjee, R. Gandhi, J. Singh, JHEP 1406 (2014) 045 [arXiv:1402.6265][hep-ph]
4. "Testing non-standard neutrino matter interactions in atmospheric neutrino propagation", A. Chatterjee, D. Choudhury, R. Gandhi, P. Mehta, [arXiv:1409.8472]

Conferences

- "Study of CPT violation using ICAL detector", Proceedings of the XX DAE-BRNS High Energy Physics Symposium, Visva Bharati, January 2013

List of other publications of candidate not related to this thesis

1. "Configuring the Long-Baseline Neutrino Experiment" V. Barger, A. Bhattacharya, A. Chatterjee, R. Gandhi, D. Marfatia, M. Masud, Phys. Rev. D 89, 011302 (2014)
2. "Configurations of the Long-Baseline Neutrino Experiment", V. Barger, A. Bhattacharya, A. Chatterjee, R. Gandhi, D. Marfatia, M. Masud, arXiv:1405.1054[hep-ph]
3. "Probing CP violation with the first ultra-high energy neutrinos from IceCube", A. Chatterjee, M. M. Devi, M. Ghosh, R. Moharana, S. K. Raut, arXiv:1312.6593[hep-ph]

Date:

Animesh Chatterjee
(PhD Candidate)

**Dedicated to
to my parents**

Acknowledgments

I would like to thank my supervisor Prof. Raj Gandhi, for the excellent guidance, great support and advice he has provided throughout my PhD life. I have been extremely lucky to have a supervisor who cared so much not only about my work, but also the complete journey of my PhD life.

It gives me immense pleasure to thank my collaborators who helped and taught me. I would like to thank Prof. Vernon Barger, Prof. N.K. Mondal, Dr. Danny Marfatia, Prof. D. Indumathi, Prof. Debajyoti Choudhury, Prof. Nita Sinha, Dr. Jyotsna Singh, Prof. Vipin Bhatnagar, Sushant Raut, Moon Moon Devi, Monojit Ghosh, Reetanjali Maharana, Mehedi Masud, Meghna K.K, Tarak Thakore, Kanishka Rawat. I would specially like to thank Dr. Srubabati Goswami, Pomita Ghoshal, Poonam Mehta and Atri Bhattacharya who have given their enormous support and suggestion all the time.

I would also like to thank Prof. Amitava Raychaudhuri, Prof. Murthy, Dr. Amol Dighe, Dr. Uma Shankar, Dr. Sandhya Choubey for their useful comments and suggestions. I would like to express my deepest gratitude to Prof. Gobinda Majumdar, Prof. Vivek Datar, Dr. Satyanarayana, Prof. Vandana Nanal, Prof. Pilley, Prof. Sudeshna Banerjee, Dr. L.M. Pant for their contribution in my journey till now starting from the graduate training period at TIFR.

I must express my sincere gratitude to Prof. Naba Kumar Mondal, the Director of the India-Based Neutrino Observatory who gave me continuous support during the time of my entire work. Also, a big thanks to all INO collaboration members for their consistent help.

I have spent an excellent year at TIFR during my course work. I would like to thank Tarak, Sumanata, Vivek, Nitali, Sudeshna, Deepak Samuel, Kolahal, Tamali, Neha, Sourabh, Mathi, Lakshmi, Thiru, Maulik, Salim, Varchaswi, Rabindra, Rajesh, Ali, Abhik. A special thanks to Moon Moon and Meghna for helping me to this entire journey.

Next, the turn for HRI, where I have spent one of the most beautiful time of my life. I want to thank all the professors for the discussions and clarifications. My wholehearted thanks to Atri da, Anushree di and Shankha for their kind help all the time. I want to thank all of you for the beautiful days I have spent here for the last four years. Thanks Niyogi da, Hochi, Rana, Dibya, Aritra, Masud, Shrobona, Nabarun, Titas, Rambha, Arghya da, Arindam da, Anirban da, Taushif, Sauri, Arijit, Manoj, Deepak, Suprabh,

ACKNOWLEDGMENTS

Tarat da, Paromita di, Tanumoy da, Madhumita di, Jonthu da, Ushoshi, Jaydip, Satendra.

I would like to acknowledge the financial, and technical support of INO without which my PhD. was not possible. Thanks to all the non-academic staff of HRI, TIFR, INO, who are giving their best.

To my closer friends, I would like to thank Dipannita, Mayukh and Kausik for the friendship and support.

Last but not the least, I would like to thank my family, my parents for their unconditional support, love and encouragement, without which I would not have come this far.

Contents

Synopsis	1
List of Figures	4
List of Tables	9
1 Introduction	11
1.1 History of Neutrinos	12
1.2 Sources of Neutrinos	13
1.3 Neutrino Oscillations	15
1.3.1 Neutrino Oscillations in vacuum	17
1.3.2 Neutrino Oscillations in matter	19
1.4 Present status of neutrino parameters	26
1.4.1 Open challenges in oscillations physics	27
1.5 Beyond neutrino oscillations	29
1.5.1 Lorentz Invariance Violation / CPT Violation	29
1.5.2 Non standard neutrino interactions	30
1.6 An overview of the thesis	35
2 ICAL@INO	37
2.1 The physics motivation of ICAL@INO	37
2.2 ICAL Detector Geometry	39
2.3 The active detector element RPC	40
2.3.1 Principle of operation	40
2.4 Gas system	42
2.5 Readout system	43

2.5.1	Electronic readout system	43
3	Simulation of ICAL for muons	45
3.1	Simulation Framework	46
3.1.1	Track finding	46
3.1.2	Track fitting	47
3.2	Response of ICAL to muons	48
3.2.1	Momentum resolution	48
3.2.2	Zenith angle resolution	50
3.2.3	Reconstruction efficiency	50
3.2.4	Relative charge identification efficiency	52
4	Octant sensitivity at ICAL	55
4.1	Octant degeneracy in neutrino oscillation probability	57
4.1.1	Ambiguity in $P_{\mu e}$ and $P_{\mu\mu}$	58
4.2	Simulation of atmospheric neutrinos at ICAL	65
4.2.1	Atmospheric neutrino event generation	65
4.2.2	Statistical procedure	66
4.3	Results	68
4.3.1	Octant sensitivity at ICAL	69
4.3.2	Octant sensitivity at NO ν A and T2K	70
4.3.3	Combined octant sensitivity	71
5	Probing Lorentz and CPT Violation at ICAL	75
5.1	CPTV effects at the probability level	76
5.1.1	Formalism	76
5.1.2	Effect at the level of probability	79
5.2	Numerical procedure	83
5.2.1	Event simulation	83
5.2.2	Statistical procedure and the χ^2 analysis	85
5.3	Results	86
6	Non-Standard Interactions in neutrino propagation at ICAL	89
6.1	Neutrino NSI Framework: relevant parameters and constraints	90
6.2	Neutrino oscillation probability in matter with NSI	92
6.3	Neutrino oscillograms in presence of NSI	95

6.4	θ_{23} Octant determination in presence of NSI using the muon disappearance channel	101
6.5	Analysis and Event spectrum	103
6.6	Constraints on $\epsilon_{\mu\tau}, \epsilon_{\mu e}, \epsilon_{e\tau}$	104
7	Summary	111
7.1	Summary of simulation of muons	111
7.2	Summary of the Octant sensitivity study	112
7.3	Summary of Lorentz / CPT violation study	113
7.4	Summary of Non standard Interaction study	114

Synopsis

Neutrino physics has now entered an era of precision measurements following immense progress over the past few decades in establishing neutrino masses and mixings. It also offers great potential for understanding physics beyond the standard model (BSM). Neutrino oscillation and consequently, neutrino mass, remain one of the first and few solid empirical indicators of BSM physics. The neutrino mixing parameters $(\theta_{12}, \theta_{13}, \theta_{23}, \Delta m_{21}^2, |\Delta m_{31}^2|)$ have been already measured to good precision and this precision is expected to improve as ongoing and near-future experiments reach higher levels of accuracy and statistics. The measurement of a non-zero value of the mixing angle θ_{13} by the reactor experiments Double-Chooz, Daya-Bay and RENO heralds a major advance in neutrino physics. There are, however several questions in neutrino physics which are not yet resolved. The most two important unknown parameters are the CP violating phase, δ_{cp} , and the sign of the mass-squared difference, Δm_{31}^2 . There are two possible arrangements of the three neutrino mass states: (i) $m_1 < m_2 < m_3$ corresponding to Normal Hierarchy (NH) and (ii) $m_3 < m_1 < m_2$ corresponding to Inverted Hierarchy (IH). Determination of the sign of Δm_{31}^2 will provide the correct mass ordering of the neutrino. The current discovery of non-zero and relatively large θ_{13} strengthens the possibility of discovering the true hierarchy of neutrino masses via matter effect.

Motivated by these aspects, I have mainly worked on detector simulation and performed a physics sensitivity study of the ICAL (Iron Calorimeter) detector. ICAL is the proposed detector at the India-Based Neutrino Observatory (INO) experiment. It is proposed to be built at Theni in Southern India. The detector consists of 151 layers of magnetised iron plates interleaved with Resistive Plate Chambers (RPCs) as active detector element with a total mass of about 52 kt. It is designed primarily to study neutrino flavor oscillations through interactions of atmospheric neutrinos in the detector. The main goals of the ICAL detector are to make precision measurements of the neutrino oscillation parameters $(\theta_{23}$ and $|\Delta m_{31}^2|)$, and more importantly, to determine the neutrino mass hierarchy, the sign of Δm_{31}^2 . These goals can be achieved by observing charged-current (CC) interactions of atmospheric muon neutrinos and anti-neutrinos (ν_μ and $\bar{\nu}_\mu$) in the detector.

Muon Resolution Studies: The detector is mainly sensitive to charged-current events

from interactions of atmospheric neutrinos with detector material (mostly iron) where muons are produced (sometimes with additional hadrons as well), depending on the type and nature of the interaction. Hence it is crucial to correctly understand the response of ICAL to muons by detailed simulations and this is the focus of this work.

The ICAL geometry was simulated using GEANT4 software and muons with fixed momenta from 1–20 GeV/c and with direction $\cos \theta > 0.35$ were propagated through this simulated detector and their characteristics studied. In the current study, muons were generated in what is called the central part of the ICAL detector where the magnetic field is large and uniform. Both contained and partially contained (with muons exiting the detector) events were analysed. Each sample was analysed for the momentum resolution, reconstruction efficiency, charge identification efficiency and direction resolution. While the momentum resolution was about 9–14%, the momentum reconstruction efficiency was better than about 80% in most of the regions. The direction resolution was found to be indeed very good, being better than a degree for all angles for momenta greater than about 4 GeV/c, which is most important for studying the neutrino mass hierarchy through matter effects. The relative charge identification efficiency was also about 98% over this range.

Study of the Octant of θ_{23} : Our current knowledge of the mixing angle θ_{23} is mainly due to the SuperKamiokande (SK) atmospheric neutrino data. However the octant in which this mixing angle lies is not yet decisively determined by the data since previous experiments have been sensitive to only $\sin^2 2\theta_{23}$. We have studied the possibility of determining the octant of θ_{23} at the ICAL detector in conjunction with long baseline experiments T2K and NO ν A, in the light of the non-zero value of θ_{13} measured by reactor experiments.

We present the octant sensitivity for T2K/NO ν A and atmospheric neutrino experiments separately as well as the combined sensitivity. For the long baseline experiments, a precise measurement of θ_{13} , which can exclude degenerate solutions in the wrong octant, increases the sensitivity drastically. For $\theta_{23} = 39^\circ$ and $\sin^2 2\theta_{13} = 0.1$, at least $\sim 2\sigma$ sensitivity can be achieved by T2K + NO ν A for all values of δ_{CP} for both normal and inverted hierarchy. For atmospheric neutrinos, the moderately large value of θ_{13} measured in the reactor experiments is conducive to octant sensitivity because of enhanced matter effects. The ICAL detector can give a 2σ octant sensitivity for 500 kt yr exposure for $\theta_{23} = 39^\circ$, $\delta_{CP} = 0$ and normal hierarchy. This increases to 3σ for both hierarchies by combining

with T2K and NO ν A. This is due to a preference of different θ_{23} values at the minimum χ^2 by T2K/NO ν A and atmospheric neutrino experiments.

Lorentz and CPT violation studies: Apart from the standard oscillation physics, we have also studied the sensitivity of the ICAL detector to Lorentz and CPT violation in the neutrino sector. Its ability to identify the charge of muons in addition to their direction and energy makes ICAL a useful tool in putting constraints on these fundamental symmetries. Using resolution, efficiencies, errors and uncertainties obtained from ICAL detector simulations, we determine sensitivities to δb_{31} , which parametrizes the violations in the muon neutrino sector. We carry out calculations for three generic cases representing mixing in the CPT violating part of the hamiltonian, specifically, when the mixing is 1) small, 2) large, 3) the same as that in the PMNS matrix. We find that for both types of hierarchy, ICAL at INO should be sensitive to $\delta b_{31} \gtrsim 4 \times 10^{-23}$ GeV at 99 % C.L. for 500 kt-yr exposure, unless the mixing in the CPT violation sector is small.

Non Standard Interactions: We study the effects of non-standard interactions on the oscillation pattern of atmospheric neutrinos. We use neutrino oscillograms as our main tool to infer the role of the NSI parameters at the probability level in the energy range, $E \in 1 - 20$ GeV and zenith angle range, $\cos \theta \in -1 - 0$. We compute the event rates for atmospheric neutrino events in presence of NSI in the energy range $E \in 1 - 10$ GeV for ICAL detector. We have tried to find bounds on different NSI parameters using this detector. As an application, we discuss how NSI impacts the determination of the correct octant of θ_{23} .

List of Figures

1.1	Muon neutrino (left) and anti-neutrino(right) survival probability as a function of energy for 6000 Km. Lower and upper panel shows for vacuum and matter respectively. Black solid and magenta dotted curve are for $\Delta m_{31}^2 > 0$ and $\Delta m_{31}^2 < 0$ respectively. True value of δ_{cp} taken as zero.	24
1.2	Muon neutrino (left) and anti-neutrino(right) oscillation probability as a function of energy for 6000 Km. Lower and upper panel shows for vacuum and matter respectively. Black solid and magenta dotted curve are for $\Delta m_{31}^2 > 0$ and $\Delta m_{31}^2 < 0$ respectively. True value of δ_{cp} taken as zero.	25
1.3	The two possible hierarchies of neutrino mass eigenstates, normal hierarchy (left) and inverted hierarchy (right)	28
2.1	Modular structure of the ICAL detector	39
2.2	Constructional schematic of a basic Resistive Plate Chamber	41
2.3	Schematic images of the development of avalanche in an RPC. Top-left panel shows ionised gas atoms by the passage of a charged particle, the avalanche size is shown in top-right panel. Bottom-left panel shows the movement of the electrons and ions to the electrode and bottom-right panel shows that the charges in the resistive layers influence the field in a small area around the position where avalanche is developed.	42
3.1	Sample track of a 10 GeV neutrino event generating a 5.1 GeV muon track and associated hadron shower in the ICAL detector	48
3.2	Momentum distributions for $(P_{in}, \cos \theta) = (1 \text{ GeV}/c, 0.65)$ fitted with Landau convoluted Gaussian; this fits better than a pure Gaussian at lower energies, $P_{in} \leq 2 \text{ GeV}/c$	49
3.3	Muon resolution as a function of input momentum and $\cos \theta$	49

3.4	Reconstructed angular distribution for input $(P_{in}, \cos \theta_{in}) = (5 \text{ GeV}/c, 0.65)$; $\theta = 49.46^\circ$	51
3.5	Angular resolution in degrees as a function of input momentum.	51
3.6	Momentum reconstruction efficiency as a function of the input momentum for different $\cos \theta$ values.	52
3.7	The relative charge identification efficiency as a function of the input momentum for different $\cos \theta$ values. Note that the y -axis range is 0.87–1 and does not start from zero.	53
4.1	Behaviour of the muon survival and oscillation probabilities as a function of $\sin^2 2\theta_{13}$ showing the θ_{23} octant degeneracy and its breaking. The left panels are for the $\text{NO}\nu\text{A}$ peak energy and baseline (2 GeV, 812 Km), while the right panels are for a typical atmospheric neutrino energy and baseline (6 GeV, 5000 Km). The top row denotes the appearance channels $P_{\mu e}$ and $P_{e\mu}$, while the bottom row denotes the disappearance channel $P_{\mu\mu}$. The values of oscillation parameters chosen are $\theta_{23}^{tr} = 39^\circ$, $\theta_{23}^{wrong} = 51^\circ$. The bands denote a variation over the full range of the phase δ_{CP} . The inset shows the region of separation of the bands near $\sin^2 2\theta_{13} = 0.1$	60
4.2	Same as Figure 4.1 with a fixed true and test $\delta_{CP} = 0$ and true $\theta_{23}^{tr} = 39^\circ$, with the band denoting a variation over the full allowed range of $\theta_{23}^{wrong} = 45^\circ$ to 54° in the wrong octant.	61
4.3	Energy spectra of the probabilities $P_{\mu e}$ and $P_{\mu\mu}$ for the $\text{NO}\nu\text{A}$ baseline (left panels) and for a sample atmospheric neutrino baseline 5000 Km (right panels). The figure shows the variation in the probabilities in each case when $\sin^2 2\theta_{13}$ is varied over three values in the current allowed range, fixing the true and test θ_{23} values $\theta_{23}^{tr} = 39^\circ$ and $\theta_{23}^{wrong} = 51^\circ$. δ_{CP} is fixed to 0.	63
4.4	Energy spectra of the probabilities $P_{\mu e}$ and $P_{\mu\mu}$ for the $\text{NO}\nu\text{A}$ baseline (left panels) and for a sample atmospheric neutrino baseline 5000 Km (right panels). The figure shows the variation in the probabilities in each case when θ_{23}^{wrong} is varied over the entire allowed range in the wrong octant, as well as varying the test δ_{CP} , fixing the true values $\theta_{23}^{tr} = 39^\circ$ and $\delta_{CP}^{tr} = 0$ in the solid curve. The spread due to variation of both test parameters is denoted by the blue band. The black band shows the variation with test δ_{CP} for a fixed $\theta_{23}^{wrong} = 51^\circ$	64
4.5	Marginalized octant sensitivity from muon events with the ICAL detector (500 kt yr exposure), for the case of normal and inverted mass hierarchy. In this figure priors have been added.	70

4.6	Marginalized octant sensitivity from a combination of NO ν A and T2K, for the case of normal and inverted mass hierarchy. The test hierarchy has been fixed to be the same as the true hierarchy in this case. In this figure priors have been added.	71
4.7	Marginalized octant sensitivity from a combination of the atmospheric muon neutrino signal at the ICAL detector (500 kt yr) + NO ν A + T2K, for the case of normal and inverted mass hierarchy. In this figure priors have been added.	72
5.1	The oscillograms of $\Delta P = (P_{\nu_\mu\nu_\mu}^{U_b \neq 0} - P_{\nu_\mu\nu_\mu}^{U_b = 0})$ for 3 different mixing cases have been shown. The value of $\delta b_{31} = 3 \times 10^{-23} GeV$ is taken for $U_b \neq 0$. Left and right panels are for Normal and Inverted hierarchy respectively.	81
5.2	The oscillograms of $\Delta P = (P_{\bar{\nu}_\mu\bar{\nu}_\mu}^{U_b \neq 0} - P_{\bar{\nu}_\mu\bar{\nu}_\mu}^{U_b = 0})$ for 3 different mixing cases have been shown. The value of $\delta b_{31} = 3 \times 10^{-23} GeV$ is taken for $U_b \neq 0$. Left and right panels are for Normal and Inverted hierarchy respectively.	82
5.3	The difference of the $P_{\nu_\mu\nu_\mu}$ with and without CPTV for $\delta b_{31} = 3 \times 10^{-23} GeV$ for two θ_{b13} values as a function of energy for a specific value of zenith angle. All other oscillation parameters are same.	83
5.4	$\Delta\chi^2$ as a function of δb_{31} for different mixing of θ_b . Best fit oscillation parameters used as mentioned in Table 5.1 . The results are marginalized over θ_{23} , θ_{13} , δ_{CP} , Δm_{31}^2 and δb_{21} . Left and right panel are for Normal and Inverted hierarchy respectively.	86
5.5	$\Delta\chi^2$ as a function of δb_{31} for case 3) is shown. The Red curve represents that both sets of data has Normal hierarchy as true hierarchy, and the green curve for Inverted hierarchy respectively. Black curve shows the bounds where hierarchy is marginalized over.	87
6.1	Oscillograms of $P_{\mu\mu}$ for NH and IH with non-zero $\epsilon_{\mu\tau}$	96
6.2	Oscillograms of $\Delta P_{\mu\mu}$ with non-zero $\epsilon_{\mu\tau}$	97
6.3	Oscillogram pattern of $\Delta P_{\mu\mu}$ with non-zero $\epsilon_{e\mu}$, $\epsilon_{e\tau}$, $\epsilon_{\mu\tau}$	98
6.4	Oscillograms of $\Delta P_{e\mu}$ for the NSI parameter $\epsilon_{\mu\tau}$	99
6.5	The effect of $\epsilon_{e\mu}$, $\epsilon_{e\tau}$, $\epsilon_{\mu\tau}$ on the oscillogram of $\Delta P_{e\mu}$	100
6.6	$P_{\mu\mu}$ for LO and HO and for NH and IH. Here $L = 5000$ km and $E = 5$ GeV has been taken as input. The width of bands represents variation over $\delta_{CP} \in [-\pi, \pi]$	102

6.7	The difference with and without NSI of ν_μ (only) events for non-zero $\epsilon_{\mu\tau}$ (left) and $\epsilon_{\mu e}$ (right). All the data are generated for 500 kt-yr of exposure for magnetized ICAL assuming NH as the true hierarchy.	104
6.8	Constraints on NSI parameters $\epsilon_{\mu\tau}$ (left) and $\epsilon_{\mu e}$ (right) with ICAL detector for 500 kt-yr fiducial volume. Magenta and green curve are for Normal and Inverted hierarchy respectively.	106
6.9	Constraints on NSI parameters $\epsilon_{e\tau}$ with ICAL detector for 500 kt-yr fiducial volume. Magenta and green curve are for Normal and Inverted hierarchy respectively.	107
6.10	Contours of exclusion between SI and NSI in $\epsilon_{\mu\tau} - \epsilon_{\mu e}$ plane with ICAL detector of fiducial volume 500kt-yr. NH is taken as true hierarchy.	108
6.11	Contours of exclusion between SI and NSI in $\epsilon_{e\tau} - \epsilon_{\mu e}$ plane with ICAL detector of fiducial volume 500kt-yr. NH is taken as true hierarchy.	109
6.12	Contours of exclusion between SI and NSI in $\epsilon_{\mu\tau} - \epsilon_{e\tau}$ plane with ICAL detector of fiducial volume 500kt-yr. NH is taken as true hierarchy.	110

List of Tables

1.1	Recent best-fit and 3σ range of the oscillation parameters.	27
2.1	Detail specification of the ICAL detector	40
4.1	Systematic uncertainties used in the χ^2 analysis	67
4.2	Marginalized octant sensitivity with ICAL detector (500 kt yr exposure), and a combination of either of them with $\text{NO}\nu\text{A} + \text{T2K}$, for the case of normal (inverted) mass hierarchy, with $\sin^2 2\theta_{13}^{tr} = 0.1$ and $\delta_{CP}^{tr} = 0$. Priors have been included in this table.	72
5.1	True values of the oscillation parameters used in the analysis	84

Chapter 1

Introduction

Neutrinos are some of the most elusive Standard Model (SM) particles even though they are the most abundant particles in the universe after photon. They are neutral, interact only through the weak interaction and therefore, do not readily interact with other particles. As a result, neutrinos are particularly difficult to study. Neutrino experiments require extremely massive detectors in order to produce statistically significant results. With so little knowledge about neutrinos, neutrino experiments are integral to understanding weak interaction and are an important probe of new physics.

Neutrino physics has now entered an exciting era in which we are in the process of getting precision measurements of neutrino masses and mixings. It also offers great potential for understanding physics beyond the standard model (BSM). A number of present and future experiments are expected to yield more precise knowledge regarding the many unresolved questions.

In this chapter, we will first briefly summarize the history of neutrinos. Then, after describing the sources of neutrinos, we will talk about the phenomenology of neutrino mixing and neutrino oscillations. We will then mention the present status of the neutrino oscillations and then briefly discuss physics beyond oscillations. Finally, we describe the content of the thesis concisely.

1.1 History of Neutrinos

The history of neutrinos started with the famous letter from Wolfgang Pauli [1]. The experimental data [2,3] forced Pauli to assume the existence of a new particle, which was later called the neutrino. In 1911 Lise Meitner and Otto Hahn performed an experiment which showed that the energies of electrons emitted during β -decay had a continuous spectrum, this led to the obvious problem of having the conservation of linear momentum and angular momenta. In his most famous letter written in December 1930, Pauli suggested that in addition to the electrons and protons contained inside the atom, there are also extremely light neutral particles, which he called neutrons. He proposed that these neutrons, which were also emitted during β -decay and accounted for the missing energy and momentum, had simply not yet been discovered. In 1931, Enrico Fermi built upon Pauli's ideas of a yet undetected particle, and three years later published a very successful model of β -decay in which neutrinos were produced. At this time Fermi coined the term "neutrino", which is Italian for "small neutral one", thus giving birth to the neutrino.

In 1956 [4] Clyde Cowan and Frederick Reines discovered the neutrino (actually the antineutrino), by observing the inverse beta decay reaction $p + \bar{\nu}_e \rightarrow n + e^+$ occurring from antineutrinos produced in a nuclear reactor. This proved the hypothesis set forth by Pauli many years before. The muon neutrino was discovered in 1962 by Lederman, Schwartz and Steinberger [5] and the tau neutrino was detected in 2000 by the direct observation of the Nu-Tau (DONuT) collaboration [6]. In 1957 Pontecorvo conceptualized the possibility of neutrino oscillations by generalizing the notions related to kaon mixing. As only one flavour of neutrino had been discovered at that time, Pontecorvo's hypothesis focused on mixing between ν and $\bar{\nu}$. In 1962, with the knowledge that multiple flavours of neutrinos existed in nature, Maki, Nakagawa and Sakata proposed oscillations between ν_e and ν_μ . This framework later extended to tau neutrino.

In 1967, the Homestake experiment, pioneered by Davis and Bahcall uncovered the first indication that supported the neutrino oscillation theory. They sought to measure the rate at which solar neutrinos were captured by chlorine nuclei. They had observed a deficit between the measurement and the prediction, but the source of the discrepancy remained unclear. Many pointed towards an inadequate understanding of the solar model or errors in the neutrino experiments. The deficit phenomenon, however, was not limited to solar neutrino observations. Atmospheric neutrino experiments also reported a

deviation from the approximately 2:1 ratio between muon and electron neutrinos that were produced through the $\pi \rightarrow \mu\nu_\mu, \mu \rightarrow e\nu_e\nu_\mu$. IMB [7] experiment, MACRO [8], and Kamiokande collaboration [9] found significant deficits in ν_μ fluxes. In 1998, Super-Kamiokande [10] explained the shortfall by fitting their results with $\nu_\mu \leftrightarrow \nu_\tau$ oscillation framework. The debate in the solar neutrino sector ended in 2001 when the Sudbury Neutrino Observatory (SNO) [11] experiment provided conclusive evidence that roughly two-thirds of the solar neutrino flux was related to non ν_e flavours. This result supported the notion of neutrino oscillations and reconciled the total flux measurement with the standard solar model (SSM) prediction.

1.2 Sources of Neutrinos

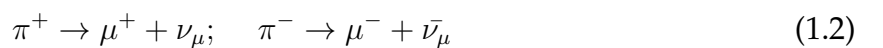
Neutrinos are generated from different sources with a wide range of energies. They can be classified as natural and artificial. In this section we summarize different sources of neutrinos which will play a major role in understanding neutrino oscillations.

Solar neutrinos: According to the standard solar model (SSM), the net thermonuclear reaction which takes place inside the core of the Sun is the fusion of four protons and two electrons into a ${}^4\text{He}$ nucleus, two electron neutrinos and an energy release of $Q = 26.73$ MeV, in the form of photons. This process can be written as



With the extremely large number of reactions taking place inside the core of the Sun, it can be seen that a large flux of electron flavour neutrinos is created. The reaction is mainly divided into two processes: a) proton-proton (pp) chain and b) Carbon-Nitrogen-Oxygen(CNO)cycle. The energies of the solar neutrinos are in the hundreds of KeV to a few MeV range. The total solar neutrino flux on the earth is about $5.94 \times 10^{10} \text{ cm}^{-2}\text{s}^{-1}$.

Atmospheric neutrinos: When primary cosmic rays interact with nuclei in the atmosphere of the Earth, secondary particles, mostly pions and some kaons, are produced in hadronic showers. Atmospheric neutrinos are produced from the decay of those secondary particles, dominantly by the following decay chains of pions :



At high energies, kaons also contribute to the production of muons and neutrinos. The muons then decay before reaching the Earth's surface and give rise to electrons, electron neutrinos and muon neutrinos through the following processes

$$\mu^+ \rightarrow e^+ + \nu_e + \bar{\nu}_\mu; \quad \mu^- \rightarrow e^- + \bar{\nu}_e + \nu_\mu \quad (1.3)$$

Hence the ratio of muon and electron type neutrino is 2:1. Energy range of the atmospheric neutrinos is from a few hundred of MeV to 10^8 GeV. Atmospheric neutrino flux falls steeply as $E^{-2.7}$ for energies above 1 GeV and the flux becomes undetectably small after about a 100 TeV (See [12] for a detail review). Atmospheric neutrino flux peaks at zenith angle $\approx 90^\circ$, i.e near the horizon, due to the larger length of atmosphere available in this direction. Atmospheric neutrinos have long energy and oscillation length, hence atmospheric neutrinos will be very useful to study neutrino oscillations as well as new physics.

Relic neutrinos: Relic neutrinos are one of the most important products of the Big Bang. In the early Universe, neutrinos were in thermal equilibrium through weak interaction with the other particles. As the Universe expanded and cooled, the rates of weak interaction processes decreased and neutrinos decoupled when these rates became smaller than the expansion rate. The weak interaction cross-section of the Relic neutrino with matter is very small due to extremely small temperatures. Therefore, the direct detection of Relic neutrinos is an extremely difficult task with present experimental techniques.

Astrophysical source of neutrinos: Very high energy neutrinos are produced by astrophysical sources like Gamma-Ray Burst (GRB), Active Galactic Nuclei (AGN). Supernova Remnants (SNRs), AGNs, GRBs and other astrophysical sources can accelerate protons to such energies (and above) by the Fermi acceleration mechanism. The interactions of these protons with soft photons or matter from the source can give Ultra high energy (UHE) neutrinos through the following process: $p\gamma, pp \rightarrow \pi^\pm X$, $\pi^\pm \rightarrow \mu^\pm \nu_\mu (\bar{\nu}_\mu)$, $\mu^\pm \rightarrow e^\pm \bar{\nu}_\mu (\nu_\mu) \nu_e (\bar{\nu}_e)$ with a flux ratio of $\phi_{\nu_e} : \phi_{\nu_\mu} : \phi_{\nu_\tau} = 1 : 2 : 0$. Recently, the IceCube detector [13] has observed a total of 37 neutrino events with deposited energies ranging from 30 TeV to 2 PeV. The 2 PeV event is the highest-energy neutrino event ever observed.

Accelerator based neutrinos: Accelerator based neutrino beam are mainly composed of muon neutrinos. They are produced by the decay of charged pions and kaons. Initially a beam of high energy protons is directed to a thick nuclear target, producing

secondaries such as positively charged pions and kaons which are collected and focused using a magnetic horn. These mesons then enter an evacuated decay tunnel where they decay to produce muons and neutrinos. The muons and the remaining mesons are absorbed in a beam dump at the end of the tunnel, producing a neutrino beam. Semi-leptonic decays of charmed particles have also been used to produce neutrinos where a high-energy proton beam is stopped in a thick target to generate heavy hadrons. The charmed heavy hadrons decay promptly emitting equal fluxes of high-energy electron and muon neutrinos.

Reactor neutrinos: Nuclear reactors are the major sources of artificially produced neutrinos. Power generation in nuclear reactors take place through the fission of neutron-rich isotopes like ^{235}U , ^{238}U , ^{239}Pu . Electron antineutrinos are produced by the chain of β -decays of the fission products in the energy range of 0.1 to 10 MeV.

1.3 Neutrino Oscillations

It has been seen that neutrinos change flavour during their propagation. To explain this it is essential that at least two of the neutrinos have masses, which are different from each other and the flavour eigenstates are different from the mass eigenstates. In this section, the standard formalism and expressions for neutrino oscillation and survival probabilities are described in detail.

Neutrino oscillation arises from a mixture between the flavour and mass eigenstates of neutrinos. The neutrino flavour eigenstate $|\nu_\alpha\rangle$ ($\alpha = e, \mu, \tau$) can be written as a superposition of mass eigenstates $|\nu_j\rangle$ ($j=1,2,3$).

$$|\nu_\alpha\rangle = \sum_{j=1,2,3} U_{\alpha j}^* |\nu_j\rangle \quad (1.4)$$

where $U_{\alpha j}$ is a 3×3 unitary mixing matrix, known as the Pontecorvo-Maki-Nakagawa-Sakata (PMNS) matrix [14, 15].

Parametrization of U:

In general for an $N \times N$ unitary matrix, there are $\frac{N(N-1)}{2}$ mixing angles and $\frac{N(N+1)}{2}$ phases. But $2(N-1)$ phases can be absorbed by the redefinition of the fields. Hence, in case of N flavours the leptonic mixing matrix $U_{\alpha j}$ depends on $\frac{(N-1)(N-2)}{2}$ Dirac CP-violating phases (δ_{CP}). If the neutrinos are Majorana particles, there are $(N-1)$ additional Majorana phases.

Standard Derivation of the Oscillation Probability:

In the standard theory of neutrino oscillations, the mass states $|\nu_j\rangle$ are eigenstates of the Hamiltonian,

$$H |\nu_j\rangle = E_j |\nu_j\rangle \quad (1.5)$$

with energy eigenvalues $E_j = \sqrt{p^2 + m_j^2}$. By solving the Schrodinger equation, the time evolution of neutrino mass eigenstates can be written as

$$|\nu_j(t)\rangle = e^{-iE_j t} |\nu_j\rangle \quad (1.6)$$

Thus the time evolution of a flavour state can be written as

$$|\nu_\alpha(t)\rangle = \sum_j U_{\alpha j}^* e^{-iE_j t} |\nu_j\rangle \quad (1.7)$$

At $t = 0$, the flavour state can be written as $|\nu_\alpha(t = 0)\rangle = |\nu_\alpha\rangle$. Using the unitary relation $U^\dagger U = 1$, the mass eigenstates can be written in terms of flavour eigenstates as

$$|\nu_j\rangle = \sum_\alpha U_{\alpha j} |\nu_\alpha\rangle \quad (1.8)$$

The amplitude of transition from a flavour state ν_α to ν_β can then be written as

$$S_{\nu_\alpha \rightarrow \nu_\beta}(t) = \langle \nu_\beta | \nu_\alpha(t) \rangle = \sum_j U_{\alpha j}^* U_{\beta j} e^{-iE_j t} \quad (1.9)$$

The oscillation probability from a flavour state ν_α to ν_β can be written as

$$P_{\nu_\alpha \rightarrow \nu_\beta}(t) = |S_{\nu_\alpha \rightarrow \nu_\beta}(t)|^2 = \sum_{j,k} U_{\alpha j}^* U_{\beta j} U_{\alpha k} U_{\beta k}^* e^{-i(E_j - E_k)t} \quad (1.10)$$

The quartic products in eqn 1.10 are free from the Majorana phases, hence Majorana phases cannot be measured in neutrino oscillation experiment. Neutrino oscillations have two different channels, if the flavour $\nu_\alpha \neq \nu_\beta$, then it is called the oscillation probability and if $\nu_\alpha = \nu_\beta$ then it is known as the survival probability.

1.3.1 Neutrino Oscillations in vacuum

We will first describe neutrino oscillations in vacuum. In vacuum, neutrino mass eigenstates evolve independently. At first, we will derive the oscillation probability formula for the two neutrino flavour case. Then we will go on to the three flavour case.

Two flavour oscillations:

In the two flavour oscillation case, we consider two flavour eigenstates of neutrinos as ν_α and ν_β . They are the superposition of two mass eigenstates ν_1 and ν_2 of masses m_1 and m_2 respectively. The mixing matrix in the two flavour case is

$$U = \begin{pmatrix} \cos\theta & \sin\theta \\ -\sin\theta & \cos\theta \end{pmatrix} \quad (1.11)$$

where θ is the mixing angle. In the two flavour case, there is only one mixing angle, θ , and there is no CP phase.

From equation 1.10, it is straightforward to derive the expression for the probability of oscillation from ν_α to ν_β

$$P(\nu_\alpha \rightarrow \nu_\beta) = \sin^2 2\theta \sin^2\left(\frac{\Delta m^2 L}{4E}\right) \quad (1.12)$$

In the case $\alpha = \beta$, the survival probability can be obtained from the unitarity- relation of the probability

$$P(\nu_\alpha \rightarrow \nu_\alpha) = 1 - \sin^2 2\theta \sin^2\left(\frac{\Delta m^2 L}{4E}\right) \quad (1.13)$$

If we use natural units then the survival probability can be written as

$$P(\nu_\alpha \rightarrow \nu_\alpha) = 1 - \sin^2 2\theta \sin^2\left(1.27 \frac{\Delta m^2 [eV^2] L [km]}{E [GeV]}\right) \quad (1.14)$$

The oscillation length is $L^{osc} = \frac{4\pi E}{\Delta m^2}$. From equations 1.12 and 1.14, we see that the oscillation and survival probabilities depend on the mixing angle θ , the mass squared difference

Δm^2 , oscillation distance L and energy E of the neutrino.

Three flavour oscillations:

In case of 3 flavour oscillation, there are 3 flavour eigenstates and 3 mass eigenstates. There will be 3 mixing angles and one Dirac CP phase. If the neutrinos are Majorana, there will be extra 2 phases. However, the rephasing invariants in eqn 1.10 (quartic products) are independent of the Majorana phases, hence it follows that they have no effect on the neutrino oscillations. The mixing matrix can be written using the PMNS parametrization in terms of $\theta_{12}, \theta_{13}, \theta_{23}$ and phase δ

$$U = R^{23} R^{13} R^{12} = \begin{pmatrix} 1 & 0 & 0 \\ 0 & c_{23} & s_{23} \\ 0 & -s_{23} & c_{23} \end{pmatrix} \begin{pmatrix} c_{13} & 0 & s_{13}e^{-i\delta} \\ 0 & 1 & 0 \\ -s_{13}e^{-i\delta} & 0 & c_{13} \end{pmatrix} \begin{pmatrix} c_{12} & s_{12} & 0 \\ -s_{12} & c_{12} & 0 \\ 0 & 0 & 1 \end{pmatrix} \quad (1.15)$$

$$U = \begin{pmatrix} c_{12}c_{13} & s_{12}c_{13} & s_{13}e^{-i\delta} \\ -s_{12}c_{23} - c_{12}s_{23}s_{13}e^{i\delta} & c_{12}c_{23} - s_{12}s_{23}s_{13}e^{i\delta} & s_{23}c_{13} \\ s_{12}s_{23} - c_{12}c_{23}s_{13}e^{i\delta} & -c_{12}s_{23} - s_{12}c_{23}s_{13}e^{i\delta} & c_{23}c_{13} \end{pmatrix} \quad (1.16)$$

where $c_{ij} = \cos\theta_{ij}$, $s_{ij} = \sin\theta_{ij}$. Now using the mixing matrix and using equation 1.10, we can write the oscillation probability

$$P(\nu_\alpha \rightarrow \nu_\beta) = \delta_{\alpha\beta} - 4 \sum_{j>k} \text{Re}[U_{\alpha j}^* U_{\beta j} U_{\alpha k} U_{\beta k}^*] \sin^2\left(\frac{\Delta m_{jk}^2 L}{4E}\right) + 2 \sum_{j>k} \text{Im}[U_{\alpha j}^* U_{\beta j} U_{\alpha k} U_{\beta k}^*] \sin^2\left(\frac{\Delta m_{jk}^2 L}{2E}\right) \quad (1.17)$$

Imaginary part of the probability expression contains information about the CP violating phase. For CP-transformed reaction $\bar{\nu}_\alpha \rightarrow \bar{\nu}_\beta$, the transition probability will be the same except that the sign of the imaginary term is reversed.

The probability expressions are not as simple as in the case of two flavour case, but one can use approximations to get ideas about the probability. One of the most important approximation is one mass squared dominance approximation (OMSD), where Δm_{21}^2 is taken as zero. The OMSD approximation is good enough for a reasonably large range of energies and baselines, and it has the advantage of being exact in the parameter θ_{13} . The expressions of the probabilities $P_{\mu\mu}$ and $P_{\mu e}$ in vacuum are given by the following expressions obtained in the OMSD approximation [16–20],

$$P_{\mu\mu}^v = 1 - \sin^2 2\theta_{23} \sin^2 \left[1.27 \Delta m_{31}^2 \frac{L}{E} \right] + 4 \sin^2 \theta_{13} \sin^2 \theta_{23} \cos 2\theta_{23} \sin^2 \left[1.27 \Delta m_{31}^2 \frac{L}{E} \right] \quad (1.18)$$

$$P_{\mu e}^v = \sin^2 \theta_{23} \sin^2 2\theta_{13} \sin^2 \left[1.27 \Delta m_{31}^2 \frac{L}{E} \right] \quad (1.19)$$

Atmospheric neutrinos cover large distances and wide range of energies, additionally recent large value of θ_{13} will be good enough to use OMSD approximation. Hence, the expressions of $P_{\mu\mu}$ and $P_{\mu e}$ using OMSD approximation will be relevant in this thesis.

1.3.2 Neutrino Oscillations in matter

When neutrinos travel through a dense medium, their propagation can be significantly modified by the coherent forward scattering from particles they encounter along the way. Potential due to the scattering on matter modifies the mixing of the neutrinos. As a result, the oscillation probability differs from the oscillation in vacuum. The flavour-changing mechanism in matter was formulated by Mikhaev, Smirnov and Wolfenstein (MSW) [21], who first pointed out that there is an interplay between flavour-non-changing neutrino-matter interactions and neutrino mass and mixing. The MSW effect stems from the fact that electron neutrinos (and antineutrinos) have different interactions with matter compared to neutrinos of other flavours. In particular, ν_e can have both charged current and neutral current elastic scattering with electrons, while ν_μ or ν_τ have only neutral current interactions with electron. When the neutrino traverses the Earth, the oscillation probability is calculated taking into account Earth's matter potential due to the forward scattering amplitude of charged current ν_e interactions with electrons. Neutral current interactions are neglected here because they lead to flavour-independent terms which are irrelevant

for the oscillation probabilities.

The effective CC Hamiltonian for an electron neutrino propagating through matter (electrons) can be written as

$$H_{eff} = \frac{G_F}{\sqrt{2}} [\bar{\nu}_e \gamma^\mu (1 - \gamma^5) e] [\bar{e} \gamma_\mu (1 - \gamma^5) \nu_e] \quad (1.20)$$

Using Fierz transformation, we can write

$$H_{eff} = \frac{G_F}{\sqrt{2}} [\bar{\nu}_e \gamma^\mu (1 - \gamma^5) \nu_e] [\bar{e} \gamma_\mu (1 - \gamma^5) e] \quad (1.21)$$

If we consider the effective Hamiltonian over the electron background and integrate over the electron momentum, the Hamiltonian can then be written as

$$H_{eff} = V_{cc} \bar{\nu}_e \gamma^0 \nu_e \quad (1.22)$$

where the charged current potential

$$V_{cc} = \sqrt{2} G_F N_e \quad (1.23)$$

Here N_e is the electron density of the medium.

Similarly, the neutral current potential of neutrinos propagating in a medium can be calculated. In an electrically neutral medium, the total number of protons and electrons is the same, hence they will cancel the overall potential. The potential will arise only from the interaction with neutrons. Hence, the net effective potential will be

$$V_{NC} = \frac{G_F N_n}{\sqrt{2}} \quad (1.24)$$

It is important to note that the neutral current potential is flavour independent, hence it will not have any effect on neutrino oscillations.

It is useful to write the matter potential in terms of the matter density ρ and the electron-

fraction in the nucleon, Y_e as

$$V_{cc} = 7.56 \times 10^{-14} \left(\frac{\rho}{g/cm^3} \right) Y_e eV \quad (1.25)$$

For earth matter $Y_e \approx 0.5$. For anti-neutrinos the matter potential will be negative, this is mainly due to the anti-commutation relation of the creation and annihilation operator. The number operator for neutrino is positive and for anti-neutrino it is negative, so V_{cc} will be $-V_{cc}$ for anti-neutrinos.

Two flavour oscillations in matter:

The matter effect on neutrino oscillation probability can be better understood if we start with the two flavour case. Lets take two flavour eigenstates ν_e and ν_μ and two mass eigenstates ν_1 and ν_2 . The time evolution equation in flavour state can be written as

$$i \frac{d}{dt} \begin{pmatrix} \nu_e(t) \\ \nu_\mu(t) \end{pmatrix} = H_f \begin{pmatrix} \nu_e(t) \\ \nu_\mu(t) \end{pmatrix} \quad (1.26)$$

The effective Hamiltonian in flavour basis is

$$H_f = U \begin{pmatrix} -\Delta & 0 \\ 0 & \Delta \end{pmatrix} U^\dagger + \begin{pmatrix} V_c & 0 \\ 0 & 0 \end{pmatrix} = \begin{pmatrix} -\Delta \cos 2\theta + V_c & \Delta \sin 2\theta \\ \Delta \sin 2\theta & \Delta \cos 2\theta - V_c \end{pmatrix} \quad (1.27)$$

where $\Delta = \frac{\Delta m^2}{4E}$ and $V_c = \sqrt{2} G_F N_e$. We will diagonalize the H_f by the orthogonal transformation

$$H_m = U_m^\dagger H_f U_m \quad (1.28)$$

where the unitary matrix

$$U_m = \begin{pmatrix} \cos \theta_m & \sin \theta_m \\ -\sin \theta_m & \cos \theta_m \end{pmatrix} \quad (1.29)$$

is the effective mixing matrix in matter. After diagonalization, the mass squared differ-

ence and mixing angle in matter are

$$\Delta m_m^2 = \sqrt{(\Delta m^2 \cos 2\theta - A)^2 + (\Delta m^2 \sin 2\theta)^2} \quad (1.30)$$

and the mixing angle in presence of matter is

$$\tan 2\theta_m = \frac{\tan 2\theta}{1 - \frac{A}{\Delta m^2 \cos 2\theta}} \quad (1.31)$$

where $A = 2EV_c$. The oscillation probability will be the same but with modified mixing parameters

$$P(\nu_\alpha \rightarrow \nu_\beta) = \sin^2 2\theta_m \sin^2\left(\frac{\Delta m_m^2 L}{4E}\right) \quad (1.32)$$

Long baselines or high matter densities are required to observe significant matter effects. Under the resonant condition $\Delta m^2 \cos 2\theta = A$, the oscillation will be significantly enhanced. The mixing angle in matter will be $\theta_m = \frac{\pi}{4}$ or maximal irrespective of the vacuum mixing angle.

Three flavour oscillations in matter:

In the case of 3 neutrino flavours, the effective matter Hamiltonian in flavour basis is given by

$$H_f = U \begin{pmatrix} 0 & 0 & 0 \\ 0 & \Delta_{21} & 0 \\ 0 & 0 & \Delta_{31} \end{pmatrix} U^\dagger + \begin{pmatrix} V_c & 0 & 0 \\ 0 & 0 & 0 \\ 0 & 0 & 0 \end{pmatrix} \quad (1.33)$$

In order to compute the effective masses and mixing angles in matter, the above Hamiltonian is diagonalized. The normalized eigenvectors of H_f form the modified matter mixing matrix. Hence, the matter and vacuum parameters are related by comparison. This technique has been implemented exactly by a numerical solution of the evolution equation in matter.

Here we give the analytic expressions for the probabilities in the OMSD approximation, which amounts to neglecting the smaller mass-squared difference Δm_{21}^2 in comparison to Δm_{31}^2 , as we have already discussed. We have checked that this approximation

works well at energies and length scales relevant here. However, all the plots we give are obtained by numerically solving the full three flavour neutrino propagation equation using Prem Reference Earth Model (PREM) [22] density profile for the earth.

Making this approximation, the mass squared difference $(\Delta m_{31}^2)^m$ and mixing angle $\sin^2 2\theta_{13}^m$ in matter can be related to their vacuum values by

$$(\Delta m_{31}^2)^m = \sqrt{(\Delta m_{31}^2 \cos 2\theta_{13} - A)^2 + (\Delta m_{31}^2 \sin 2\theta_{13})^2} \quad (1.34)$$

$$\sin 2\theta_{13}^m = \frac{\Delta m_{31}^2 \sin 2\theta_{13}}{\sqrt{(\Delta m_{31}^2 \cos 2\theta_{13} - A)^2 + (\Delta m_{31}^2 \sin 2\theta_{13})^2}} \quad (1.35)$$

Using the above substitutions, the OMSD probabilities $P_{\mu\mu}$ and $P_{\mu e}$ in matter are given by

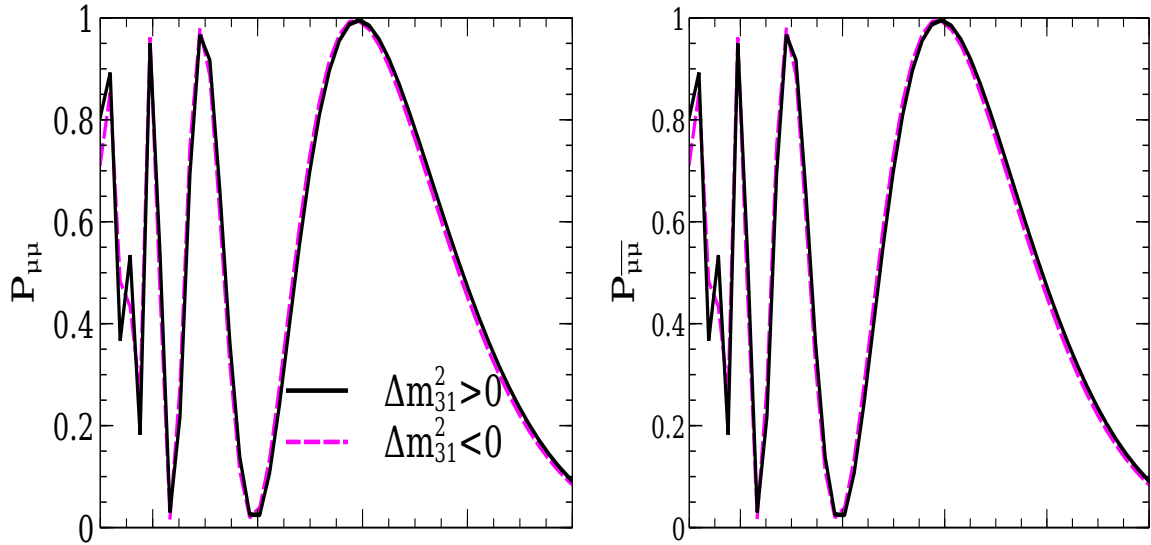
$$\begin{aligned} P_{\mu\mu}^m = & 1 - \cos^2 \theta_{13}^m \sin^2 2\theta_{23} \sin^2 \left[1.27 \left(\frac{\Delta m_{31}^2 + A + (\Delta m_{31}^2)^m}{2} \right) \frac{L}{E} \right] \\ & - \sin^2 \theta_{13}^m \sin^2 2\theta_{23} \sin^2 \left[1.27 \left(\frac{\Delta m_{31}^2 + A - (\Delta m_{31}^2)^m}{2} \right) \frac{L}{E} \right] \\ & - \sin^4 \theta_{23} \sin^2 2\theta_{13}^m \sin^2 \left[1.27 (\Delta m_{31}^2)^m \frac{L}{E} \right] \end{aligned} \quad (1.36)$$

$$P_{\mu e}^m = \sin^2 \theta_{23} \sin^2 2\theta_{13}^m \sin^2 \left[1.27 (\Delta m_{31}^2)^m \frac{L}{E} \right] \quad (1.37)$$

The probability for the time-reversed transition $P_{\mu e}^m$ is same as $P_{e\mu}^m$ with the replacement $\delta_{cp} \rightarrow -\delta_{cp}$. The OMSD analytical expressions are insensitive to δ_{cp} , hence $P_{\mu e}^m = P_{e\mu}^m$. For an inverted neutrino mass hierarchy, the corresponding probabilities are obtained by reversing the sign of Δm_{31}^2 . The antineutrino probabilities can be written down by making the replacement $A \rightarrow -A$ in the above equations.

In Fig 1.1 and 1.2, we plot the 3-flavour muon neutrino(left panel), anti-neutrino (right panel) survival and oscillation probabilities in vacuum(upper panel) and in matter(lower panel) as a function of energy for both normal and inverted hierarchies for a baseline of 6000 km. The oscillation parameters used as mentioned in Table 1.1. In case of inverted hierarchy, we have only changed the sign of Δm_{31}^2 as negative, other oscillation parameters are taken same as the normal hierarchy oscillation parameters.

Oscillation in Vacuum, L = 6000 Km



Oscillation in Matter, L = 6000Km

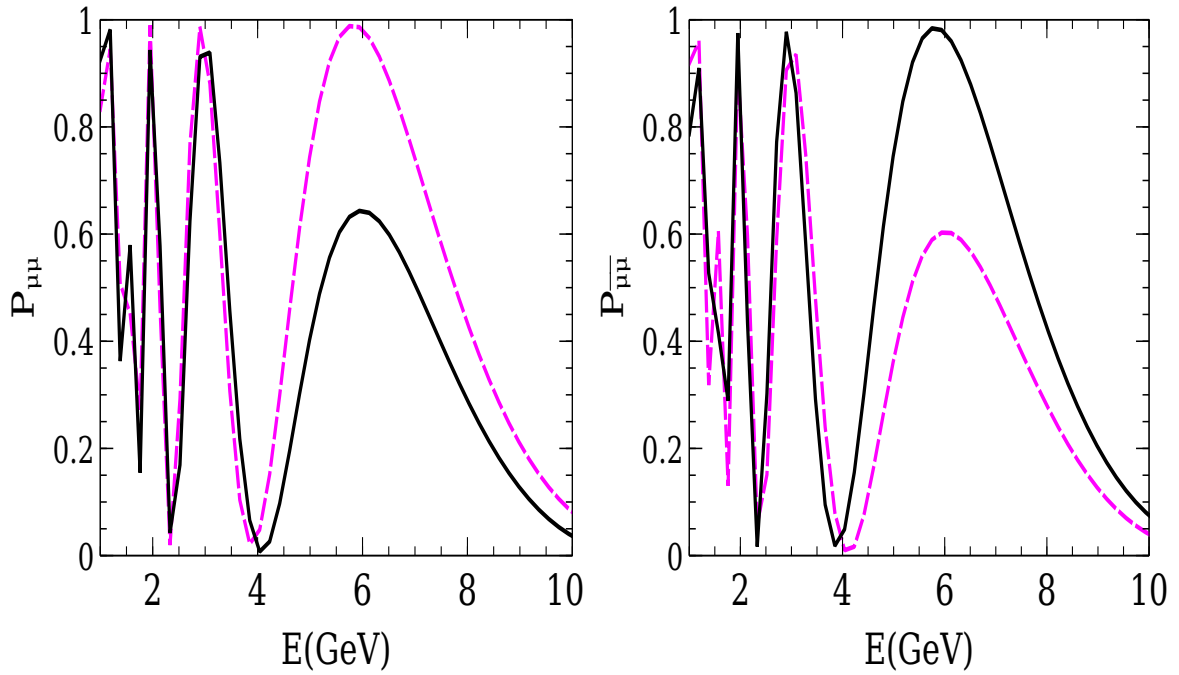
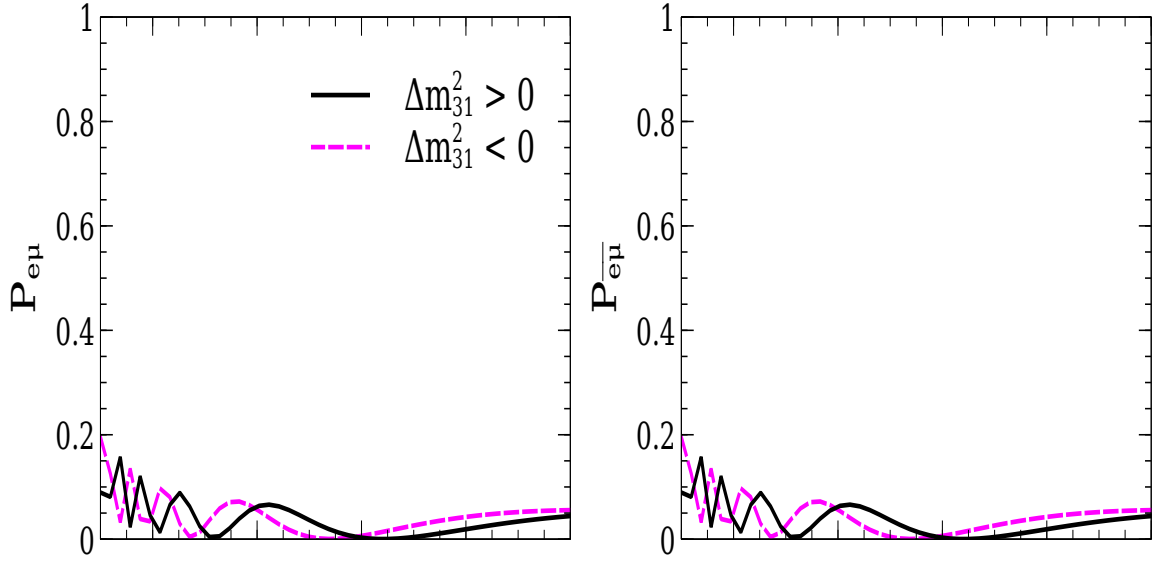


Figure 1.1: Muon neutrino (left) and anti-neutrino(right) survival probability as a function of energy for 6000 Km. Lower and upper panel shows for vacuum and matter respectively. Black solid and magenta dotted curve are for $\Delta m_{31}^2 > 0$ and $\Delta m_{31}^2 < 0$ respectively. True value of δ_{cp} taken as zero.

Oscillation in Vacuum, L = 6000 Km



Oscillation in matter, L = 6000 Km

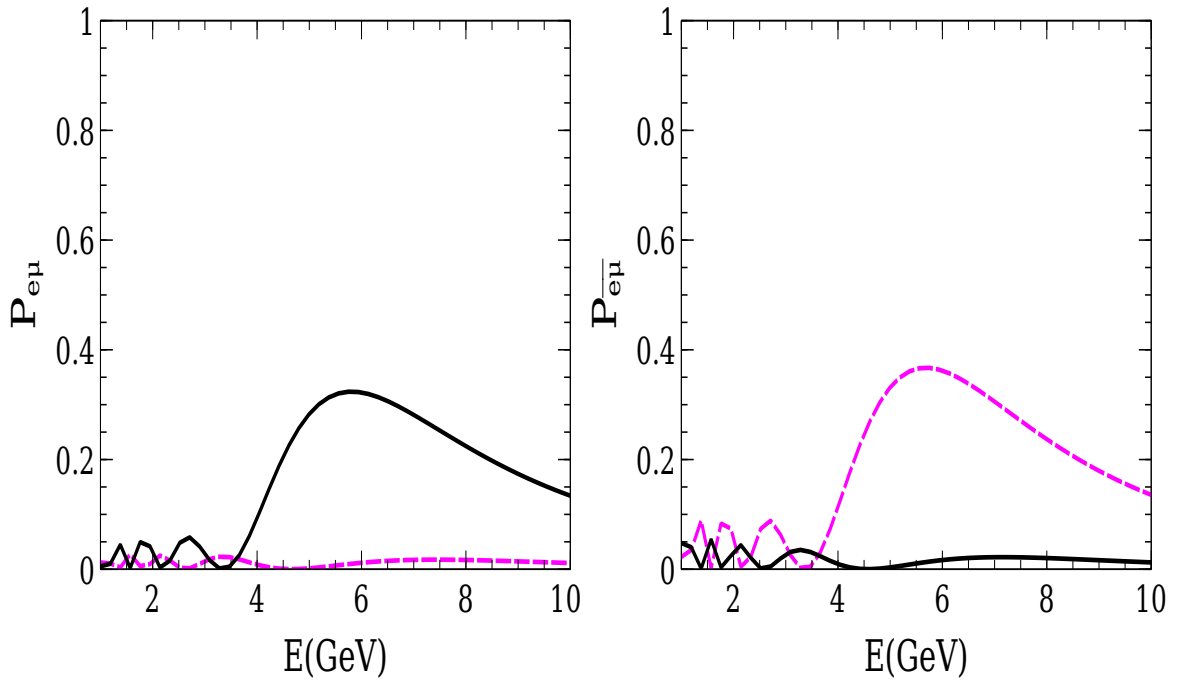


Figure 1.2: Muon neutrino (left) and anti-neutrino(right) oscillation probability as a function of energy for 6000 Km. Lower and upper panel shows for vacuum and matter respectively. Black solid and magenta dotted curve are for $\Delta m_{31}^2 > 0$ and $\Delta m_{31}^2 < 0$ respectively. True value of δ_{cp} taken as zero.

We point out some of the interesting qualitative features demonstrated by the probabilities in Fig 1.1 and 1.2

a) It is clear from the figures that the survival probabilities for neutrinos and anti-neutrinos are same for vacuum. This is due to the fact that, there is no matter interactions, which are different for neutrinos and anti-neutrinos.

b) In case of matter effects, the differences between the probability values for normal and inverted hierarchy in all the channels are maximized in the energy range 4-8 GeV.

c) It shows that $P_{\mu\mu}$ in matter for neutrinos with normal hierarchy deviates from the vacuum oscillations and for anti-neutrinos it is $P_{\bar{\mu}\bar{\mu}}$ that exhibits this deviation for inverted hierarchy.

d) Matter effects in $P_{\mu e}$ in case of a NH manifest themselves by a rise over the corresponding value for an IH. In the case of $P_{\bar{\mu}e}$, IH rises over the NH.

1.4 Present status of neutrino parameters

In the current Standard Model (SM) framework, neutrinos are regarded as massless, uncharged leptons that interact with matter only via the weak force. However, there is strong evidence which suggests that neutrinos undergo transformations between flavours, a quantum mechanical phenomenon known as "neutrino oscillations", which require neutrinos to be massive. Recently large number of neutrino experiments started data taking and reconfirming the neutrino oscillations as well as precision measurement of the oscillation parameters.

The neutrino mixing matrix, or the PMNS matrix can be parametrized in terms of three mixing angles θ_{12} , θ_{13} , θ_{23} , and a CP violating phase δ_{cp} . Neutrino oscillations are also governed by two mass squared differences Δm_{21}^2 and Δm_{31}^2 . Solar neutrino oscillation parameters, θ_{12} and Δm_{21}^2 have been measured from the combined analysis of the KamLAND and solar neutrino data. Super-Kamiokande (SK) atmospheric, T2K [23] and MINOS [24] and other atmospheric neutrino experiments have measured the value of

$\sin^2 2\theta_{23}$ and $|\Delta m_{31}^2|$. After decades of speculation on whether or not θ_{13} is zero, data from these experiments have revealed that the value of θ_{13} is non-zero. The short baseline reactor neutrino experiments, Daya Bay [25], RENO [26] and Double Chooz [27] have excluded $\theta_{13} = 0$ at 5.2σ , 4.9σ and 3.1σ respectively. Recent [28] global analysis best fit value of the oscillation parameters are given in Table 1.1

Oscillation Parameter	Best-fit value	3σ range
$\sin^2 \theta_{12}/10^{-1}$	3.23	2.78 - 3.75
$\sin^2 \theta_{23}/10^{-1}$ (NH)	5.67	3.92 - 6.43
$\sin^2 \theta_{23}/10^{-1}$ (IH)	5.73	4.03 - 6.40
$\sin^2 \theta_{13}/10^{-1}$ (NH)	2.34	1.77 - 2.94
$\sin^2 \theta_{13}/10^{-1}$ (IH)	2.40	1.83 - 2.97
Δm_{21}^2 [10^{-5} eV ²]	7.60	7.11 - 8.18
$ \Delta m_{31}^2 $ [10^{-3} eV ²] (NH)	2.48	2.30 - 2.65
$ \Delta m_{31}^2 $ [10^{-3} eV ²] (IH)	2.38	2.30 - 2.54
δ/π (NH)	1.34	0.0 - 2.0
δ/π (IH)	1.48	0.0 - 2.0

Table 1.1: Recent best-fit and 3σ range of the oscillation parameters.

1.4.1 Open challenges in oscillations physics

Large value of θ_{13} has expedited the possibility of resolving the two most important questions, namely, neutrino mass hierarchy or the sign of Δm_{31}^2 , and, measuring the CP violation in the neutrino sector. Apart from these two there is also an important question, known as the Octant degeneracy of θ_{23} .

Neutrino mass hierarchy: Neutrino has three mass eigenstates, m_1, m_2, m_3 . There are two possibilities, i) $m_3 > m_2 > m_1$, called as Normal hierarchy, or ii) $m_2 > m_1 > m_3$, namely, Inverted hierarchy as shown in Fig 1.3. Oscillation experiments have measured only the absolute value of Δm_{31}^2 , but hierarchy of the mass-spectrum is still unknown.

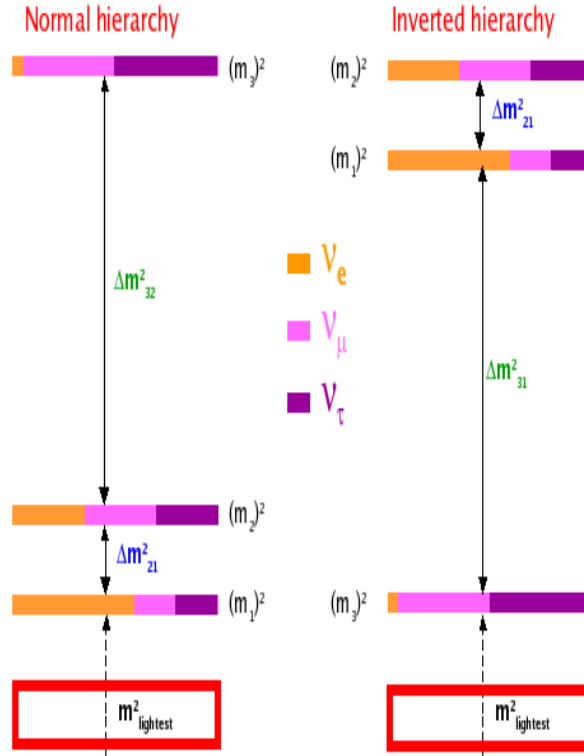


Figure 1.3: The two possible hierarchies of neutrino mass eigenstates, normal hierarchy (left) and inverted hierarchy (right)

Large value of non zero θ_{13} will enhance the oscillation when neutrinos will pass through matter, hence the sign of the mass squared difference can be known from the matter effect. Atmospheric neutrinos travel maximum distance through earth matter. Neutrinos and anti-neutrinos interact differently with earth matter. Non zero value of θ_{13} will help to resolve mass hierarchy if any atmospheric neutrino experiment can detect neutrino and anti-neutrino differently.

CP violation: δ_{CP} appears in the PMNS matrix, if the PMNS is real then there is no CP violation, in other words if δ_{CP} is zero or π then CP is conserved. CP violation has been observed in the quark sector, hence there can be a complex phase analogous to the CKM phase. Since δ_{CP} occurs with the mixing angle θ_{13} in the PMNS matrix, the recent measurement of non zero and moderately large value of θ_{13} by reactor and accelerator experiment is expected to be conducive for the measurement of δ_{CP} .

Octant degeneracy: Another unknown parameter in neutrino oscillation physics is the exact value of θ_{23} . Atmospheric neutrino experiments, like SK has measured $\sin^2 2\theta_{23}$, however the octant in which this mixing angle lies is not yet decisively determined by the data. Octant degeneracy in neutrino oscillation means that, it is not known clearly whether the angle is θ_{23} or $\frac{\pi}{2} - \theta_{23}$.

1.5 Beyond neutrino oscillations

Recently, mass eigenstate mixing induced neutrino oscillations has become the standard theory accounting for the solar, atmospheric and long baseline neutrino experiments. However, there are other alternative theories which can also induce neutrino oscillations or can cause effects similar to some of the experimental observations. Mass eigenstate mixing induced neutrino oscillations are basically due to the fact that different mass eigenstates have different energies for the same momentum. Thus, in principle, any theories which can modify the dispersion relation to meet this condition can induce neutrino oscillations, such as violation of Lorentz invariance (LIV) and CPT(CPTV), non standard interactions etc.

1.5.1 Lorentz Invariance Violation / CPT Violation

Lorentz invariance is intimately related to CPT symmetry as stated in the CPT theorem [29–31]. For a local field theory, the Lorentz invariance leads to CPT symmetry, while breaking CPT symmetry naturally causes Lorentz invariance violation, which is proven in [32].

The Standard Model (SM) and supersymmetric (SUSY) models are designed to incorporate CPT invariance. However, these models do not include gravity. The Standard Model Extension (SME) [33, 34] is an effective field theory that incorporates gravity with the SM, by way of introducing CPT-even and CPT-odd terms. The fundamental scale of the SME is the Planck scale $m_p \approx 10^{19} GeV$, which is about 17 orders of magnitude larger than electroweak scale m_w associated with SM. By treating the SM as a low energy effective theory of underlining fundamental physics, all the possible Lorentz symmetry breaking terms are added into the SM Lagrangian using the SM fields and gravitational

fields. To generate neutrino oscillation effects, it turns out that the minimal renormalizable version of SME [35] is sufficient.

The possible origin of CPT violation in the neutrino sector has been studied in the context of extra dimensions [36,37], non-factorizable geometry [38], and non-local causal Lorentz invariant theories [39]. There are other alternative studies, which tries to put bounds on CPT sector in many different contexts(See [40–42] for a detailed review). The original formalism to analyze CPT violating effects on neutrino oscillations has been proposed in [43]. The CPT violating term contributes to the standard Hamiltonian, which will alter the effective neutrino masses. This change in neutrino mass would affect the neutrino oscillation wavelengths. CPT violation in neutrino oscillations would manifest itself in the observation $P(\nu_\alpha \rightarrow \nu_\beta) \neq P(\bar{\nu}_\beta \rightarrow \bar{\nu}_\alpha)$. However, when neutrinos propagate through matter, the matter effects give rise to "fake" CP and CPT violation even if the vacuum Hamiltonian is CPT conserving. These fake effects need to be accounted for while searching for CPT violation.

CPT violation may also occur if particle and anti-particle masses are different. Such violation, however, also breaks the locality assumption of quantum field theories [32]. Many authors have studied how best to parametrize and/or use neutrino oscillations and neutrino interactions to perform tests of CPT and Lorentz symmetry breaking in different contexts, ranging from neutrino factories and telescopes to long baseline, atmospheric, solar and reactor experiments, including those looking for supernova neutrinos (See [43–68] for a detail review) .

1.5.2 Non standard neutrino interactions

As discussed in section 1.3, standard matter interactions affect the survival and oscillation probability of the electron neutrino, but not of the muon and tau neutrinos, since muon and tau particle are absent in normal matter. There can be, however, non-standard matter interactions (NSI) that influence the survival and oscillation probabilities of second and third generation neutrinos. These are interactions of neutrinos with matter (up and down quarks and leptons). One way in which non-standard interactions can arise is through the violation of the unitarity of the lepton mixing matrix in certain see-saw models [69]. Siz-able NSI effects can be introduced via new scalar exchange bosons such as Higgs bosons

or scalar leptoquarks, some supersymmetric models may also give rise to NSI [70].

In future neutrino experiments, 'new physics', beyond the SM may appear in the form of unknown couplings involving neutrinos, which are usually referred to as non-standard neutrino interactions(NSI). Compared with standard neutrino oscillations, NSIs could contribute to the oscillation probabilities and neutrino event rates as sub-leading effects, and may bring in very distinctive phenomena. Running and future neutrino experiments will provide us with more precision measurements on neutrino flavour transitions, and therefore, the window of searching for NSIs is open.

In principle, NSIs could exist in the neutrino production, propagation, and detection processes. In general, the NSI can impact the neutrino oscillation signals via two kinds of interactions : (a) charged current (CC) interactions (b) neutral current (NC) interactions. However, CC interactions affect processes only at the source or the detector and these are clearly discernible at near detectors (via the zero distance effect). On the other hand, the NC interactions affect the propagation of neutrinos. The main motivation to study NSIs is that if they exist we ought to know their effects on physics.

In the literature, there exist several theoretical and phenomenological studies of NSIs for atmospheric, accelerator, reactor, solar and supernova neutrinos(See for details [71–76]). In addition, some experimental collaborations have obtained bounds on NSIs [77,78].

Other than these two phenomena, there are various questions, which are yet unresolved, few of them are

Existence of sterile neutrinos:

The hypothesis of sterile neutrinos are based on recent anomalies observed in neutrino experiments. Decades of experimentation have produced a vast number of results in neutrino physics and astrophysics, some of which are in perfect agreement with only three active neutrinos, while a small subset calls for physics beyond the standard model.

The first, and individually still most significant, piece pointing towards new physics is the LSND [79] result, where electron antineutrinos were observed in a pure muon antineutrino beam. The most straightforward interpretation of the LSND result is antineu-

trino oscillation with a mass squared difference, Δm^2 , of about 1 eV^2 . Given the other neutrino oscillation parameters, the LSND Δm^2 requires a fourth neutrino.

A new anomaly supporting the sterile neutrino hypothesis emerges from the recent re-evaluations of reactor antineutrino fluxes [80], which find a 3% increased flux of antineutrinos relative to the previous calculations. As a result, more than 30 years of data from reactor neutrino experiments, which formerly agreed well with the flux prediction, have become the observation of an apparent 6% deficit of electron antineutrinos. This is known as the reactor antineutrino anomaly and is compatible with sterile neutrinos having $\Delta m_{sterile}^2 > 1 \text{ eV}^2$.

Another hint consistent with sterile neutrinos comes from the source calibrations performed for radio-chemical solar neutrino experiments based on gallium [81, 82]. Both the source strength and reaction cross section are known with some precision and a 5-20% deficit of the measured to expected count rate was observed. Again, this result would find a natural explanation by a sterile neutrino $\Delta m_{sterile}^2 > 1 \text{ eV}^2$.

However, cosmological data, observations of the cosmic microwave background and large scale structure favor the existence of a fourth light degree-of-freedom which could be a sterile neutrino. Recent Planck results [83] show that effective number of neutrinos is, $N_{eff} = 3.30 \pm 0.27$ and an upper limit of 0.23 eV for the summed neutrino mass.

Dirac or Majorana nature:

If massive neutrinos are Dirac particles, they must be distinguishable from their antiparticles because of lepton number conservation. On the other hand, Majorana neutrino is its own antiparticle which can participate in lepton-number-violating processes. Only charge-neutral fermions can be Majorana and hence neutrinos stand out to be the only probable candidates within the Standard Model.

Establishing whether neutrinos are Dirac fermions possessing distinct antiparticles, or are Majorana fermions, i.e. spin 1/2 particles that are identical with their antiparticles, is of fundamental importance for understanding the underlying symmetries of particle interactions and the origin of neutrino masses. The neutrinos with definite mass will be Dirac fermions if particle interactions conserve some additive lepton number, e.g. the total lepton charge $L = L_e + L_\mu + L_\tau$. If no lepton charge is conserved, the neutrinos will be Majorana fermions (see, e.g. [84]).

The massive neutrinos are predicted to be of Majorana nature by the see-saw mechanism of neutrino mass generation [85], which also provides an attractive explanation of

the smallness of neutrino masses and, through the leptogenesis theory [86], of the observed baryon asymmetry of the Universe. If the neutrinos are Majorana in nature, then Majorana phases are same for all the massive neutrinos, which violates lepton number. Hence, they do not have any effect on lepton number conserving process like the neutrino oscillations.

Absolute scale of neutrino mass:

Significant constraints on the absolute scale of neutrino mass can be obtained through β -decay, neutrinoless double beta decay experiments and also from cosmology. The experimental searches for neutrinoless double beta decay have a long history (see, e.g. [87, 88]). The best sensitivity was achieved in the Heidelberg–Moscow ^{76}Ge experiment [89]: Recent study [90] shows the strongest mass upper limit of $m_{\beta\beta}^{0\nu}$ ranges from 0.115 to 0.339 eV depending on different choices of nuclear matrix elements. While the bound from cosmology [83] is 0.23 eV.

Mechanism of neutrino mass generation:

There are different mass models which try to explain small neutrino masses. Important models are Left-Right symmetric models, models with spontaneous B-L violation, radiative mass models, Grand unified models (SU(5), SO(10)) and supersymmetric models. One of the most important mechanism of neutrino mass generation is the see-saw mechanism [85]. The see-saw mechanism is briefly described below–

see-saw mechanism:

The principle of the seesaw mechanism can be understood by looking at the neutrino mass matrix. One has to assume that besides the usual left handed (LH) neutrinos ν_L , there are right handed (RH) neutrinos ν_R . Therefore one can construct a Dirac mass term for neutrinos,

$$\mathcal{L}_{mass}^D = m_D \bar{\nu}_R \nu_L + h.c. = \frac{1}{2} (m_D \bar{\nu}_R \nu_L + m_D \bar{\nu}_L^c \nu_R^c) + h.c. \quad (1.38)$$

since neutrinos have zero electric charge, in general also Majorana mass terms are possible,

$$\mathcal{L}_{mass}^L = \frac{1}{2} m_L \bar{\nu}_L^c \nu_L + h.c. \quad (1.39)$$

$$\mathcal{L}_{mass}^R = \frac{1}{2} m_R \bar{\nu}_R^c \nu_R + h.c. \quad (1.40)$$

Now one can introduce a mass matrix M , such that

$$\mathcal{L}_{mass} = \mathcal{L}_{mass}^D + \mathcal{L}_{mass}^L + \mathcal{L}_{mass}^R \quad (1.41)$$

where

$$M = \begin{pmatrix} m_L & m_D \\ m_D^T & m_R \end{pmatrix} \quad (1.42)$$

in the most general case. In the seesaw scenario the RH neutrino fields $\nu_R = N_R$ are assumed to be fields with a heavy mass, whereas m_D is of the electroweak scale. Therefore $m_D \ll m_R$. Since ν_L possesses non zero isospin and hypercharge, LH Majorana is forbidden by the SM, so $m_L = 0$. Hence the mass eigenstates will be

$$m_1 \approx \frac{m_D^2}{m_R} \quad (1.43)$$

$$m_2 \approx m_R \quad (1.44)$$

As a consequence, one has a neutrino at a mass scale $\lambda_N = m_R$ of new physics and a very light neutrino, the mass of which is suppressed by $\frac{m_D}{\lambda_N}$.

Whether these non-standard effects can explain neutrino experimental data is certainly worth investigating. On the other hand, these alternatives are new physics beyond the Standard Model and testing them is theoretically important. Atmospheric neutrinos cover a wide range of energies, path lengths and matter densities, and will prove to be a powerful tool to explore new physics.

1.6 An overview of the thesis

Large number of experiments have been designed to study these unresolved questions, many are in proposal state, which have potential to resolve these interesting questions. Motivated by these aspects, the thesis mainly focuses on the simulation study, oscillation and new physics study at the future neutrino experiment ICAL detector at INO. The thesis is organized in the following way:

Chapter 2 describes the ICAL detector. In this chapter, we have described the ICAL detector geometry, working principle of the active detector elements, which are Resistive Plate chambers(RPC) and electronic systems of ICAL.

In Chapter 3, we have discussed the simulation of muons at the ICAL detector, which is very crucial to study neutrino oscillation physics.

In Chapter 4, we have studied the possibility of determining the octant of θ_{23} at the ICAL detector in conjunction with long baseline experiments T2K and NO ν A, in the light of the non-zero value of θ_{13} measured by reactor experiments.

Chapter 5 contains the sensitivity of the ICAL detector to Lorentz and CPT violation. We have also shown that strong constraints on CPT violating parameters can be achieved.

In chapter 6 , we have shown the effects of non-standard interactions on the oscillation pattern of atmospheric neutrinos at the ICAL detector.

Chapter 7 is a summary of the thesis and its main conclusion.

Chapter 2

ICAL@INO

The India-based Neutrino Observatory, (INO) [91] Project is a multi-institutional effort aimed at building a world-class underground laboratory with a rock cover of approximately 1200 m for non-accelerator based high energy and nuclear physics research in Southern India. The detector will be located inside a cavern with rock cover in order to reduce the cosmic muon background. Iron Calorimeter (ICAL) detector is the proposed detector for INO. The ICAL detector consists of 151 layers of magnetised iron plates interleaved with Resistive Plate Chambers (RPCs) as the active detector element with a total mass of about 52 ktons. Magnetization of the detector will help to identify neutrino and anti-neutrino.

The chapter is organised as follows: In section 2.1, we have highlighted the physics motivation of the ICAL detector. We have briefly described the ICAL detector geometry in section 2.2. In section 2.3, we have talked about the active detector element RPC. Gas flow system has been described in section 2.4. Finally, the electronic and readout system has been briefly mentioned in section 2.5.

2.1 The physics motivation of ICAL@INO

The ICAL detector is contemplated as a detector mainly for atmospheric neutrinos. The primary detection mechanism is via detection of muons produced in charged current (CC) neutrino interactions. The major physics goals of the ICAL detector are

1. Precision measurement of the neutrino oscillation parameters (θ_{23} and $|\Delta m_{31}^2|$).

2. Determination of the sign of Δm_{31}^2 , hence the neutrino mass hierarchy.

3. Measure the deviation of θ_{23} from maximality and resolving octant degeneracy.

Apart from the oscillation measurement, new physics can also be studied with the magnetized ICAL detector.

4. Probing CPT violation in the atmospheric neutrino sector.

5. Testing non-standard neutrino matter interaction in atmospheric neutrino propagation.

6. Probing cosmic rays through very high energy muons underground.

7. Indirect search for dark matter using the large detector volume.

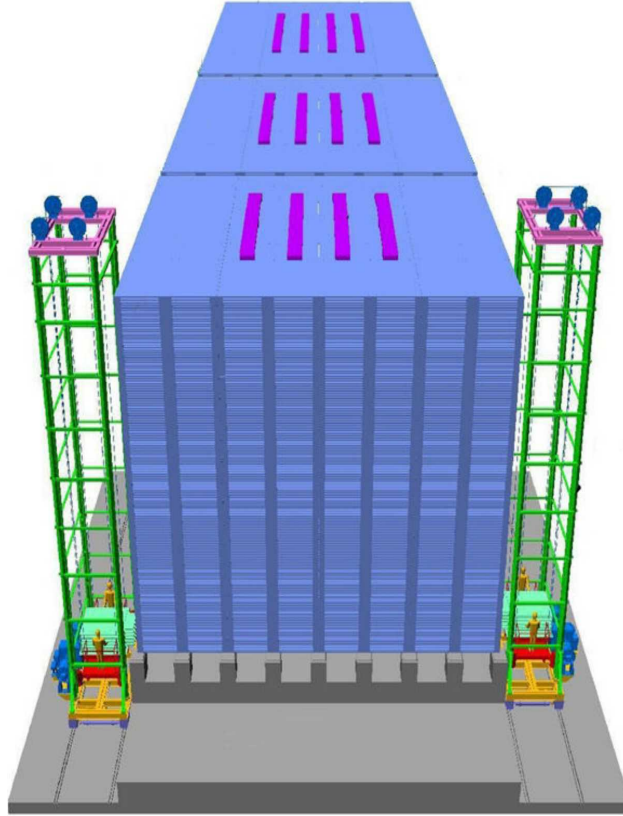


Figure 2.1: Modular structure of the ICAL detector

2.2 ICAL Detector Geometry

The proposed ICAL detector has a modular structure, it will have three modules. The size of each module is $16\text{ m} \times 16\text{ m} \times 14.45\text{ m}$. A schematic illustration of the ICAL detector is shown in Fig 2.1. Each module comprises 151 horizontal layers of 5.6 cm thick iron plates of size $16\text{ m} \times 16\text{ m} \times 5.6\text{ cm}$ with a vertical gap of 4 cm, interleaved with RPCs.

The basic RPC units of size $1.84\text{ m} \times 1.84\text{ m} \times 2.5\text{ cm}$ are placed in grid-format within the air gap, with a 16 cm horizontal gap between them accommodating steel support structures in both x and y directions. Hence the iron sheets are supported every 2 m in both the x and y directions. The typical value of the magnetic field strength is around 1.3 Tesla. The detail specification of the ICAL detector is given in Table 2.1.

Number of Modules	3
Dimension of each Module	16 m × 16 m × 14.5 m
Detector Dimension	48 m × 16 m × 14.5 m
Number of RPC layers	151
Iron plate thickness	5.6 cm
Magnetic field	1.3 Tesla
Dimension of each RPC	1.84 m × 1.84 m × 2.4 cm
RPC units/ layer/ module	64
Total no. of RPC units	28800
No.of electronic readout channels	3.7×10^6

Table 2.1: Detail specification of the ICAL detector

2.3 The active detector element RPC

The resistive plate chamber is a DC operated gas based detector with good spatial as well as timing resolution. It is a type of spark chamber with resistive electrodes. Good spatial and timing resolution makes it well suited for fast tracking calorimetry. It is made of two parallel electrodes(float glass) of thickness 3 mm with a volume resistivity of $10^{12}\Omega\text{-cm}$. These glass plates are separated with a spacing of 2 mm by means of highly insulated spacers. A proper gas mixture at atmospheric pressure is circulated through the gap and an appropriate electric field is applied across the glass electrodes through a resistive coating on their outer surfaces. The gas mixture is required for the multiplication of charge (streamer mode) produced when some ionizing particle passes through the gas volume. The schematic diagram of a basic RPC is shown in Fig 2.2.

2.3.1 Principle of operation

An ionizing particle passing through the gaseous gap initiates a streamer in the gas volume which results in a local discharge of the electrodes. Owing to the high resistivity and quenching characteristics of the glass electrodes, the discharge is limited to a tiny area of about 0.1 cm^2 . This discharge induces an electrical signal on the external pick up strips on both sides of the RPC, which can be used to record the location and time of ionization. The schematic diagram is shown in Fig 2.3. The RPCs may be operated either in the

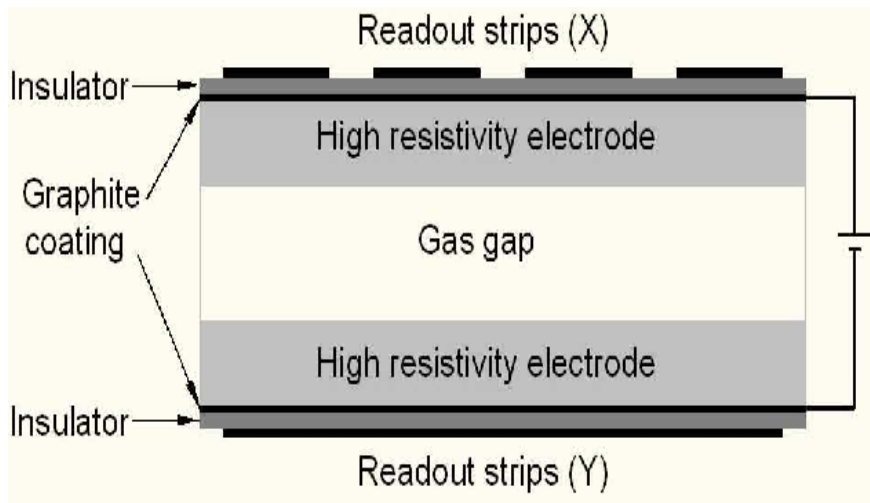


Figure 2.2: Constructional schematic of a basic Resistive Plate Chamber

avalanche mode or streamer discharge mode. Avalanche mode corresponds to the generation of a Townsend avalanche followed by the release of primary charge by the ionizing radiation. It operates at a lower voltage and the gain is less. Typical pulse amplitudes are of the order of a few mV. In the streamer mode the avalanche generated is followed by a streamer discharge. The secondary ionization continues until there is a breakdown of the gas and a continuous discharge takes place. This mode operates at a higher voltage and also results in high gain. Typical pulse amplitudes are of the order of 100-200 mV. We are operating the RPCs in avalanche mode.

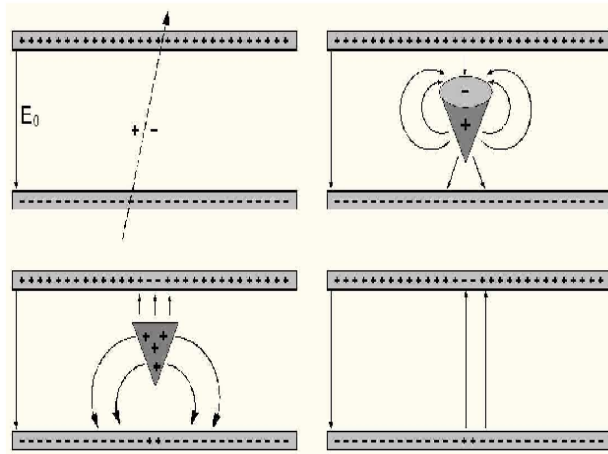


Figure 2.3: Schematic images of the development of avalanche in an RPC. Top-left panel shows ionised gas atoms by the passage of a charged particle, the avalanche size is shown in top-right panel. Bottom-left panel shows the movement of the electrons and ions to the electrode and bottom-right panel shows that the charges in the resistive layers influence the field in a small area around the position where avalanche is developed.

2.4 Gas system

The suitable gases for RPCs were chosen considering the following aspects—low working voltage, high gain, good proportionality, high rate capability. The gas mixture decides the working mode of the RPC in avalanche or in streamer mode, resulting in different characteristics and performances. Currently the RPC's are operated in avalanche mode for which the main component should be an electronegative gas, with high enough primary ionization production but with small free path for electron capture. The high electronegative attachment coefficient limits the avalanche electron number. The three gases used are Argon, Isobutane and R-134a (Freon). R-134a is an eco friendly electronegative gas with high enough primary ionization production but with small free path for electron capture. Isobutane has high absorption probabilities for UV photons produced in electron ion recombination, so acts as a quenching gas. It limits the charge spread. Argon is added to control the excess number of electrons. Composition of the gas mixture will be 95.42% of Freon, 4.21% of Isobutane and 0.37% of Argon.

2.5 Readout system

The readout of the RPCs will be performed by external orthogonal X and Y pickup strips. A localized discharge due to the passage of charged particles will induce pulses on the appropriate strips. The pulses will go to front end ASICs located near the strip ends. Fast discriminators of the ASICs will provide a fast timing signal. The proposed strips are 3 cm wide. Hence in each module and in single layer of RPC, there will be 64 strips along the X-direction and 512 strips along the Y direction.

2.5.1 Electronic readout system

The signal readout chain at the front-end essentially consists of fast, high gain, HMC based pre-amplifiers and low-level, threshold leading-edge discriminators, followed by the digital front-ends. The incoming detector signals are passed through programmable threshold comparators for producing digital logic signals. These signals are used for recording Boolean hit information, for generating trigger primitives as well by time multiplexing blocks for generating timing signals. Signals from only one coordinate will be used for generating the trigger. Processing of only one coordinate signals for generating trigger primitives and using time multiplexing techniques for recording timing information will reduce the DAQ channel count and hence the cost. The time multiplexing scheme combines hit information from a block of strip channels into a single data stream which can be passed on to multi-hit TDCs at the back end. In this scheme, the front-end processing will be achieved by a custom ASIC chip whereas the hit recording and time multiplexing is done by a commercial FPGA device.

The trigger generator is an independent sub-system which uses the same hit signals to look for required patterns of hits in the detector and initiate data recording if any of the interesting predefined hit patterns occur inside the detector. For instance, a trigger may be generated when certain hit patterns such as 2 or 3 hit layers out of 5 consecutive layers occur. This will ensure the trigger generation of nearly all the relevant atmospheric neutrino events. Programmability is the key requirement of this sub-system so that different physics motivated data recording plans may be supported during the course of experiment. A commercial FPGA device based design is best suited for this purpose. We plan to use the VME standard for the DAQ system and hosts will be based on Linux PC boxes.

Chapter 3

Simulation of ICAL for muons

An accurate determination of the muon energy and direction is crucial to achieve the neutrino oscillation physics goals. Muons (and sometimes also associated hadrons) arise from the CC interactions of atmospheric ν_μ and $\bar{\nu}_\mu$ in the detector; both the $\nu_\mu \rightarrow \nu_\mu$ and $\nu_e \rightarrow \nu_\mu$ oscillation channels are sources of ν_μ ($\bar{\nu}_\mu$). Hence the muons produced in the detector are sensitive to the pattern of neutrino flavour oscillations, and in turn can be used to probe the neutrino oscillation parameters of interest.

In addition, the muon energy and direction information can be combined with that of the hadrons to directly recover the energy and direction of the neutrinos. While CC ν_e interactions produce electrons in the final state, ICAL is not optimised to reconstruct their energy and direction with high precision due to their rapid energy loss mechanisms in the dense iron. As ν_μ and $\bar{\nu}_\mu$ pass through the earth matter, they undergo different interactions depending on the mass hierarchy. Hence, the hierarchy may be determined by observing individual event rates for ν_μ and $\bar{\nu}_\mu$, which give rise to μ^- and μ^+ , respectively, in CC interactions. Therefore, the ICAL detector must be optimised to correctly identify the charge of muons.

The chapter is organised as follows: in section 3.1, we briefly explain the procedure to simulate muon tracks in the detector and the algorithm to reconstruct their momentum and charge. In section 3.2, we show the response of the ICAL detector to fixed energy and fixed direction muons.

3.1 Simulation Framework

The geometry of the proposed ICAL detector has been simulated using the GEANT4 [92] package. Muons being minimum ionizing particles leave long, clean, tracks in the detector, hence ICAL detector is most sensitive to muons. The muon momentum can be determined from the curvature of its track as it propagates in the magnetized detector and also by measuring its path length. The charge of the muon can also be found from the direction of curvature of the track and this in turn distinguishes ν_μ and $\bar{\nu}_\mu$ interactions. A sample track of 10 GeV neutrino is shown in Fig 3.1.

When a charged particle, for example, a muon, passes through an RPC, it gives a signal which is counted as a “hit” in the detector with assigned x or y values from the respective pick-up strip information, a z -value from the layer information, and a time stamp t . All the possible pairs of nearby x and y hits in a plane are combined to form a cluster. A set of clusters generated in a few successive layers is called a tracklet. The most important part of the reconstruction are track finding and track fitting.

3.1.1 Track finding

The input to the track finding algorithm are the hits. Typically, muons leave only about one hit per layer they traverse (~ 1.6 , on average) while hadrons and electrons, due to the very different nature of their energy loss mechanisms, give showers which leave several hits per layer. Including the possibility of cross-talk (which gives the possibility of more than one hit in a plane for muons as well), the separation/rejection of hadronic showers is done by an algorithm that uses a cut on the total number of hits in a given RPC module. Track finder first find possible clusters in the three adjacent planes. It uses a simple curve fitting algorithm to find tracklets from the clusters. Adjacent tracklets are associated into tracks and the longest possible tracks are found [93] by iteration of this process.

The direction (up/down) of the track is calculated from the timing information which is averaged over the x and y timing values in a plane. The track finder also separates out tracks as “shower-like” or “muon-like”; for the case of muon-like tracks which have at least 5 hits in the event, the clusters in a layer are averaged to yield a single hit per layer

with x, y and timing information and are sent to the track fitter for further analysis.

3.1.2 Track fitting

A Kalman-filter [94] based algorithm is used to fit the tracks based on the bending of the tracks in the magnetic field. Every track is identified by a starting vector $X_0 = (x, y, dx/dz, dy/dz, q/p)$, which contains the position of the earliest hit (x, y, z) as recorded by the finder, with the charge-weighted inverse momentum q/p taken to be zero. The initial track direction is calculated from the first two layers. This initial state vector is then extrapolated to the next layer using a standard Kalman-filter based algorithm. In this algorithm a track is represented by a set of parameters, called state vector which contains the information about the position of the hits, direction of the track and the momentum of the particle at that position. A state vector is defined as $x = (x, y, dx/dz, dy/dz, q/p)$. The state covariance matrix, C , a 5×5 matrix, contains the expected error in the state vector. The state vector is updated in every next plane using the information about the current state vector. The estimated state vector is given by

$$x_k = F_{k-1}x_{k-1} + u_{k-1} ,$$

where F is the propagator matrix which transports the state vector from $(k-1)^{th}$ plane to k^{th} plane and u is the process noise which contains information about multiple scattering and energy loss by the particle. The propagator matrix contains the information about the magnetic field and it is calculated for every pair of detector planes. Track fitting is done to get the accurate estimate of the state vector at each plane.

The process of iteration also achieves the best fit to the track. The track is then extrapolated to another half-layer of iron (since the interaction is most likely to have taken place in the iron) to determine the vertex of the interaction and the best fit value of the momentum at the vertex is returned as the reconstructed momentum (both in magnitude and direction). While q/p determines the magnitude of the momentum at the vertex, the direction is reconstructed using dx/dz and dy/dz , which yield $\cos \theta$ and ϕ .

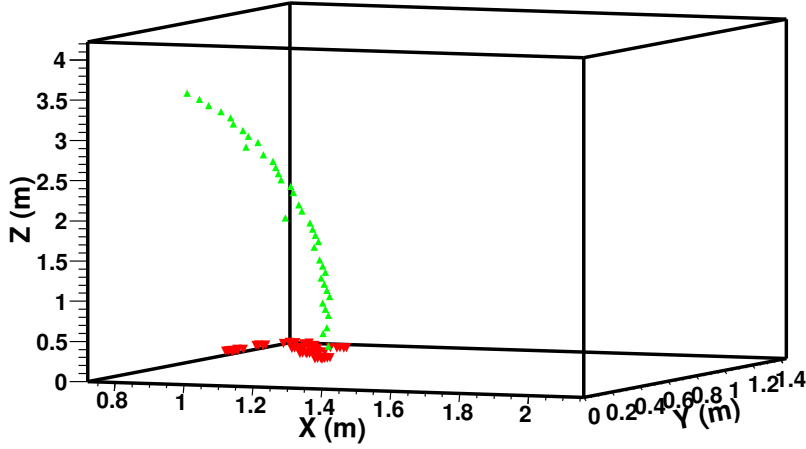


Figure 3.1: Sample track of a 10 GeV neutrino event generating a 5.1 GeV muon track and associated hadron shower in the ICAL detector

3.2 Response of ICAL to muons

We propagate 10000 muons uniformly from a vertex randomly located in the central region of the central module of the detector. We study the number of tracks reconstructed, the direction reconstruction, including up/down discrimination, momentum and zenith angle resolution.

3.2.1 Momentum resolution

The momentum resolution, R , is defined (with its error δR) in terms of the RMS width σ of the histogram of reconstructed momentum, P_{rec} , as,

$$R \equiv \sigma/P_{in}, \quad (3.1)$$

$$\delta R/R = \delta\sigma/\sigma.$$

Low energy distribution are fitted with a convolution of Landau and Gaussian probability functions because they have asymmetric tail. Figure of such distribution has been shown in Fig 3.2.

While the histograms at higher energies show no asymmetric tails, they fit poorly with

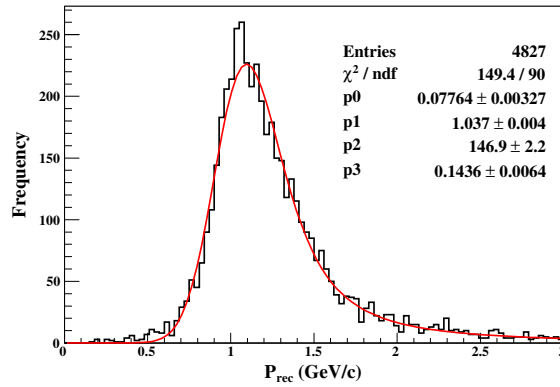


Figure 3.2: Momentum distributions for $(P_{\text{in}}, \cos \theta) = (1 \text{ GeV}/c, 0.65)$ fitted with Landau convoluted Gaussian; this fits better than a pure Gaussian at lower energies, $P_{\text{in}} \leq 2 \text{ GeV}/c$.

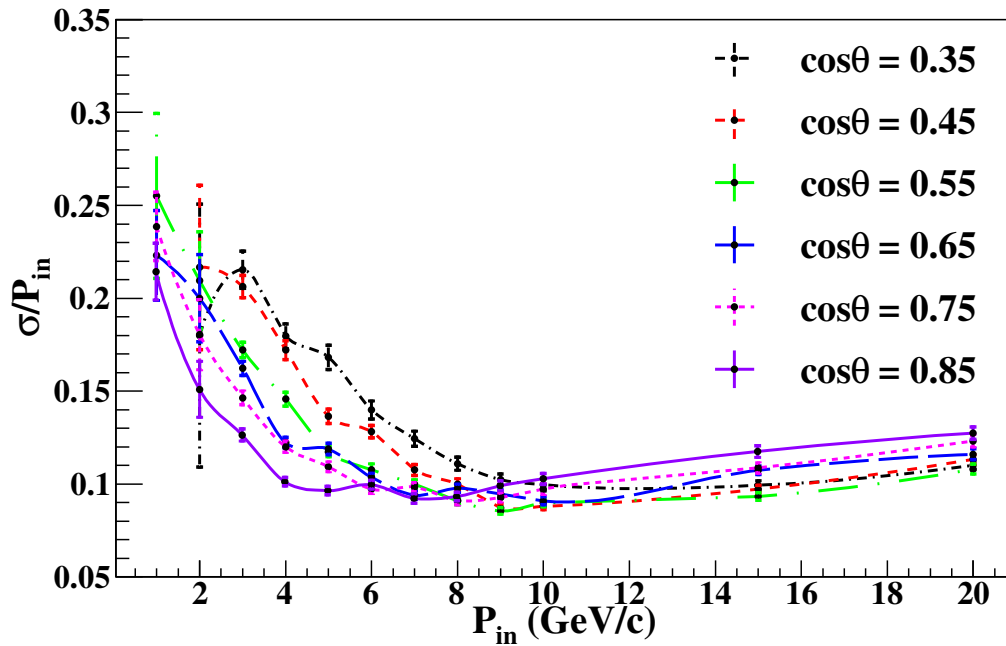


Figure 3.3: Muon resolution as a function of input momentum and $\cos \theta$.

Gaussian probability distribution. In the case of Landau-Gauss fits, the width is defined as $\sigma \equiv \text{FWHM}/2.35$, where $\text{FWHM} = \text{Full Width at Half Maximum}$, in order to make a consistent and meaningful comparison with the Gaussian fits at higher energies, where the square root of the variance or the RMS width equals $\text{FWHM}/2.35$.

The momentum resolution as a function of input momentum for different values of $\cos \theta$ is shown in Fig 3.3 for momenta from 1–20 GeV/c. It can be seen that initially (upto about 6 GeV/c), the resolution improves with increasing energy. This is because, at such small momenta, as the momentum increases, the number of RPC layers crossed by the muons also increases, thus increasing the number of layers and hits; in addition, the magnetic field causes appreciable bending so the accuracy of momentum reconstruction also increases. Thus the resolution improves. As the input momentum increases further, the particle begins to exit the detector, so that only a partial track is contained in the detector; this comprises relatively straight sections since the radius of curvature increases with momentum, resulting in a poorer fit. Due to this the resolution then worsens as the input energy increases.

3.2.2 Zenith angle resolution

The θ resolution is the width obtained by fitting the reconstructed zenith angle distribution with Gaussian probability distribution functions (pdf). The events distribution as a function of the reconstructed θ is shown in Fig 3.4 for a sample input $(P_{\text{in}}, \cos \theta_{\text{in}}) = (5 \text{ GeV/c}, 0.65)$. It is seen that the distribution is very narrow, less than a degree, indicating a good angular resolution for muons.

The θ resolution is shown as a function of input momentum for different zenith angles in Fig 3.5. The resolution quickly improves with input momentum, being better than a degree for all input angles for $P_{\text{in}} > 4 \text{ GeV/c}$. Beyond 10 GeV/c, the curves approximately coincide.

3.2.3 Reconstruction efficiency

The momentum reconstruction efficiency (ϵ_{rec}) is defined as the ratio of the number of reconstructed events, n_{rec} (irrespective of charge), to the total number of generated events, N_{total} . We have

$$\epsilon_{\text{rec}} = \frac{n_{\text{rec}}}{N_{\text{total}}}, \quad (3.2)$$

and its error, $\delta\epsilon_{\text{rec}} = \sqrt{\epsilon_{\text{rec}}(1 - \epsilon_{\text{rec}})/N_{\text{total}}}$.

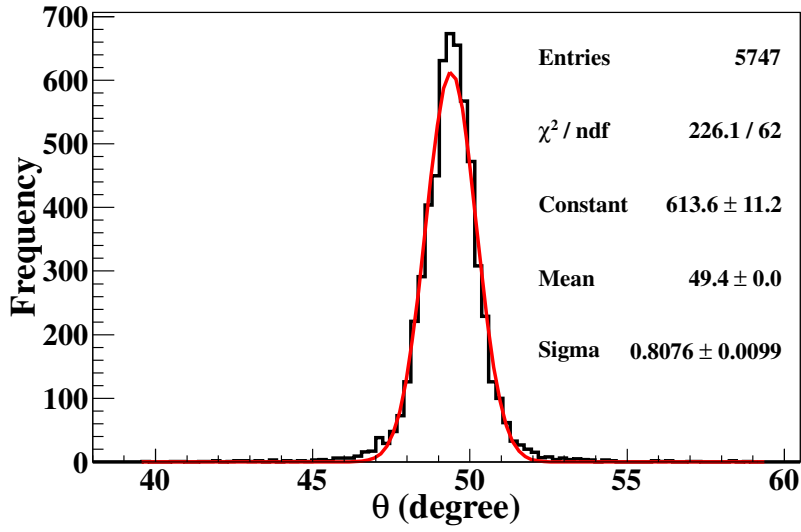


Figure 3.4: Reconstructed angular distribution for input $(P_{\text{in}}, \cos \theta_{\text{in}}) = (5 \text{ GeV}/c, 0.65)$; $\theta = 49.46^\circ$.

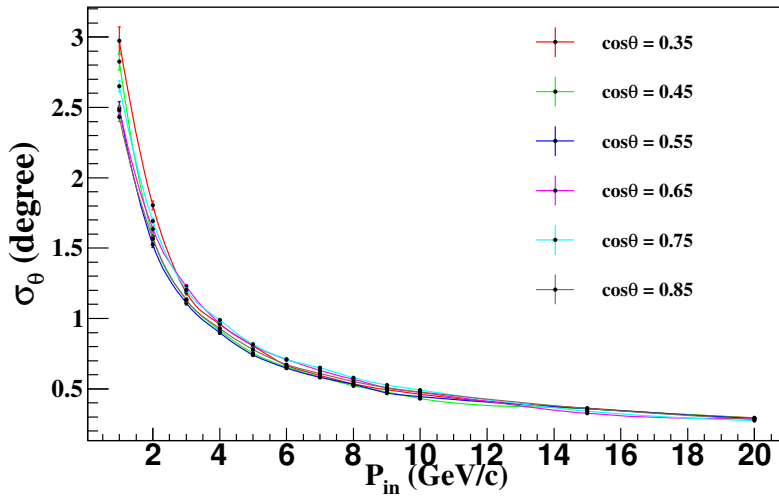


Figure 3.5: Angular resolution in degrees as a function of input momentum.

Fig. 3.6 shows the muon momentum reconstruction efficiency as a function of input momentum for different $\cos \theta$ bins. The momentum reconstruction efficiency is somewhat smaller than the track reconstruction efficiency, especially at smaller angles. It is seen that the efficiency of momentum reconstruction depends on the energy of the incident particle, the strength of the magnetic field, the angle of propagation, etc.

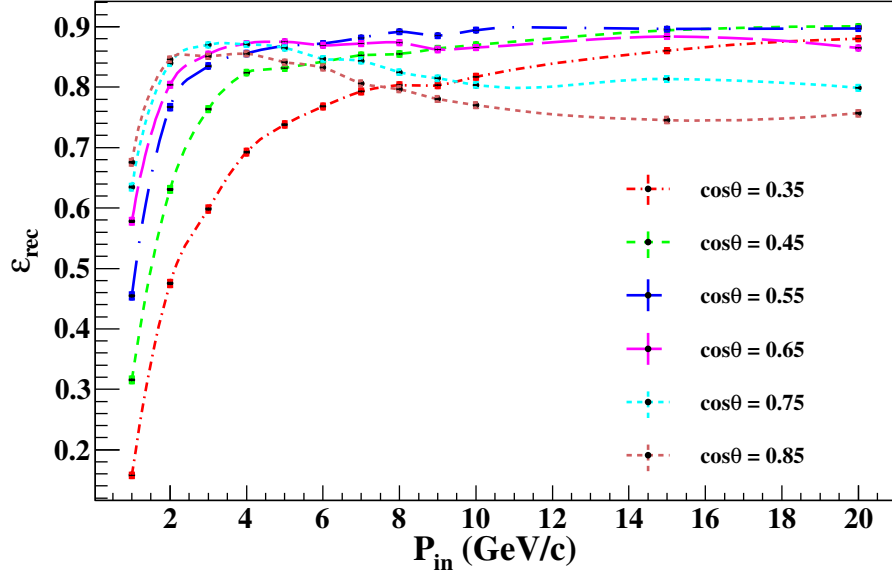


Figure 3.6: Momentum reconstruction efficiency as a function of the input momentum for different $\cos\theta$ values.

Momentum values below 4 GeV/c as the input momentum increases, the reconstruction efficiency increases for all angles, since the number of hits increases as the particle crosses more number of layers. At larger angles, the reconstruction efficiency for small energies is smaller compared to vertical angles since the number of hits for reconstructing tracks is less. But as the input energy increases, since the particle crosses more number of layers, the efficiency of reconstructing momentum also increases and becomes comparable with vertical angles. At higher energies the reconstruction efficiency becomes almost constant. The drop in efficiency at high energies for vertical muons is due to the track being partially contained as well as the requirement of single track being reconstructed.

3.2.4 Relative charge identification efficiency

The charge of the particle is determined from the direction of curvature of the track in the magnetic field. Relative charge identification efficiency is defined as the ratio of number of events with correct charge identification, n_{cid} , to the total number of reconstructed

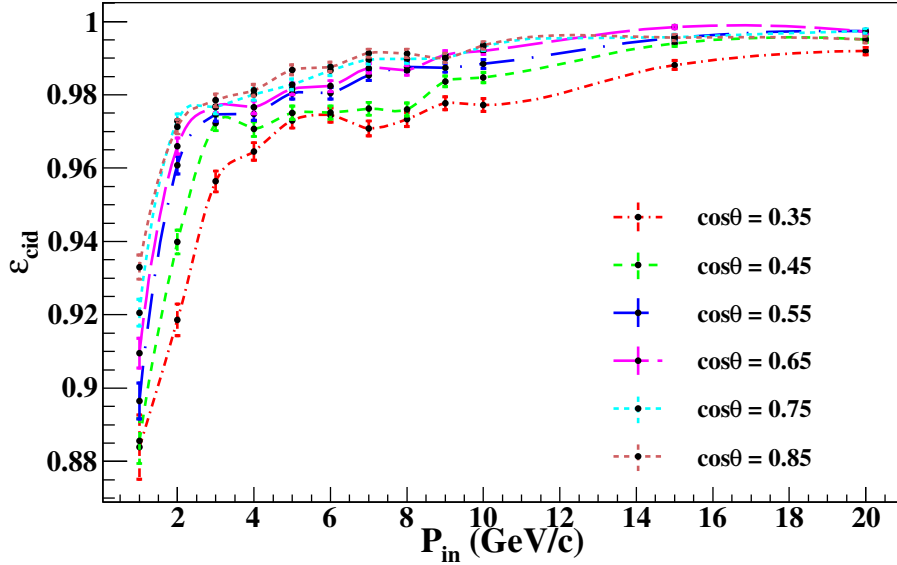


Figure 3.7: The relative charge identification efficiency as a function of the input momentum for different $\cos\theta$ values. Note that the y -axis range is 0.87–1 and does not start from zero.

events, i.e.,

$$\epsilon_{\text{cid}} = \frac{n_{\text{cid}}}{n_{\text{rec}}}, \quad (3.3)$$

with error, $\delta\epsilon_{\text{cid}} = \sqrt{\epsilon_{\text{cid}}(1 - \epsilon_{\text{cid}})/n_{\text{rec}}}$.

The total reconstructed events also includes those which are reconstructed in the wrong θ quadrant. Fig. 3.7 shows the relative charge identification efficiency as a function of input momentum for different polar angles $\cos\theta$. Here we consider the number of reconstructed events after applying the additional selection criterion. A marginally worse charge identification efficiency is obtained for vertical events ($\cos\theta = 0.85$) when this additional criterion is not applied, while results at other angles are virtually the same.

The muon undergoes multiple scattering during propagation in the detector; for small momentum, since the number of layers with hits is small, this may lead to an incorrectly reconstructed direction of bending, resulting in the wrong charge identification. Hence the charge identification efficiency is relatively poor at lower energies, as can be seen from Fig. 3.7. As the energy increases the length of the track also increases due to which the

charge identification efficiency also improves. Beyond a few GeV/ c , the charge identification efficiency becomes roughly constant, about 98–99%. While this is expected to hold up to $P_{\text{in}} \sim 50$ GeV/ c or more, the momentum resolution at such high momenta will be much worse; but this is outside the scope of the present study.

Chapter 4

Octant sensitivity at ICAL

In Neutrino physics, most interesting unresolved questions are Neutrino mass hierarchy determination, θ_{23} Octant degeneracy and measurement of CP violation. The recent measurement of a non-zero value of the mixing angle θ_{13} by the reactor experiments Double-Chooz [27], Daya-Bay [25] and RENO [26] heralds a major breakthrough in the advancement of neutrino physics. Non zero value of the θ_{13} has opened up the possibility of answering the major questions in neutrino oscillation physics. The large value of $\sin^2 2\theta_{13}$ will mostly enhance the possibility of determining the neutrino mass hierarchy. Precision measurement of θ_{13} and mass hierarchy will help to determine the true octant of θ_{23} . In the PMNS matrix δ_{CP} occurs with the mixing angle θ_{13} , hence moderate large value of θ_{13} is expected to be conducive for the measurement of δ_{CP} .

The mixing angle $\sin^2 2\theta_{23}$ is mainly determined by the SuperKamiokande (SK) atmospheric neutrino data. However the octant in which this mixing angle lies is not yet decisively determined by the data. A full three-flavour fit to the SK data gives the best-fit for NH in the lower octant (LO) and IH in the higher octant (HO) keeping θ_{13} as a free parameter in the analysis [95].

The octant degeneracy means impossibility of distinguishing between θ_{23} and $\pi/2 - \theta_{23}$. This is generic and robust for vacuum oscillation probabilities that are functions of $\sin^2 2\theta_{23}$, e.g. the two flavour muon survival probability in vacuum [96]. If on the other hand the leading term in the probability are functions of $\sin^2 \theta_{23}$ (e.g. $P_{\mu e}$) then the inherent octant degeneracy is not there but lack of knowledge of other parameters like θ_{13} and δ_{CP} can give rise to octant degeneracy [97, 98]. These issues may affect the octant sensitivity of the long baseline experiments T2K and NO ν A where the matter effect is not

very significant and in particular resonant matter effects do not get a chance to develop. Although conventionally the octant degeneracy refers to the indistinguishability of θ_{23} and $\pi/2 - \theta_{23}$, in view of the present uncertainty in the measurement of θ_{23} the scope of this can be generalized to any value of θ_{23} in the wrong octant within its allowed range. In this chapter by octant sensitivity we refer to this "generalized" definition. If in addition the hierarchy is unknown then there can also be the wrong-octant–wrong-hierarchy solutions and one needs to marginalize over the wrong hierarchy as well.

Atmospheric neutrinos pass through long distances in matter and they span a wide range in energy and can encounter resonant matter effects. In this case the octant sensitivity in $P_{\mu\mu}$ ensues from the term $\sin^4 \theta_{13} \sin^2 2\theta_{13}^m$ [99]. $P_{\mu e}$ in matter contains $\sin^2 \theta_{13} \sin^2 2\theta_{13}^m$. Since at resonance $\sin^2 2\theta_{13}^m \approx 1$, the octant degeneracy can be removed.

Atmospheric neutrinos provide fluxes of both neutrinos and antineutrinos as well as neutrinos of both electron and muon flavour. On one hand it provides the advantage of observing both electron and muon events. However on the other hand a particular type of event gets contributions from both disappearance and appearance probabilities. This can be a problem if the matter effects for these two channels go in opposite directions. Thus it is necessary to carefully study the various contributions and ascertain what may be the best possibility to decode the imprint of matter effects in atmospheric neutrino propagation.

In this chapter we study in detail the possibility of removal of octant degeneracy in view of the precise measurement of a relatively large value of θ_{13} . We examine the octant sensitivity in the long baseline experiments T2K and NO ν A and in the atmospheric neutrino experiment ICAL, as well as the combined sensitivity of these experiments. In particular we address whether degeneracy due to θ_{13} can still affect octant determination at the current level of precision of this parameter.

The plan of the chapter is as follows. In Section 4.1, we discuss the octant degeneracy at the level of oscillation and survival probabilities, for baselines corresponding to both atmospheric neutrinos and those relevant to NO ν A and T2K. Section 4.2 discusses the simulation of atmospheric neutrinos. In Section 4.3, we discuss the results. First we discuss the octant sensitivity in ICAL detector. Next we describe the results obtained for octant sensitivity using NO ν A and T2K. Finally we present combined octant sensitivity of long baseline and ICAL experiment.

4.1 Octant degeneracy in neutrino oscillation probability

The ambiguity in the determination of the octant of θ_{23} may appear in the oscillation and survival probabilities as

(a) the intrinsic octant degeneracy, in which the probability is a function of $\sin^2 2\theta_{23}$ and hence the measurement cannot distinguish between θ_{23} and $\pi/2 - \theta_{23}$,

$$P(\theta_{23}^{tr}) = P(\pi/2 - \theta_{23}^{tr}) \quad (4.1)$$

(b) the degeneracy of the octant with other neutrino parameters, which confuses octant determination due to the uncertainty in these parameters. In particular, this degeneracy arises in probabilities that are functions of $\sin^2 \theta_{23}$ or $\cos^2 \theta_{23}$. For such cases $P(\theta_{23}^{tr}) \neq P(\pi/2 - \theta_{23}^{tr})$. However for different values of the parameters θ_{13} and δ_{CP} the probability functions become identical for values of θ_{23} in opposite octants for different values of these parameters, i.e.

$$P(\theta_{23}^{tr}, \theta_{13}, \delta_{CP}) = P(\pi/2 - \theta_{23}^{tr}, \theta'_{13}, \delta'_{CP}), \quad (4.2)$$

where θ_{23}^{tr} denotes the true value of the mixing angle and the primed and unprimed values of θ_{13} and δ_{CP} lie within the current allowed ranges of these parameters.

In the case of δ_{CP} , this covers the entire range from 0 to 2π , while for θ_{13} the current 3σ range is given by $\sin^2 2\theta_{13} = 0.07 - 0.13$. From the above equation it is evident that even if θ_{13} is determined very precisely, this degeneracy can still remain due to complete uncertainty in the CP phase. In fact, the scope of this degeneracy can be enlarged to define this as

$$P(\theta_{23}^{tr}, \theta_{13}, \delta_{CP}) = P(\theta_{23}^{wrong}, \theta'_{13}, \delta'_{CP}) \quad (4.3)$$

where θ_{23}^{wrong} denote values of the mixing angle in the opposite octant.

The features of the octant degeneracy and the potential for its resolution in different neutrino energy and baseline ranges can be understood from the expressions for the oscillation and survival probabilities relevant to specific ranges. We discuss below the probability expressions in the context of the fixed baseline experiments NO ν A/T2K and for atmospheric neutrino experiment.

4.1.1 Ambiguity in $P_{\mu e}$ and $P_{\mu\mu}$

For NO ν A/T2K, the baselines are 812 and 295 Km respectively and the peak energies of the beams are in the range 0.5-2 GeV. For these values of baselines, the earth matter density is in the range 2.3 – 2.5 g/cc, and the corresponding matter resonance energies are above 10 GeV. Hence the neutrino energies of both experiments lie well below matter resonance, and the oscillation probabilities will only display small sub-leading matter effects. The expressions of the relevant probabilities $P_{\mu\mu}$ and $P_{\mu e}$ in using one-mass scale dominant (OMSD) approximation are given in equations 1.18 and 1.19 respectively ,

The probability expressions have sub-leading corrections corresponding to small matter effect terms and the solar mass-squared difference [16–20]. We observe the following salient features from these expressions:

(a) The disappearance channel $P_{\mu\mu}$ has in its leading order a dependence on $\sin^2 2\theta_{23}$, and hence is dominated by the intrinsic octant degeneracy. There is a small θ_{13} -dependent correction in the measurement of θ_{23} which gives a minor ($\sim 1\%$) resolution of the degeneracy if θ_{13} is known precisely.

(b) The appearance channel $P_{\mu e}$ has the combination of parameters $\sin^2 \theta_{23} \sin^2 2\theta_{13}$, and hence does not suffer from the intrinsic octant degeneracy. However, the degeneracy of the octant with the parameter θ_{13} comes into play, since the above combination may be invariant for opposite octants for different values of θ_{13} , and hence this degeneracy cannot get lifted with a measurement from such experiments alone [100]. This channel can be also affected by the large uncertainty in δ_{CP} when sub-leading corrections are included.

For atmospheric neutrinos, the relevant baselines and energies are in the range 1000 - 12500 Km and 1 - 10 GeV respectively. A large region in this L and E space exhibits strong resonant earth matter effects, since the earth densities in this baseline range (3 - 8 g/cc) correspond to resonance energies $E_{\text{res}} = 4 - 9$ GeV. Hence the relevant probability expressions $P_{\mu e}^m$, P_{ee}^m and $P_{\mu\mu}^m$ can be written, in the OMSD approximation and with full matter effects, as [17, 101]

$$P_{\mu e}^m = \sin^2 \theta_{23} \sin^2 2\theta_{13}^m \sin^2 \left[1.27 (\Delta m_{31}^2)^m \frac{L}{E} \right] \quad (4.4)$$

$$\begin{aligned}
P_{\mu\mu}^m = & 1 - \cos^2 \theta_{13}^m \sin^2 2\theta_{23} \sin^2 \left[1.27 \left(\frac{\Delta m_{31}^2 + A + (\Delta m_{31}^2)^m}{2} \right) \frac{L}{E} \right] \\
& - \sin^2 \theta_{13}^m \sin^2 2\theta_{23} \sin^2 \left[1.27 \left(\frac{\Delta m_{31}^2 + A - (\Delta m_{31}^2)^m}{2} \right) \frac{L}{E} \right] \\
& - \sin^4 \theta_{23} \sin^2 2\theta_{13}^m \sin^2 \left[1.27 (\Delta m_{31}^2)^m \frac{L}{E} \right]
\end{aligned} \tag{4.5}$$

$$P_{ee}^m = 1 - \sin^2 2\theta_{13}^m \sin^2 \left[1.27 (\Delta m_{31}^2)^m \frac{L}{E} \right] \tag{4.6}$$

The following features can be observed from the probability expressions:

(a) The oscillation probability in matter $P_{\mu e}^m$ is still guided to leading order by a dependence on $\sin^2 \theta_{23}$. But strong resonant earth matter effects help in resolving the degeneracy since the mixing angle θ_{13} in matter gets amplified to maximal values (close to 45°) near resonance. The combination $\sin^2 \theta_{23} \sin^2 2\theta_{13}^m$ no longer remains invariant over opposite octants, since $\sin^2 2\theta_{13}^m$ becomes close to 1 in both octants irrespective of the vacuum value of θ_{13} . This breaks the degeneracy of the octant with θ_{13} .

(b) The muon survival probability in matter $P_{\mu\mu}^m$ has leading terms proportional to $\sin^2 2\theta_{23}$, as in the vacuum case, which could give rise to the intrinsic octant degeneracy. But the strong octant-sensitive behaviour of the term $\sin^4 \theta_{23} \sin^2 2\theta_{13}^m$ near resonance can override the degeneracy present in the $\sin^2 2\theta_{23}$ -dependent terms.

(c) The electron survival probability P_{ee}^m is independent of θ_{23} and hence does not contribute to the octant sensitivity.

In the following discussion, we address the octant degeneracy due to θ_{23} in the wrong octant, θ_{13} and unknown values of δ_{CP} , at a probability level. The probability figures are drawn by solving the full three flavour propagation equation of the neutrinos in matter using PREM density profile [22]. In all these figures the left panels are for the NO ν A peak energy and baseline (2 GeV, 812 Km), while the right panels are for a typical atmospheric neutrino energy and baseline (6 GeV, 5000 Km). The top row denotes the appearance channel $P_{\mu e}$, while the bottom row denotes the disappearance channel $P_{\mu\mu}$.

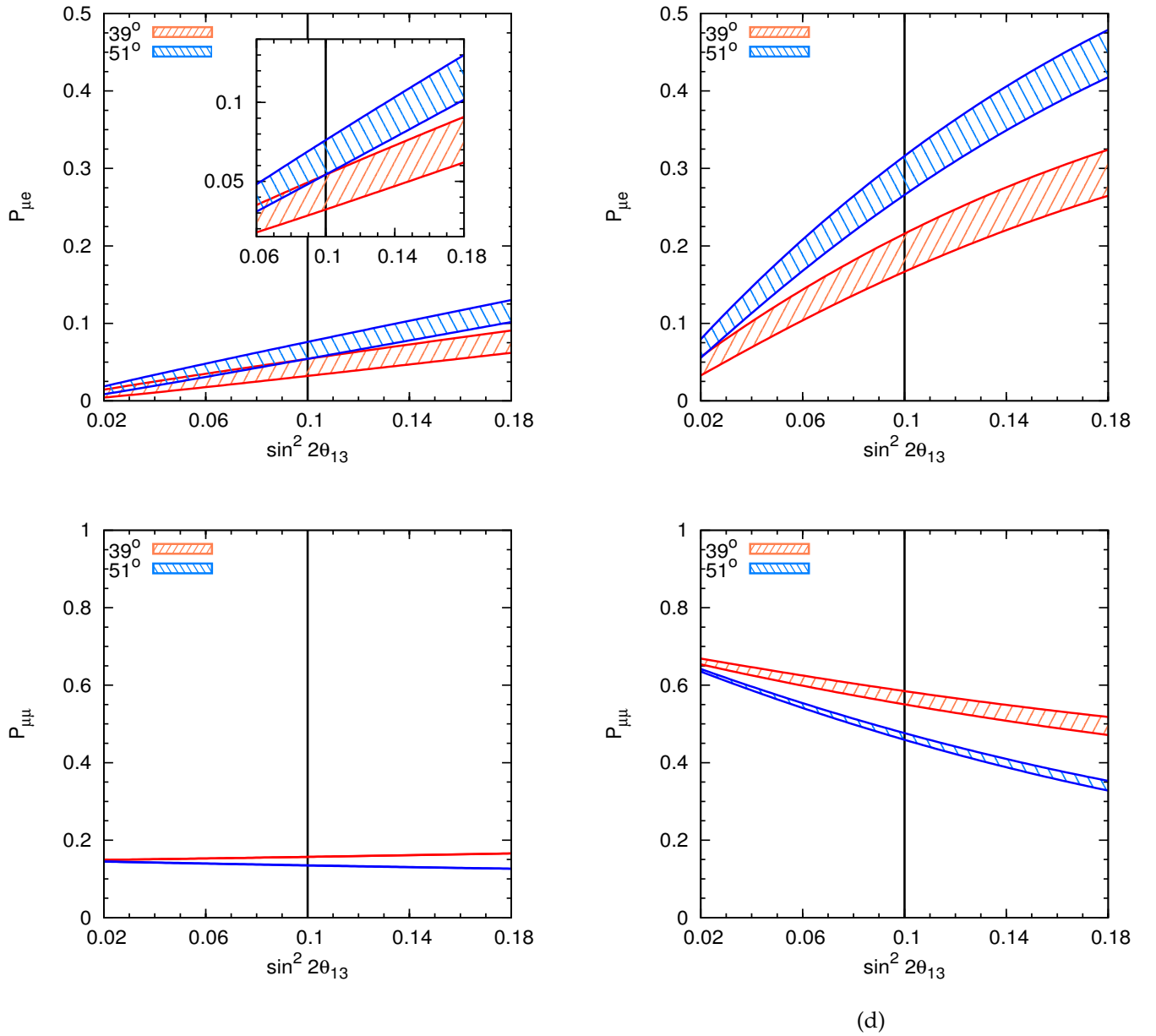


Figure 4.1: Behaviour of the muon survival and oscillation probabilities as a function of $\sin^2 2\theta_{13}$ showing the θ_{23} octant degeneracy and its breaking. The left panels are for the NO ν A peak energy and baseline (2 GeV, 812 Km), while the right panels are for a typical atmospheric neutrino energy and baseline (6 GeV, 5000 Km). The top row denotes the appearance channels $P_{\mu e}$ and $P_{e\mu}$, while the bottom row denotes the disappearance channel $P_{\mu\mu}$. The values of oscillation parameters chosen are $\theta_{23}^{tr} = 39^\circ$, $\theta_{23}^{wrong} = 51^\circ$. The bands denote a variation over the full range of the phase δ_{CP} . The inset shows the region of separation of the bands near $\sin^2 2\theta_{13} = 0.1$.

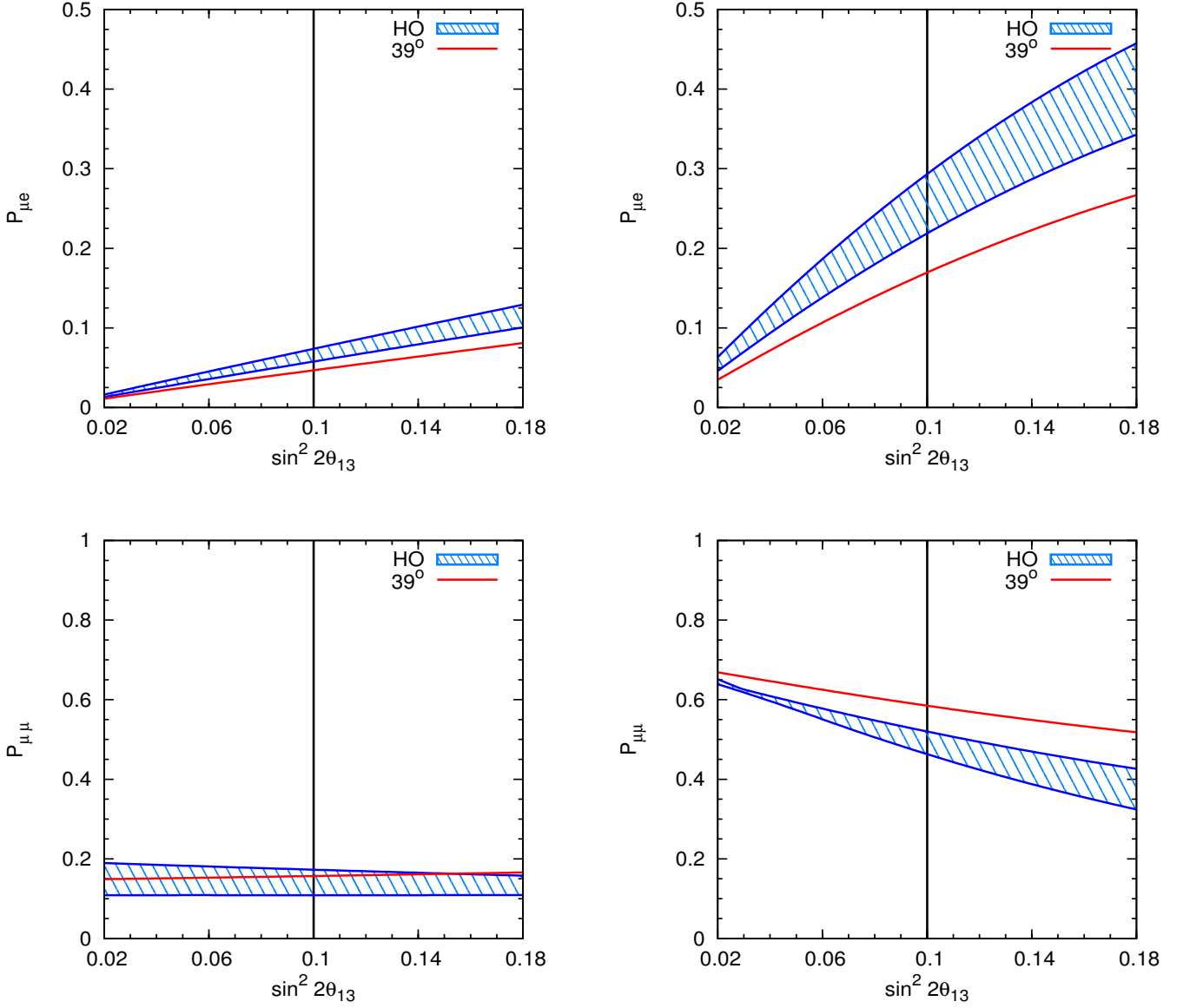


Figure 4.2: Same as Figure 4.1 with a fixed true and test $\delta_{CP} = 0$ and true $\theta_{23}^{tr} = 39^\circ$, with the band denoting a variation over the full allowed range of $\theta_{23}^{wrong} = 45^\circ$ to 54° in the wrong octant.

Fig 4.1 depicts the probabilities $P_{\mu e}$ and $P_{\mu\mu}$ as a function of $\sin^2 2\theta_{13}$ for $\theta_{23}^{tr} = 39^\circ$ and $\theta_{23}^{wrong} = 51^\circ$. The bands show the probability range in each case when δ_{CP} is varied over its full range (0 to 2π). For a given fixed value of $\sin^2 2\theta_{13}$, the distinction between θ_{23} in the two octants can be gauged from the separation of the two bands along the relevant vertical line. The left panels show that for $P_{\mu e}$, the δ_{CP} bands overlap and the two hierarchies cannot be distinguished till nearly $\sin^2 2\theta_{13} = 0.1$. The inset in the upper

left panel shows the region of separation of the bands near $\sin^2 2\theta_{13} = 0.1$ in detail. Hence the knowledge of the parameter θ_{13} upto its current level of precision becomes crucial, since a θ_{13} range including lower values would wash out the octant sensitivity derivable from such experiments due to the combined degeneracy with θ_{13} and δ_{CP} . For $P_{\mu\mu}$, the intrinsic degeneracy predominates and the effect of δ_{CP} variation is insignificant.

For the 5000 km baseline, due to the resonant matter effects breaking the octant degeneracy at the leading order, both $P_{\mu e}$ and $P_{\mu\mu}$ show a wider separation between the opposite-octant bands, even for small values of θ_{13} . This is due to the $\sin^2 \theta_{23} \sin^2 2\theta_{13}^m$ ($\sin^4 \theta_{23} \sin^2 2\theta_{13}^m$) term in $P_{\mu e}$ ($P_{\mu\mu}$). The δ_{CP} bands in the right-hand panels are much wider because of the enhancement of the subleading terms due to matter effects. However, the enhancement is more for the leading order term which alleviates the degeneracy with δ_{CP} .

Fig 4.2 shows the probabilities $P_{\mu e}$ and $P_{\mu\mu}$ as a function of $\sin^2 2\theta_{13}$. We have held fixed, true and test $\delta_{CP} = 0$ and true $\theta_{23}^{tr} = 39^\circ$, with the band denoting a variation over the full allowed range of $\theta_{23}^{wrong} = 45^\circ$ to 54° in the wrong octant. Thus this figure reveals the effect of the uncertainty in the measurement of θ_{23} in the determination of octant, for a given value of $\sin^2 2\theta_{13}$. For the $\text{NO}\nu\text{A}$ baseline, the survival probability $P_{\mu\mu}$ shows an overlap of the test θ_{23} band with the true curve, while in the probability $P_{\mu e}$ there is a small separation. Fig 4.1 and 4.2 thus indicate that for the $\text{NO}\nu\text{A}$ baseline, the octant sensitivity from $P_{\mu e}$ is more affected by the uncertainty in δ_{CP} and less by the test θ_{23} variation, while for $P_{\mu\mu}$ the opposite is true.

The plots for the atmospheric neutrino baseline show a clear breaking of the octant degeneracy in both $P_{\mu e}$ and $P_{\mu\mu}$ even for small values of θ_{13} , indicating that the octant sensitivity from the atmospheric neutrino signal is stable against the variation of both δ_{CP} and the test value of θ_{23} , even for small values of θ_{13} .

We will now discuss the effect of precision measurement of θ_{13} on the determination of octant degeneracy. In Fig 4.3, the energy spectra of the probabilities $P_{\mu e}$ and $P_{\mu\mu}$ are plotted. The figure shows the variation in the probabilities in each case when $\sin^2 2\theta_{13}$ is varied over three values $\sin^2 2\theta_{13} = 0.07, 0.1$ and 0.13 covering the current allowed range, and for two illustrative values of θ_{23} 39° and 51° in opposite octants. The value of δ_{CP} is fixed to be 0. The figure indicates that the separation of the Lower Octant(LO) and Higher Octant(HO) curves and hence the octant sensitivity depends on the value of $\sin^2 2\theta_{13}$ in opposite ways depending on whether the true θ_{23} value lies in the higher or lower octant.

In $P_{\mu e}$, for $\theta_{23}^{tr} = 39^\circ$, lower values of true $\sin^2 \theta_{13}$ can give a higher octant sensitivity since they are more separated from the band of variation of the probability over the whole

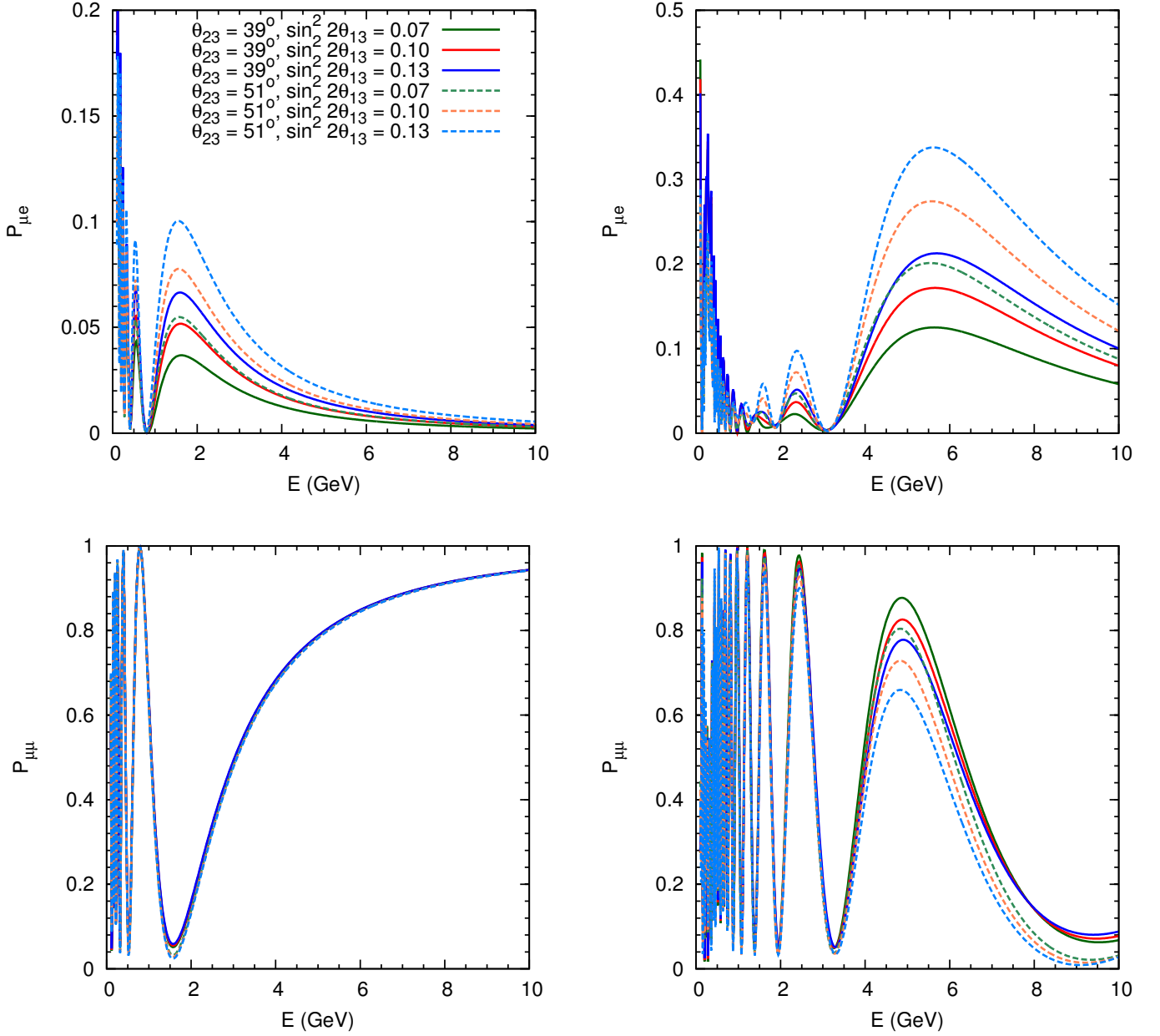


Figure 4.3: Energy spectra of the probabilities $P_{\mu e}$ and $P_{\mu\mu}$ for the NO ν A baseline (left panels) and for a sample atmospheric neutrino baseline 5000 Km (right panels). The figure shows the variation in the probabilities in each case when $\sin^2 2\theta_{13}$ is varied over three values in the current allowed range, fixing the true and test θ_{23} values $\theta_{23}^{tr} = 39^\circ$ and $\theta_{23}^{wrong} = 51^\circ$. δ_{CP} is fixed to 0.

range of test $\sin^2 2\theta_{13}$, and as true $\sin^2 2\theta_{13}$ increases the degeneracy with the wrong θ_{23} band becomes more prominent. For $\theta_{23}^{tr} = 51^\circ$, the opposite is true, i.e. higher values of $\sin^2 2\theta_{13}^{tr}$ have a better separation with the wrong θ_{23} band. For example, for the NO ν A

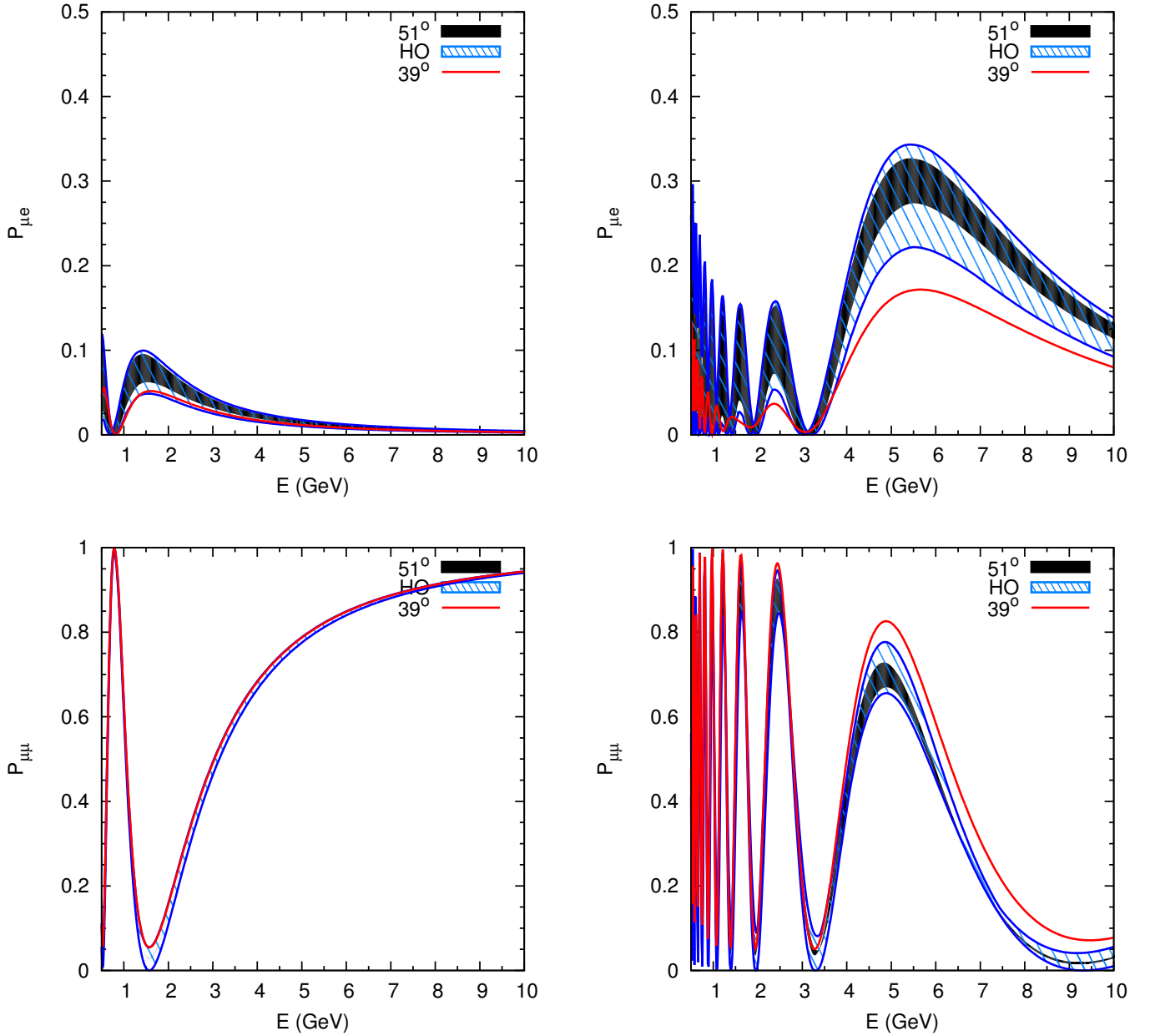


Figure 4.4: Energy spectra of the probabilities $P_{\mu e}$ and $P_{\mu\mu}$ for the NO ν A baseline (left panels) and for a sample atmospheric neutrino baseline 5000 Km (right panels). The figure shows the variation in the probabilities in each case when θ_{23}^{wrong} is varied over the entire allowed range in the wrong octant, as well as varying the test δ_{CP} , fixing the true values $\theta_{23}^{tr} = 39^\circ$ and $\delta_{CP}^{tr} = 0$ in the solid curve. The spread due to variation of both test parameters is denoted by the blue band. The black band shows the variation with test δ_{CP} for a fixed $\theta_{23}^{wrong} = 51^\circ$.

baseline, if $\theta_{23}^{tr} = 39^\circ$, the $P_{\mu e}$ curve for $\sin^2 2\theta_{13}^{tr} = 0.07$ is well-separated from the band for $\theta_{23}^{wrong} = 51$, while the curve for $\sin^2 2\theta_{13}^{tr} = 0.1$ is seen to be just separated from it,

and the $\sin^2 2\theta_{13}^{tr} = 0.13$ curve lies entirely within the band of test $\sin^2 2\theta_{13}$ variation with the wrong octant. But if $\theta_{23}^{tr} = 51^\circ$, the $\sin^2 2\theta_{13}^{tr} = 0.07$ curve suffers from the degeneracy while the curves for $\sin^2 2\theta_{13}^{tr} = 0.1$ and upwards lie clearly outside the θ_{23}^{wrong} band. For $P_{\mu\mu}$, the effect of θ_{13} on the separation between the opposite octant bands is less, since the behaviour is governed by the intrinsic octant degeneracy.

For the 5000 km baseline, due to strong matter effects, the separation of the true and wrong θ_{23} bands is much better, and only the highest (lowest) values of $\sin^2 2\theta_{13}^{tr}$ suffer from a degeneracy with the wrong octant for $P_{\mu e}$ if the true octant is lower (higher), for $P_{\mu\mu}$, the behaviour is reversed.

Fig 4.4 again depicts the energy spectra of the probabilities $P_{\mu e}$ and $P_{\mu\mu}$. This figure shows the variation in the probabilities in each case when θ_{23}^{wrong} is varied over the entire allowed range in the wrong octant, as well as varying the test δ_{CP} , fixing $\theta_{23}^{tr} = 39^\circ$ and $\delta_{CP}^{tr} = 0$. The solid black band denotes the variation with test δ_{CP} for a fixed $\theta_{23}^{wrong} = 51^\circ$.

For the NO ν A baseline, the test probability bands show an almost complete overlap with the $\theta_{23}^{tr} = 39^\circ, \delta_{CP}^{tr} = 0$ curve. However, the octant sensitivity may still be retained due to spectral information. So there always exist specific energy regions and bins from which the octant sensitivity can be derived.

At 5000 km, the minimum separation between octants does not occur at or near $\theta_{23}^{wrong} = 90^\circ - \theta_{23}^{tr} = 51^\circ$ as can be seen from the solid black shaded region. The edge of the striped blue band corresponding to some other value of θ_{23} is closest to the 'true' curve and well-separated from it. This shows that there is octant sensitivity for this baseline even after including the uncertainty in δ_{CP} and θ_{23} .

4.2 Simulation of atmospheric neutrinos at ICAL

Simulation of atmospheric neutrinos can be categorised in two different steps:1) Atmospheric neutrino event generation 2) Statistical procedure.

4.2.1 Atmospheric neutrino event generation

The neutrino and anti-neutrino CC events are obtained by folding the incident neutrino fluxes with the appropriate probabilities, relevant CC cross sections, the detector efficiency, resolution, mass and the exposure time. We have taken HONDA et.al. fluxes [102] for the analysis.

The μ^- event rate in a specific energy bin of width dE and the angle bin of width $d\Omega$ can be written as :

$$\frac{d^2N_\mu}{d\Omega dE} = \frac{1}{2\pi} \left[\left(\frac{d^2\Phi_\mu}{d \cos \theta dE} \right) P_{\mu\mu} + \left(\frac{d^2\Phi_e}{d \cos \theta dE} \right) P_{e\mu} \right] \sigma_{CC} D_{\text{eff}} \quad (4.7)$$

Here $\Phi_{\mu,e}$ are the atmospheric fluxes (ν_μ and ν_e), σ_{CC} is the total CC cross section and D_{eff} is the detector efficiency. Similarly μ^+ event rate can be obtained from anti-neutrino.

We have considered the smearing in both energy and angle, assuming a Gaussian form of resolution function, R . The energy resolution function, we use,

$$R_{\text{EN}}(E_t, E_m) = \frac{1}{\sqrt{2\pi}\sigma} \exp \left[-\frac{(E_m - E_t)^2}{2\sigma^2} \right] \quad (4.8)$$

E_m and E_t denote the measured and true values of energy respectively. The smearing width σ is a function of E_t . The function of σ used as, $\sigma = 0.1\sqrt{E_t}$. We have used optimistic resolution, while muon resolution of the ICAL detector is approximately $\sigma = 0.1E_t$.

Angular smearing function is given by,

$$R_\theta(\theta_t, \theta_m) = N \exp \left[-\frac{(\theta_t - \theta_m)^2 + \sin^2 \theta_t (\phi_t - \phi_m)^2}{2(\Delta\theta)^2} \right] \quad (4.9)$$

where N is a normalisation constant. θ_t and θ_m denote the true and measured values of angle respectively and $\Delta\theta$ is the smearing width. The value of $\Delta\theta = 10^\circ$. We have integrated the ϕ from 0 to 2π .

Now, the ν_μ event rate with the smearing factors taken into account is given by,

$$\frac{d^2N_\mu}{d\Omega_m dE_m} = \frac{1}{2\pi} \int \int dE_t d\Omega_t R_{\text{EN}}(E_t, E_m) R_\theta(\Omega_t, \Omega_m) [\Phi_\mu^d P_{\mu\mu} + \Phi_e^d P_{e\mu}] \sigma_{CC} D_{\text{eff}} \quad (4.10)$$

where we have denoted $(d^2\Phi/d \cos \theta dE)_{\mu,e} \equiv \Phi_{\mu,e}^d$ and D_{eff} is the detector efficiency.

4.2.2 Statistical procedure

The difference between the events with two different sets of parameters has been calculated in terms of χ^2 . The χ^2 for a fixed set of parameters is done using the method of pulls,

which allows us to take into account the various statistical and systematic uncertainties. The flux, cross-sections and other systematic uncertainties are taken into account in the computation of N_{ij}^{th} . Let the k^{th} input deviate from its standard value by $\sigma_k \xi_k$, where σ_k is its uncertainty. Then the value of N_{ij}^{th} with the changed inputs is given by,

$$N_{ij}^{\text{th}} = N_{ij}^{\text{th}}(\text{std}) + \sum_{k=1}^{\text{npull}} c_{ij}^k \xi_k \quad (4.11)$$

where $N_{ij}^{\text{th}}(\text{std})$ is the theoretical rate for i - j^{th} bin, calculated with the standard values of the inputs and npull is the number of sources of uncertainty, which in our case is 5. The values of the systematic uncertainties are shown in Table 4.1

Uncertainties	Values
Flux Normalization	20%
Tilt Factor	5%
Zenith angle dependence	5%
Overall cross section	10%
Overall systematic	5%

Table 4.1: Systematic uncertainties used in the χ^2 analysis

The ξ_k 's are called the pull variables and they determine the number of σ 's by which the k^{th} input deviates from its standard value. In eqn 4.11, c_{ij}^k is the change in N_{ij}^{th} when the k^{th} input is changed by σ_k . The uncertainties in the inputs are not very large. Therefore, in eqn 4.11 we only considered the changes in N_{ij}^{th} which are linear in ξ_k . Thus we have a modified χ^2 defined by

$$\chi^2(\xi_k) = \sum_{i,j} \frac{\left[N_{ij}^{\text{th}}(\text{std}) + \sum_{k=1}^{\text{npull}} c_{ij}^k \xi_k - N_{ij}^{\text{ex}} \right]^2}{N_{ij}^{\text{ex}}} + \sum_{k=1}^{\text{npull}} \xi_k^2 \quad (4.12)$$

where the additional term ξ_k^2 is the penalty imposed for moving k^{th} input away from its standard value by $\sigma_k \xi_k$. The χ^2 with pulls, which includes the effects of all theoretical and systematic uncertainties, is obtained by minimizing $\chi^2(\xi_k)$, given in eqn 4.12, with respect to all the pulls ξ_k :

$$\chi_{\text{pull}}^2 = \text{Min}_{\xi_k} \left[\chi^2(\xi_k) \right] \quad (4.13)$$

4.3 Results

In this section we present the results of our analysis for T2K, NO ν A and ICAL experiment. We also give results for octant sensitivity when the results from both type of experiments are combined. In Refs. [103, 104], it has been shown that the atmospheric parameters Δm_{atm}^2 and $\theta_{\mu\mu}$ measured in MINOS are related to the oscillation parameters in nature, Δm_{31}^2 and θ_{23} using the following non-trivial transformations:

$$\sin \theta_{23} = \frac{\sin \theta_{\mu\mu}}{\cos \theta_{13}} , \quad (4.14)$$

$$\Delta m_{31}^2 = \Delta m_{atm}^2 + (\cos^2 \theta_{12} - \cos \delta \sin \theta_{13} \sin 2\theta_{12} \tan \theta_{23}) \Delta m_{21}^2 . \quad (4.15)$$

These transformations become significant in light of the moderately large measured value of θ_{13} . Therefore, in order to avoid getting an erroneous estimate of octant sensitivity, we take these ‘corrected’ definitions into account.

The true value of the oscillation parameters used for this analysis are:

$$\begin{aligned} (\Delta m_{21}^2)^{tr} &= 7.6 \times 10^{-5} \text{ eV}^2 \\ (\sin^2 \theta_{12})^{tr} &= 0.31 \\ (\sin^2 2\theta_{13})^{tr} &= 0.1 \\ (\Delta m_{atm}^2)^{tr} &= 2.4 \times 10^{-3} \text{ eV}^2 , \end{aligned} \quad (4.16)$$

and specific values of $\theta_{\mu\mu}^{tr}$ and δ_{CP}^{tr} . In the theoretical predictions which are fitted to the simulated experimental data, the ‘test’ parameters are marginalized over the following ranges:

$$\begin{aligned} \delta_{CP} &\in [0, 2\pi) \\ \theta_{\mu\mu} &\in \begin{cases} (35^\circ, 45^\circ) & \text{(true higher octant)} \\ (45^\circ, 55^\circ) & \text{(true lower octant)} \end{cases} \\ \sin^2 2\theta_{13} &\in (0.07, 0.13) . \end{aligned} \quad (4.17)$$

Δm_{21}^2 and $\sin^2 \theta_{12}$ are fixed to their true values since their effect is negligible. Also, after verifying that the effect of a marginalization over Δm_{31}^2 is minimal, we have fixed Δm_{atm}^2 to its true value for computational convenience. In our calculation, the hierarchy is assumed to be known in all the atmospheric neutrino experiments, since the time-scale involved would ensure that the hierarchy is determined before any significant octant sensitivity is achievable.

Priors are taken in terms of the measured quantities $\sin^2 2\theta_{13}$ and $\sin^2 2\theta_{\mu\mu}$ as follows:

$$\chi_{prior}^2 = \left(\frac{\sin^2 2\theta_{\mu\mu}^{\text{true}} - \sin^2 2\theta_{\mu\mu}}{\sigma(\sin^2 2\theta_{\mu\mu})} \right)^2 + \left(\frac{\sin^2 2\theta_{13}^{\text{true}} - \sin^2 2\theta_{13}}{\sigma(\sin^2 2\theta_{13})} \right)^2 \quad (4.18)$$

with the 1σ error ranges as $\sigma_{\sin^2 2\theta_{\mu\mu}} = 5\%$ and $\sigma_{\sin^2 2\theta_{13}} = 0.01$ unless otherwise stated. The latter is the error on θ_{13} quoted recently by Double Chooz, Daya Bay and RENO.

4.3.1 Octant sensitivity at ICAL

In this analysis for ICAL detector we have considered 500 kt-yr fiducial volume. The magnetized detector will be able to identify the charge of the muon events. We have done the analysis when simulation results of muon energy and angle resolution have not been done. We have used the following neutrino energy and angular resolution for ICAL $\sigma_{E_\nu} = 0.1\sqrt{E_\nu}$, $\sigma_{\theta_\nu} = 10^\circ$.

The χ^2 is defined as,

$$(\chi_{\text{tot}}^2)^{\text{prior}} = \min(\chi_{\text{Atm}}^2 + \chi_{\text{prior}}^2), \quad (4.19)$$

where,

$$\text{where } \chi_{\text{Atm}}^2 = \chi_\mu^2 + \chi_{\bar{\mu}}^2 \quad (4.20)$$

For the atmospheric analysis, the flux and detector systematic uncertainties are included using the method of χ^2 pulls as outlined in [101, 105–107].

Magnetization of the ICAL detector gives an excellent sensitivity to hierarchy, hence it is plausible to assume that hierarchy would be determined before octant in these detectors. Thus in our analysis of atmospheric neutrinos, we assume the neutrino mass hierarchy fixed to be either normal or inverted, and do not marginalize over the hierarchy. This is tantamount to the assumption that the wrong-octant-wrong hierarchy solutions are excluded.

In Fig 4.5, we present the octant sensitivity of the ICAL detector with an exposure of 500 kt-yr. The second column of Table 4.2 displays the χ^2 values for different values of θ_{23} in the LO. The χ^2 in this case is symmetric about $\pi/4$, and therefore the values in the higher octant are similar. Assuming an inverted hierarchy gives worse results because in this case, matter resonance and hence octant sensitivity occurs in the antineutrino component of the event spectrum, for which the flux and detection cross-sections are lower. A 2σ sensitivity is obtained at $\theta_{23} = 39^\circ$ if NH is the true hierarchy.

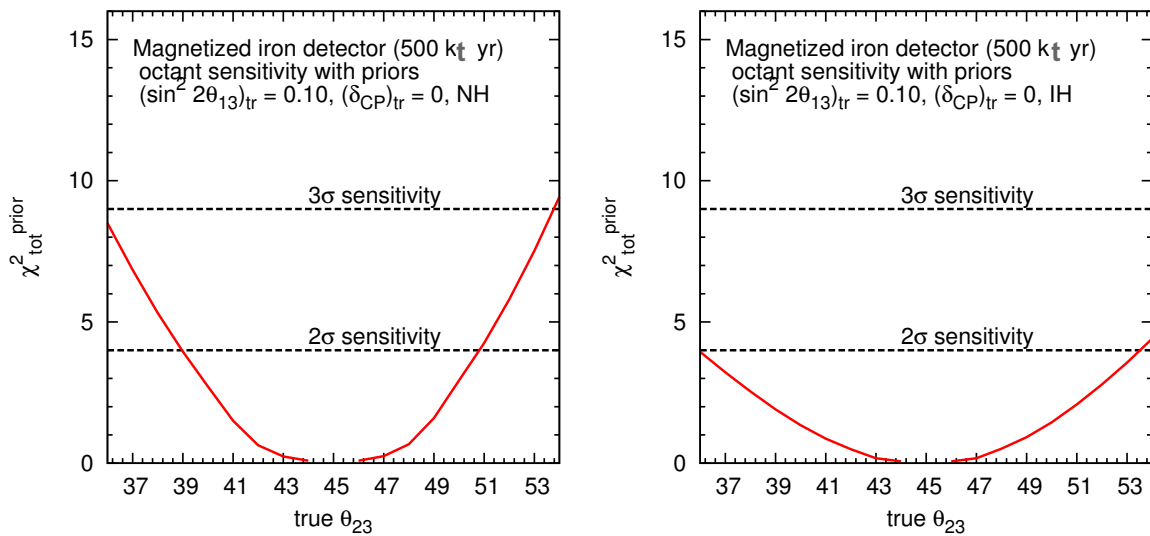


Figure 4.5: Marginalized octant sensitivity from muon events with the ICAL detector (500 kt yr exposure), for the case of normal and inverted mass hierarchy. In this figure priors have been added.

4.3.2 Octant sensitivity at NO ν A and T2K

We simulate the current generation of long baseline experiments NO ν A and T2K, using the GLoBES package [108,109] and its associated data files [110,111]. For T2K, we assume a 3 year run with neutrinos alone, running with beam power of 0.77 MW throughout. (We choose this low running time for T2K to compensate for the fact that their beam power will be increased to its proposed value over a period of a few years [112].) The energy resolutions and backgrounds are taken from Refs. [113–117]. The detector mass is taken to be 22.5 kt. For NO ν A, we consider the set-up as described in Refs. [118,119], which is

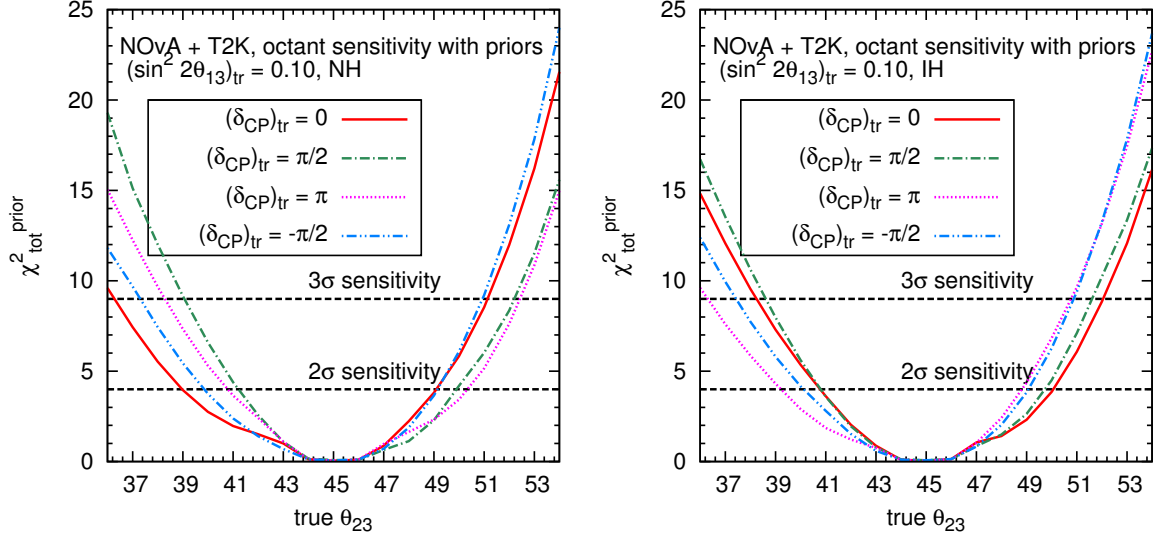


Figure 4.6: Marginalized octant sensitivity from a combination of NO ν A and T2K, for the case of normal and inverted mass hierarchy. The test hierarchy has been fixed to be the same as the true hierarchy in this case. In this figure priors have been added.

re-optimized for the moderately large measured value of θ_{13} . The 14 kt detector receives a neutrino and antineutrino beam for 3 years each, from the NuMI beam.

Fig 4.6 shows the octant sensitivity from a combination of NO ν A and T2K marginalized over the test parameters and with added priors. The χ^2 is defined as

$$(\chi^2_{\text{tot}})^{\text{prior}} = \min(\chi^2_{\text{NO}\nu\text{A}} + \chi^2_{\text{T2K}} + \chi^2_{\text{prior}}) \quad (4.21)$$

Here (and elsewhere), ‘min’ denotes a marginalization over the test parameters as outlined above. In Fig 4.6, the neutrino mass hierarchy is assumed to be known in each case. These plots are done for four specific true values of the CP phase, $\delta_{\text{CP}} = 0, \pi/2, \pi$ and $-\pi/2$.

4.3.3 Combined octant sensitivity

Fig 4.7 shows the combined octant sensitivity using the atmospheric muon neutrino signal in a magnetized iron detector with NO ν A and T2K. In Table 4.2 we list the marginalized octant sensitivity with priors for a magnetized iron detector (500 kt yr exposure), and

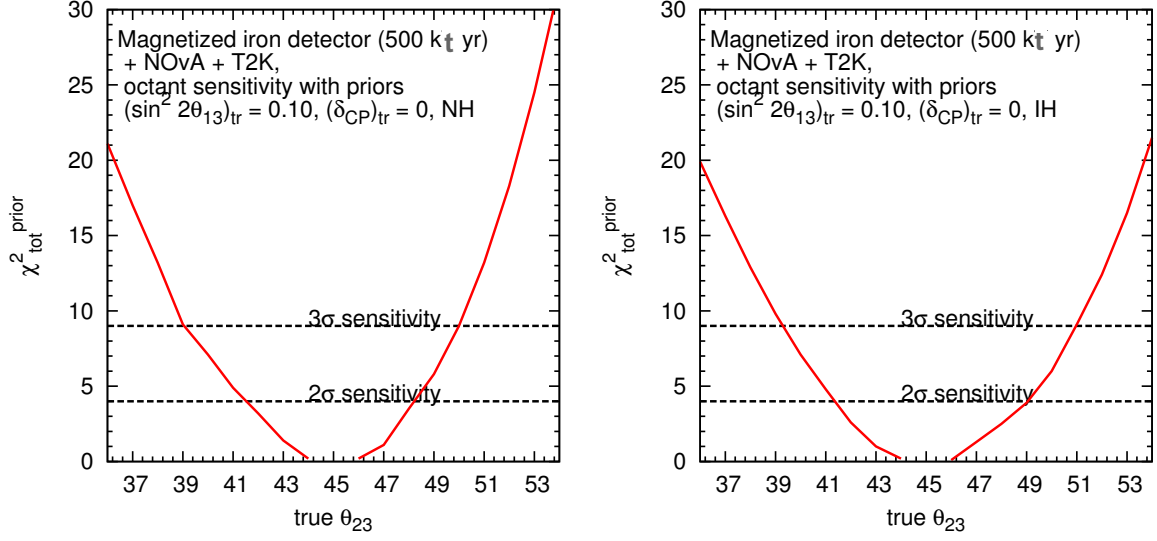


Figure 4.7: Marginalized octant sensitivity from a combination of the atmospheric muon neutrino signal at the ICAL detector (500 kt yr) + NO ν A + T2K, for the case of normal and inverted mass hierarchy. In this figure priors have been added.

θ_{23}^{tr}	ICAL(500 kt-yr)	ICAL(500 kt-yr) +NO ν A+T2K
36	8.5 (3.9)	21.1 (19.9)
37	6.8 (3.2)	17.0 (16.3)
38	5.3 (2.5)	13.2 (12.9)
39	3.9 (1.9)	9.1 (9.8)
40	2.7 (1.3)	7.1 (7.1)
41	1.5 (0.9)	4.9 (4.8)
42	0.6 (0.5)	3.2 (2.6)
43	0.2 (0.2)	1.4 (1.0)
44	0.1 (0.1)	0.2 (0.2)

Table 4.2: Marginalized octant sensitivity with ICAL detector (500 kt yr exposure), and a combination of either of them with NO ν A + T2K, for the case of normal (inverted) mass hierarchy, with $\sin^2 2\theta_{13}^{tr} = 0.1$ and $\delta_{CP}^{tr} = 0$. Priors have been included in this table.

a combination of each of them with NO ν A + T2K, for the case of both NH and IH. All of the above results are for $\delta_{CP}^{tr} = 0$. For a magnetized iron detector, the combination with NO ν A + T2K gives a 3σ sensitivity at $\theta_{23} = 39^\circ$ for NH.

In conclusion, we find that the improved precision of θ_{13} and the different dependence

on θ_{23} in the disappearance and appearance channels probabilities leads to an enhanced octant sensitivity. The ICAL detector can give a 2σ octant sensitivity for 500 kt yr exposure for $\theta_{23} = 39^\circ$, $\delta_{CP} = 0$ and normal hierarchy, this increases to 3σ for both hierarchies by combining with T2K and $\text{NO}\nu\text{A}$.

Chapter 5

Probing Lorentz and CPT Violation at ICAL

Invariance under the product of charge conjugation (C), parity (P) and time reversal (T), *i.e.* the CPT theorem [120–122], is a linchpin of present-day quantum field theories underlying particle physics. It is noteworthy that this invariance under the product of purely discrete symmetries is actually a consequence of the invariance of the Lagrangian (\mathcal{L}) under a connected continuous group, namely, proper Lorentz transformations. Additionally, it follows from the requirement that \mathcal{L} be hermitian and the interactions in the underlying field theory be local, with the fields obeying the commutation relations dictated by the spin-statistics theorem.

Theories attempting to unify gravity and quantum mechanics may, however, break such seemingly solid pillars of low energy effective field theories (like the Standard Model (SM)) via new physics associated with the Planck scale. For a general mechanism for the breaking of Lorentz symmetry in string theories, see, for instance, [123]. Other scenarios for such breaking have been discussed in [124] and [125]. Also, as shown in [32], a violation of CPT always breaks Lorentz invariance, while the converse is not true. A framework for incorporating CPT and Lorentz violation into a general relativistically extended version of the SM has been formulated in [34, 126]. It is termed as the Standard Model Extension (SME), and our discussion in this paper will utilize the effective CPT violating (CPTV) terms that it introduces. Such terms, given the impressive agreement of the (CPT and Lorentz invariant) SM with all present day experiments, must of necessity

be small.

A characteristic attribute of neutrino oscillations is the amplification, via interference, of the effects of certain small parameters (*e.g.* neutrino masses) in the underlying SM Lagrangian. As discussed in [35] and [127], the CPT violation manifest in an effective SME Hamiltonian can also be rendered measurable in neutrino oscillation experiments. Its non-observation, on the other hand, can be used to set impressive limits on CPT and Lorentz violation. This has been done, to cite a few recent examples, by IceCube [128], Double Chooz [129, 130], LSND [131], MiniBooNE [132], MINOS [133, 134] and Super Kamiokande [135].

In what follows, in Section 5.1, we review the perturbative phenomenological approach that allows us to introduce the effects of CPT violation in the neutrino oscillation probability, based on the SME. We examine effects at the probability level, in order to get a better understanding of the physics that drives the bounds we obtain using our event rate calculations. In section 5.2, we describe our method of analysis, and in section 5.3, we discuss our results in the form the bounds on CPT violating terms.

5.1 CPTV effects at the probability level

5.1.1 Formalism

The effective Lagrangian for a single fermion field, with Lorentz violation [33] induced by new physics at higher energies can be written as

$$\mathcal{L} = i\bar{\psi}\partial_{\mu}\gamma^{\mu}\psi - m\bar{\psi}\psi - A_{\mu}\bar{\psi}\gamma^{\mu}\psi - B_{\mu}\bar{\psi}\gamma_{5}\gamma^{\mu}\psi , \quad (5.1)$$

where A_{μ} and B_{μ} are real numbers, hence A_{μ} and B_{μ} necessarily induce Lorentz violation, being invariant under boosts and rotations, for instance. Such violation under the group of proper Lorentz transformations then leads to CPT violation [32]. CPT violation may also occur if particle and anti-particle masses are different. Such violation, however, also breaks the locality assumption of quantum field theories [32]. We do not consider this mode of CPT breaking in our work.

The effective contribution to the neutrino Lagrangian can then be parametrized [43] as

$$\mathcal{L}_\nu^{CPTV} = \bar{\nu}_L^\alpha b_\mu^{\alpha\beta} \gamma^\mu \nu_L^\beta \quad (5.2)$$

where $b_\mu^{\alpha\beta}$ are four Hermitian 3×3 matrices corresponding to the four Dirac indices μ and α, β are flavour indices. In the literature the CPT and Lorentz violating term $b_\mu^{\alpha\beta}$ is also frequently denoted as $(a)_\mu^{\alpha\beta}$ which combines the vector and axial couplings in equation 5.1. See, for example, [127]. Therefore the effective Hamiltonian in the vacuum for ultra-relativistic neutrinos with definite momentum p is

$$H \equiv \frac{MM^\dagger}{2p} + b_0 \quad (5.3)$$

where M is the neutrino mass matrix in the CPT conserving limit. As mentioned above, the b_μ parametrize the extent of CPT violation.

In going to equation 5.3 from equation 5.2 above, we have made an implicit transition to a preferred frame in which the cosmic microwave background is isotropic. We note that this will result in small anisotropic correction terms in the laboratory frame. We can also obtain the same effective Hamiltonian using modified dispersion relation. We generally write the Lorentz Invariance(LI) dispersion relation as $E^2 = m^2 + p^2$. But to violate LI, we use the modified dispersion relation $E^2 = F(p,m)$. We note that our world is almost LI, and at rest with respect to the CMB, hence any modified dispersion relation must reduce to the LI dispersion at lower energies. The dispersion relation using rotational invariance in CMB frame can be written as [136]

$$E^2 = m^2 + p^2 + E_{pl} f^{(1)} |p| + f^{(2)} p^2 + \dots \quad (5.4)$$

where f^n ,s are dimensionless and E_{pl} is the Planck energy at which the LI is expected to be broken in quantum gravity.

Thus the effective Hamiltonian in the vacuum for ultra-relativistic neutrinos with definite momentum p is

$$H \equiv \frac{MM^\dagger}{2p} + b \quad (5.5)$$

where $b = \frac{E_{pl} f^{(1)}}{2}$ is the leading term which contributes to the CPT violation.

In many experimental situations, the neutrino passes through appreciable amounts of matter, including this effect, the Hamiltonian with CPT violation in the flavour basis becomes

$$H_f = \frac{1}{2E} \cdot U_0 \cdot D(0, \Delta m_{21}^2, \Delta m_{31}^2) \cdot U_0^\dagger + U_b \cdot D_b(0, \delta b_{21}, \delta b_{31}) \cdot U_b^\dagger + D_m(V_e, 0, 0) \quad (5.6)$$

where U_0 & U_b are unitary matrices and $V_e = \sqrt{2}G_F N_e$, where G_F is the fermi coupling constant and N_e is the electron number density. Value of $V_e = 0.76 \times 10^{-4} \times Y_e [\frac{\rho}{g/cc}]$ eV, where Y_e is the fraction of electron, which is ≈ 0.5 for earth matter and ρ is matter density inside earth. D , D_m and D_b are diagonal matrices with their elements as listed. Here $\delta b_{i1} \equiv b_i - b_1$ for $i = 2, 3$, where b_1, b_2 and b_3 are the eigenvalues of b .

As is well-known, in standard neutrino oscillations, U_0 is parametrized by three mixing angles ($\theta_{12}, \theta_{23}, \theta_{13}$) and one phase δ_{CP} . In general for an N dimensional unitary matrix, there are N independent rotation angles (i.e. real numbers) and $N(N + 1)/2$ imaginary quantities (phases) which define it. For Dirac fields, $(2N - 1)$ of these may be absorbed into the representative spinor, while for Majorana fields this can be done for N phases. In the latter case, the $N - 1$ additional phases in U_0 become irrelevant when the product MM^\dagger is taken.

It is clear that the results will depend on the mixing angles and phases in the CPT violation sector. In general U_b has 3 mixing angles and 3 phases, but for simplicity and to understand the effect of the mixing angle in the CPT sector, we have assumed phases of U_b to be zero. In what follows, we examine the effects of three different representative sets of mixing angles, 1) small mixing ($\theta_{b12} = 6^\circ, \theta_{b23} = 9^\circ, \theta_{b13} = 3^\circ$), 2) large mixing ($\theta_{b12} = 38^\circ, \theta_{b23} = 45^\circ, \theta_{b13} = 30^\circ$) and the third set 3) uses the same values as the mixing in neutrino PMNS, ($\theta_{b12} = \theta_{12}, \theta_{b23} = \theta_{23}, \theta_{b13} = \theta_{13}$). We use the recent best fit neutrino oscillation parameters in our calculation as mentioned in Table 5.1.

Before going into the detailed numerical calculations, we can roughly estimate the bound on CPTV term. As an example, let us assume case 3) *i.e* when $U_b = U_0$, then δb can effectively be added to $\frac{\Delta m^2}{2E}$. If we take 10 GeV for a typical neutrino energy, the value of $\frac{\Delta m^2}{2E}$ will be about 10^{-22} GeV. Assuming the CPT violating term to be of the same order, and assuming that neutrino mass splitting can be measured at ICAL to 10% accuracy, we expect sensitivity to δb values of approximately around 10^{-23} GeV.

From case 3 above, we note further that in its probability expressions, δb_{21} will always

appear with the smaller (by a factor of 30) mass squared difference Δm_{21}^2 . Thus we expect its effects on oscillations will be sub-dominant in general, limiting the capability of atmospheric neutrinos to constrain it, and in our work we have not been able to put useful constraints on δb_{21} . Although, for completeness, in our analysis δb_{21} is marginalized over the range 0 to 5×10^{-23} GeV. Thus, our effort has been to find a method which will give the most stringent bounds on CPT violation as parametrized by δb_{31} . For simplicity, all phases are set to zero, hence the distinction between Dirac and Majorana neutrinos with regard to the number of non-trivial phases does not play a role in what follows. We note here that phases are contained in the imaginary part of the CPT violating matrix in the flavour basis, and hence setting them to zero allows an emphasis on CPT as opposed to the pure CP effects. Moreover, in the approximation where the effects of δb_{21} are much smaller than those of δb_{31} , the impact of at least some of the non-trivial phases anyway will be negligible. We also study the effect and impact of hierarchy in putting constraints on CPT violating terms.

5.1.2 Effect at the level of probability

Prior to discussing the results of our numerical simulations, it is useful to examine these effects at the level of probabilities. We note that the matter target in our case is CP asymmetric, which will automatically lead to effects similar to those induced by U_b . In order to separate effects arising due to dynamical CPT violation from those originating due to the CP asymmetry of the earth, it helps to consider the difference in the disappearance probabilities with U_b effects turned on and off, respectively. We use the difference in probabilities

$$\Delta P = P_{\nu_\mu\nu_\mu}^{U_b \neq 0} - P_{\nu_\mu\nu_\mu}^{U_b = 0}. \quad (5.7)$$

We do this separately for ν_μ and $\bar{\nu}_\mu$ events with NH and IH assumed as the true hierarchy. The results are shown in the Fig 5.1 and 5.2. We note that at the event level, the total muon events receive contributions from both the $P_{\nu_\mu\nu_\mu}$ disappearance and $P_{\nu_e\nu_\mu}$ appearance channels, and the same is true for anti-neutrinos. In our final numerical results, we have taken both these contributions into account.

Several general features are apparent in Fig 5.1-5.2. First, effects are uniformly small at shorter baselines irrespective of the value of the energy. From the 2 flavour analysis, *e.g.* [46] we recall that the survival probability difference in vacuum is proportional to

$\sin(\frac{\delta m^2 L}{2E}) \sin(\delta b L)$. The qualitative feature that CPT effects are larger at long baselines continues to be manifest even when one incorporates three flavour mixing and the presence of matter, and this is brought out in all the figures.

Secondly, as is well-known, matter effects are large and resonant for neutrinos and NH, and for anti-neutrinos with IH. Thus in both these cases, they mask the (smaller) effect of CPT stemming from U_b . Hence for neutrino events, CPT sensitivity is significantly higher if the hierarchy is inverted as opposed to normal, and the converse is true for anti-neutrino events.

Finally, effects are largest for cases 3) and 2), and smaller for case 1). The effect is smaller for case 1) is due to the fact that mixing is very small compared to other two. The origin of the difference for the case 2) and 3) is likely due to the fact that CPT violating effects are smaller when θ_{b13} is large, as shown in Fig 5.3.

We carry through this mode of looking at the difference between the case when U_b is non-zero and zero respectively to the event and χ^2 levels in our calculations below. To use the lepton charge identification capability of a magnetized iron calorimeter optimally, we calculate χ^2 from μ^- and μ^+ events separately. Following this procedure, the contribution arising through matter being CP asymmetric will expectedly cancel for each μ^- and μ^+ event for any given zenith angle and energy. The numerical procedure adopted and the details of our calculation are provided in the following section.

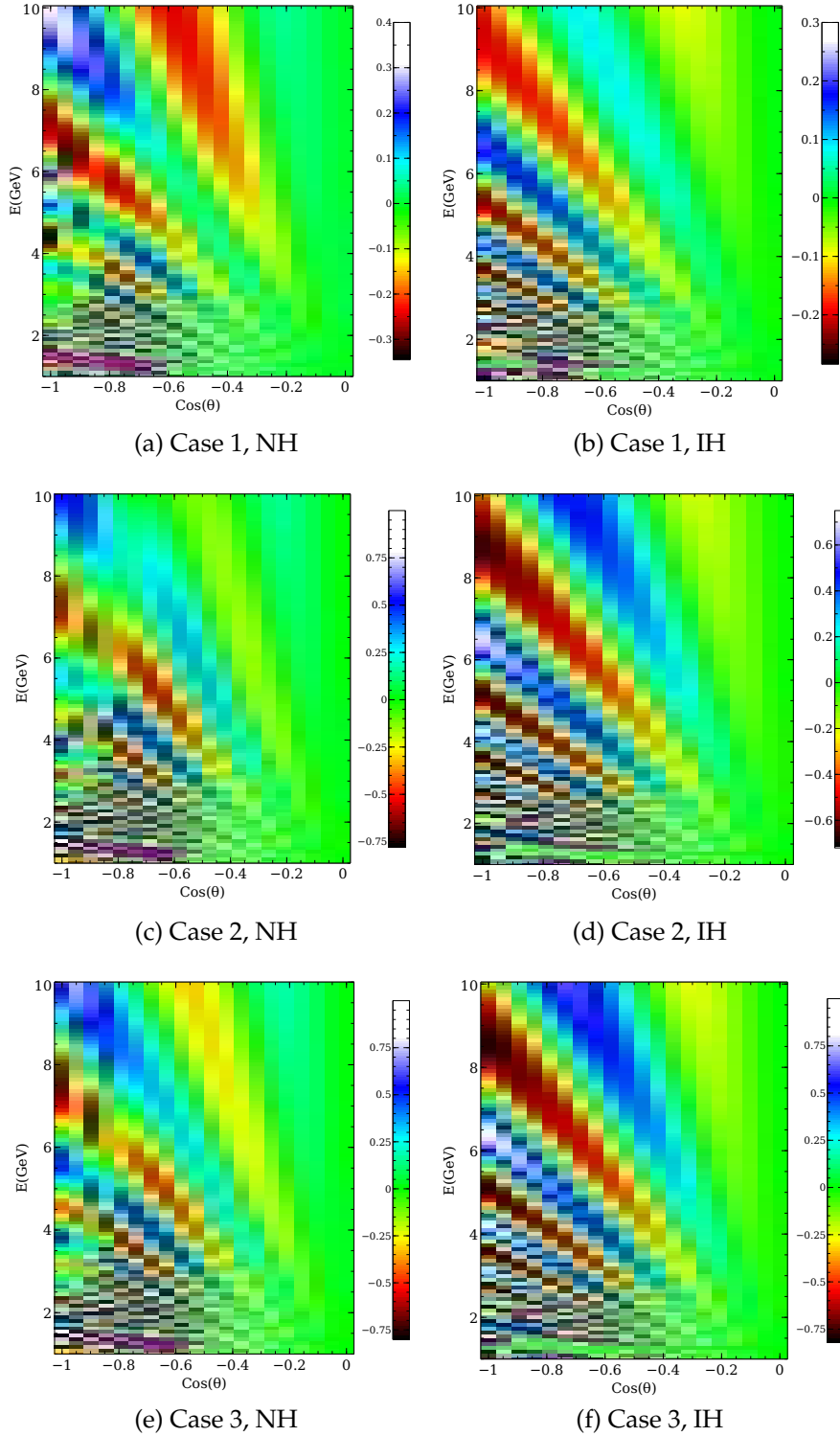


Figure 5.1: The oscillograms of $\Delta P = (P_{\nu_\mu \nu_\mu}^{U_b \neq 0} - P_{\nu_\mu \nu_\mu}^{U_b = 0})$ for 3 different mixing cases have been shown. The value of $\delta b_{31} = 3 \times 10^{-23} \text{ GeV}$ is taken for $U_b \neq 0$. Left and right panels are for Normal and Inverted hierarchy respectively.

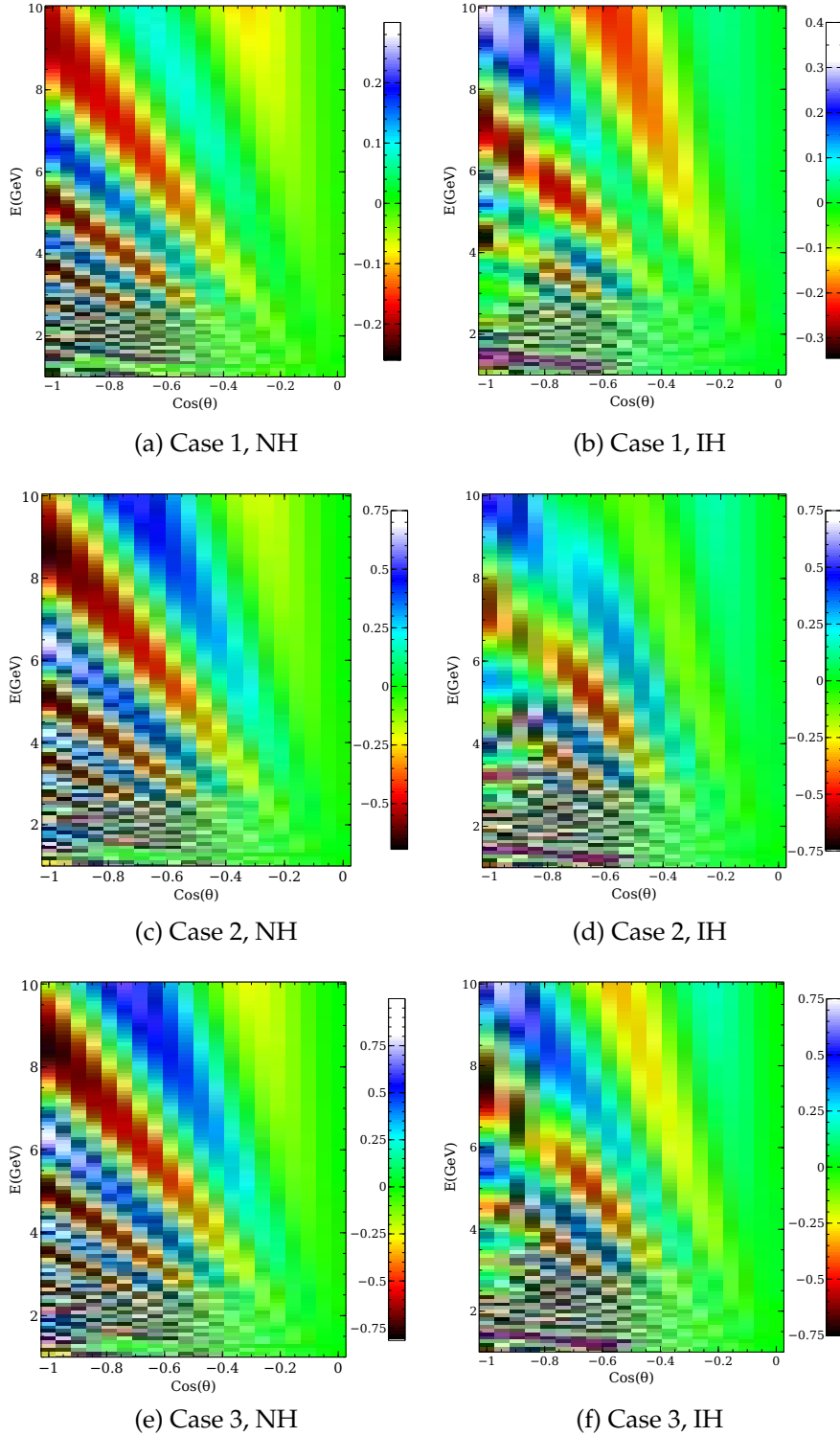


Figure 5.2: The oscillograms of $\Delta P = (P_{\bar{\nu}_\mu \bar{\nu}_\mu}^{U_b \neq 0} - P_{\bar{\nu}_\mu \bar{\nu}_\mu}^{U_b = 0})$ for 3 different mixing cases have been shown. The value of $\delta b_{31} = 3 \times 10^{-23} \text{ GeV}$ is taken for $U_b \neq 0$. Left and right panels are for Normal and Inverted hierarchy respectively.

5.2 Numerical procedure

Our work uses the ICAL detector as a reference configuration, but the qualitative content of the results will hold for any similar detector. Magnetized iron calorimeters typically have very good energy and direction resolution for reconstructing μ^+ and μ^- events. The analysis proceeds in two steps: (1) Event simulation (2) Statistical procedure and the χ^2 analysis.

5.2.1 Event simulation

We use the NUANCE [137] neutrino generator to generate events. The ICAL detector composition and geometry are incorporated within NUANCE and atmospheric neutrino fluxes(Honda et al. [102]) have been used. In order to reduce the Monte Carlo (MC) fluctuations in the number of events given by NUANCE, we generate a very large number of neutrino events with an exposure of $50 \text{ kt} \times 1000 \text{ years}$ and then finally normalize to 500 kt-yr .

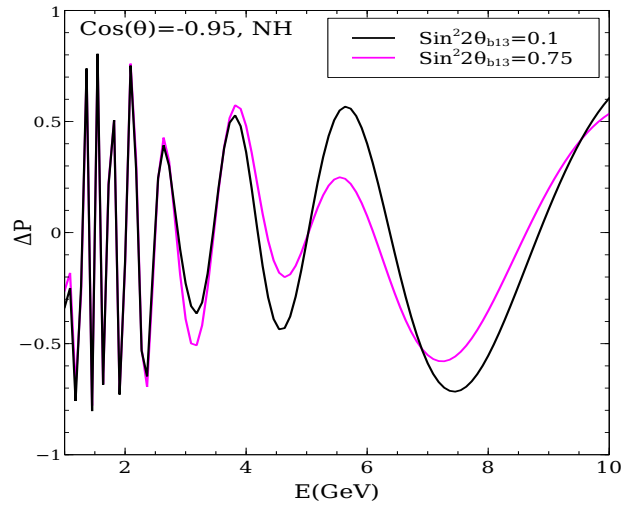


Figure 5.3: The difference of the $P_{\nu_\mu \nu_\mu}$ with and without CPTV for $\delta b_{31} = 3 \times 10^{-23} \text{ GeV}$ for two θ_{b13} values as a function of energy for a specific value of zenith angle. All other oscillation parameters are same.

Each changed-current neutrino event is characterized by neutrino energy and neutrino zenith angle, as well as by a muon energy and muon zenith angle. In order to save on

Oscillation parameter	true values	Oscillation parameter	true values
$\sin^2 2\theta_{12}$	0.86	δ_{CP}	0.0
$\sin^2 2\theta_{23}$	1.0	$\sin^2 2\theta_{b12}$	1) 0.043, 2) 0.94, 3) 0.86
$\sin^2 2\theta_{13}$	0.1	$\sin^2 2\theta_{b23}$	1) 0.095, 2) 1.0, 3) 1.0
Δm_{21}^2 (eV ²)	7.5×10^{-5}	$\sin^2 2\theta_{b13}$	1) 0.011, 2) 0.75, 3) 0.1
$ \Delta m_{32}^2 $ (eV ²)	2.4×10^{-3}	$\delta_b, \phi_{b2}, \phi_{b3}$	0.0, 0.0, 0.0

Table 5.1: True values of the oscillation parameters used in the analysis

computational time, we use a re-weighting algorithm to generate oscillated events. This algorithm, takes the neutrino energy and angle for each event and calculates probabilities $P_{\nu_\mu\nu_\mu}$ and $P_{\nu_\mu\nu_e}$ for any given set of oscillation parameters. It then compares it with a random number r between 0 to 1. If $r < P_{\nu_\mu\nu_e}$, then it is classified as a ν_e event. If $r > (P_{\nu_\mu\nu_e} + P_{\nu_\mu\nu_\mu})$, it classified as a ν_τ event. If $P_{\nu_\mu\nu_e} \leq r \leq (P_{\nu_\mu\nu_e} + P_{\nu_\mu\nu_\mu})$, then it is considered to come from an atmospheric ν_μ which has survived as a ν_μ . Similarly muon neutrinos from the oscillation of ν_e to ν_μ are also calculated using this re-weighting method.

Oscillated muon events are binned as a function of muon energy and muon zenith angle. We have divided each of the ten energy bins into 40 zenith angle bins. These binned data are folded with detector efficiencies and resolution functions as described in equation (6) to simulate reconstructed muon events. In this work we have used the (i) muon reconstruction efficiency (ii) muon charge identification efficiency (iii) muon energy resolution (iv) muon zenith angle resolution, obtained by the INO collaboration [138], separately for μ^+ and μ^- .

The measured muon events after implementing efficiencies and resolution are

$$N(\mu^-) = \int dE_\mu \int d\theta_\mu [R_{E_\mu} R_{\theta_\mu} (R_{eff} C_{eff} N_{osc}(\mu^-) + \bar{R}_{eff} (1 - \bar{C}_{eff}) N_{osc}(\mu^+))] \quad (5.8)$$

where $R_{eff}, C_{eff}, \bar{R}_{eff}, \bar{C}_{eff}$ are reconstruction and charge identification efficiencies for μ^- and μ^+ respectively, N_{osc} is the number of oscillated muons in each true muon energy and zenith angle bin and $R_{E_\mu}, R_{\theta_\mu}$ are energy and angular resolution functions.

The energy and angular resolution function in Gaussian form are given by

$$R_E = \frac{1}{\sqrt{2\pi}\sigma_E} \exp \left[-\frac{(E_m - E_t)^2}{2\sigma_E^2} \right] \quad (5.9)$$

$$R_\theta = N_\theta \exp \left[-\frac{(\theta_t - \theta_m)^2}{2(\sigma_\theta)^2} \right] \quad (5.10)$$

Here E_m , E_t and θ_m, θ_t are measured and true energy and angle respectively. N_θ is the normalization constant, σ_θ, σ_E are angular and energy smearing of muons. σ_θ, σ_E are obtained from ICAL simulations [138].

5.2.2 Statistical procedure and the χ^2 analysis

We have generated event rate data with the true values of oscillation parameters given in Table 5.1 and assuming no CPT violation, these are defined as N^{ex} . They are then fitted with another set of data, labelled as (N^{th}), where we have assumed CPT violation. The statistical significance of the difference between these two sets of data will provide constraints on the CPT violation parameters.

We define χ^2 for the data as

$$\chi_{pull}^2 = \min_{\xi_k} [2(N^{th'} - N^{ex} - N^{ex} \ln(\frac{N^{th'}}{N^{ex}})) + \sum_{k=1}^{npull} \xi_k^2] \quad (5.11)$$

where

$$N^{th'} = N^{th} + \sum_{k=1}^{npull} c^k \xi_k \quad (5.12)$$

$npull$ is the number of pull variable, in our analysis we have taken $npull=5$. ξ_k is the pull variable and c^k are the systematic uncertainties. We have used 5 systematic uncertainties in this analysis as mentioned in Table 4.1 as generally used in the other analysis of the collaboration. We have assumed a Poissonian distribution for χ^2 because for higher energy bins the number of atmospheric events will be small.

Since ICAL can discriminate charge of the particle, it is useful to calculate $\chi^2(\mu^-)$ and $\chi^2(\mu^+)$ separately for μ^- and μ^+ events and then added to get total χ^2 . We have marginalized the total χ^2 within a 3σ range of the best fit value. χ^2 has been marginalized over

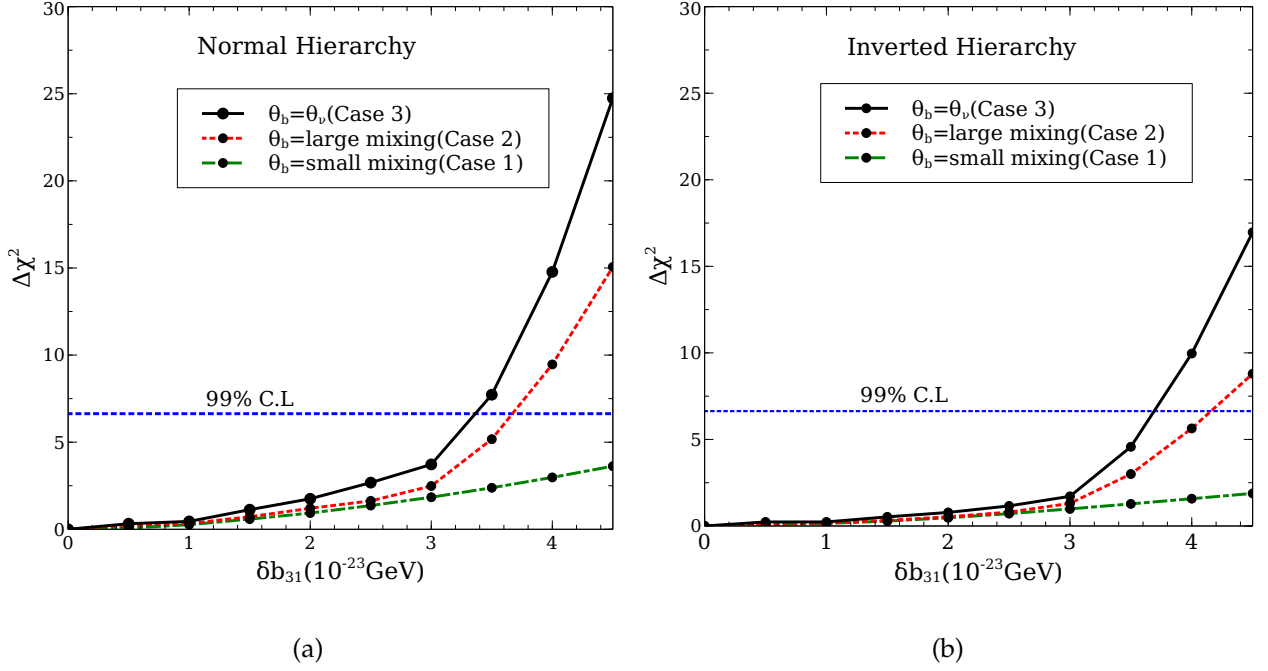


Figure 5.4: $\Delta\chi^2$ as a function of δb_{31} for different mixing of θ_b . Best fit oscillation parameters used as mentioned in Table 5.1. The results are marginalized over $\theta_{23}, \theta_{13}, \delta_{CP}, \Delta m_{31}^2$ and δb_{21} . Left and right panel are for Normal and Inverted hierarchy respectively.

the oscillation parameters $\Delta m_{31}^2, \theta_{23}, \theta_{13}, \delta_{CP}, \delta b_{21}$ for both normal and inverted hierarchy with μ^+ and μ^- separately for given set of input data.

5.3 Results

Figure(5.4) illustrates $\Delta\chi^2$ analysis performed by marginalizing over all the oscillation parameters $\Delta m_{31}^2, \theta_{23}, \theta_{13}$ within a 3σ range of their best fit values as given in Table 5.1. δ_{CP} is marginalized over 0 to 2π . δb_{21} is marginalized over the range 0 to 5×10^{-23} GeV. Left and right panel are for the Normal and Inverted Hierarchy respectively. While from figure(5.4) we see that the best bounds arise for case 3) for both the hierarchy, where mixing in the CPTV sector is the same as in the case of neutrino mixing, good bounds are also obtainable for large mixing. Since θ_{b12} and θ_{b23} in both cases 2) and 3) are large, the origin of this difference is likely due to the fact that CPT violating effects are smaller when θ_{b13} is large, as shown in fig 5.3.

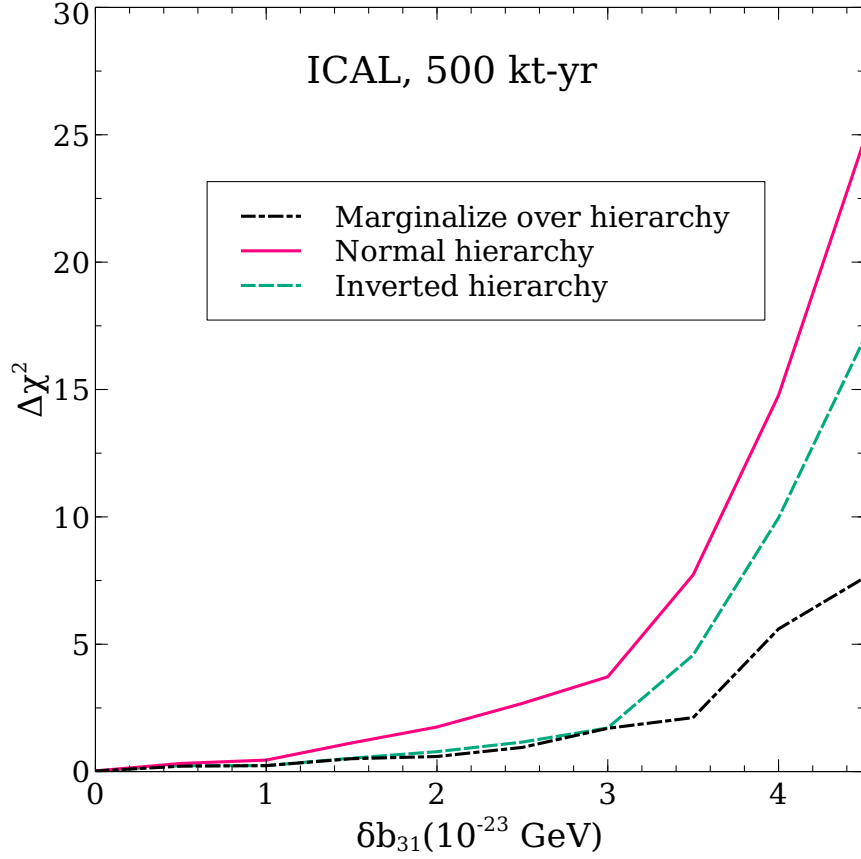


Figure 5.5: $\Delta\chi^2$ as a function of δb_{31} for case 3) is shown. The Red curve represents that both sets of data has Normal hierarchy as true hierarchy, and the green curve for Inverted hierarchy respectively. Black curve shows the bounds where hierarchy is marginalized over.

From figure(5.4) we see that 99% C.L. or better constraints on the CPT violating parameter, δb_{31} are possible for both hierarchies if it is $\gtrsim 4 \times 10^{-23}$ GeV, if the mixing in the CPTV sector is not small.

It is clear from the fig 5.5 that if marginalization over the hierarchy is carried out, the constraints are considerably weaker. Hence a knowledge of the hierarchy certainly helps in getting useful constraints on CPT. The sensitivities obtained are comparable to those anticipated from other types of experiments and estimates in the literature [44–47, 50].

Chapter 6

Non-Standard Interactions in neutrino propagation at ICAL

In this chapter, we have described the effect of Non-Standard neutrino Interaction(NSI) on neutrino oscillation pattern at atmospheric neutrinos with the help of ICAL detector. We use neutrino oscillograms as our main tool to understand the role of NSI parameters at the probability level. We have tried to find bounds on different NSI parameters using this detector. Some of the results presented in this chapter are published in [139].

The minimal theoretical scenario needed to describe oscillations requires the existence of neutrino masses. The simplest way is to add right handed neutrino fields to the SM particle content (something that the originators of the SM would, no doubt, have trivially done were non-zero neutrino masses known then) and generate a Dirac mass term for neutrinos. However it is hard to explain the smallness of the neutrino mass terms via this mechanism. Once we invoke new physics in order to explain the non-zero neutrino masses, it seems rather unnatural to exclude the possibility of non standard interactions (NSI) which can, in principle, allow for flavour changing interactions. Simultaneously, these are new sources of CP violation which can affect production, detection and propagation of neutrinos [140].

In recent years, the emphasis has shifted towards understanding the interplay between SI and NSI and whether future oscillation experiments can test such NSI apart from determining the standard oscillation parameters precisely. This has led to an upsurge in research activity in this area (see the references in [140]). There are also other motiva-

tions for NSI such as (electroweak) leptogenesis [141], neutrino magnetic moments [142], neutrino condensate as dark energy [143, 144].

Neutrino oscillation experiments can probe these NSI by exploiting the interference of standard amplitude with the NSI one. In view of the excellent agreement of data with standard flavour conversion via oscillations, we would like to explore how large an NSI is still viable or how sub-dominant effects show up in oscillation probabilities.

The plan of the chapter is as follows. We first briefly outline the NSI framework in Sec. 6.1 and then discuss the neutrino oscillation probabilities in presence of NSI using perturbation theory approach in Sec. 6.2. We describe the features of the neutrino oscillograms in Sec. 6.3. In section 6.4, we discuss about the effect of nsi parameters on octant of θ_{23} . Analysis procedure and event spectrum has been described in section 6.5 and finally results are shown in section 6.6.

6.1 Neutrino NSI Framework: relevant parameters and constraints

As in case of standard weak neutrino interactions, a wide class of "new physics scenarios" can be conveniently parametrised in a model independent way at low energies ($E \ll M_{EW}$) by using effective four-fermion interactions. In general, the NSI can impact the neutrino oscillation signals via two kinds of interactions : (a) charged current (CC) interactions (b) neutral current (NC) interactions. However, CC interactions affect processes only at the source or the detector and these are clearly discernible at near detectors (via the zero distance effect). On the other hand, the NC interactions affect the propagation of neutrinos (via baseline dependent effect) which can be studied at far detectors. Due to this decoupling, the two can be treated in isolation. Usually, it is assumed that the CC NSI terms (e.g., of the type $(\bar{\nu}_\beta \gamma^\mu P_L l_\alpha)(\bar{f}_L \gamma_\mu P_C f'_L)$ with f, f' being the components of a weak doublet) are more tightly constrained than the NC terms and, hence, are not considered. It turns out, though, that, in specific models, the two can be of comparable strengths [145]. However, we are interested in the NSI that alters the propagation of neutrinos, we shall consider the NC type of interactions alone.

The effective Lagrangian describing the NC type neutrino NSI of the type $(V - A)(V \pm A)$

$$\mathcal{L}_{NSI} = -2\sqrt{2}G_F \epsilon_{\alpha\beta}^{fC} [\bar{\nu}_\alpha \gamma^\mu P_L \nu_\beta][\bar{f} \gamma_\mu P_C f], \quad (6.1)$$

where G_F is the Fermi constant, ν_α, ν_β are neutrinos of different flavours, f is a first generation SM fermion (e, u, d). The chiral projection operators are given by $P_L = (1 - \gamma_5)/2$ and $P_C = (1 \pm \gamma_5)/2$. In general, the NSI terms can be complex. The new NC interaction terms can affect the neutrino oscillation physics either by causing the flavour of neutrino to change ($\nu_\alpha + f \rightarrow \nu_\beta + f$) *i.e.*, flavour changing (FC) interaction or, by having a non-universal scattering amplitude of NC for different neutrino flavours *i.e.*, flavour preserving (FP) interaction. At the level of the underlying Lagrangian, the NSI coupling of the neutrino can be to e, u, d . However, from a phenomenological point of view, only the sum (incoherent) of all these individual contributions (from different scatterers) contributes to the coherent forward scattering of neutrinos off matter. If we normalize to n_e , the effective NSI parameter for neutral Earth matter is

$$\epsilon_{\alpha\beta} = \sum_{f=e,u,d} \frac{n_f}{n_e} \epsilon_{\alpha\beta}^f = \epsilon_{\alpha\beta}^e + 2\epsilon_{\alpha\beta}^u + \epsilon_{\alpha\beta}^d + \frac{n_n}{n_e} (2\epsilon_{\alpha\beta}^d + \epsilon_{\alpha\beta}^u) = \epsilon_{\alpha\beta}^e + 3\epsilon_{\alpha\beta}^u + 3\epsilon_{\alpha\beta}^d \quad (6.2)$$

where n_f is the density of fermion f in medium crossed by the neutrino and n_n is the neutron number density. Also $\epsilon_{\alpha\beta}^f = \epsilon_{\alpha\beta}^{fL} + \epsilon_{\alpha\beta}^{fR}$ which implies that NC type NSI matter effects are sensitive to the vector sum of the NSI couplings.

Let us now discuss the constraints on NC type NSI parameters. As mentioned above, the contribution that enters oscillation framework is given by Eq.6.2. The individual NSI terms such as $\epsilon_{\alpha\beta}^{fL}$ or $\epsilon_{\alpha\beta}^{fR}$ are constrained in any experiment (keeping only one of them non-zero at a time) and moreover the coupling is either to e, u, d individually [70]. In view of this, it is not so straightforward to interpret those bounds in terms of effective $\epsilon_{\alpha\beta}$.

There are two ways : (a) One could take the most stringent constraint in the individual NSI terms (say, $|\epsilon_{\mu\tau}^u|$) and use that to bound the effective term (say, $|\epsilon_{\mu\tau}|$) in Eq 6.2 and that leads to

$$|\epsilon_{\alpha\beta}| < \begin{pmatrix} 0.06 & 0.05 & 0.27 \\ 0.05 & 0.003 & 0.05 \\ 0.27 & 0.05 & 0.16 \end{pmatrix} \quad (6.3)$$

b) With the assumption that the errors on individual NSI terms are uncorrelated, the

authors in Ref. [145] (see also Ref. [70]) deduce model-independent bounds on effective NC NSI terms for neutral Earth matter leads to

$$|\epsilon_{\alpha\beta}| < \begin{pmatrix} 4.2 & 0.33 & 3.0 \\ 0.33 & 0.068 & 0.33 \\ 3.0 & 0.33 & 21 \end{pmatrix} \quad (6.4)$$

Following the other studies on neutrino NSI during propagation, we will use a conservative value of $|\epsilon_{\alpha\beta}| = 0.15$ for the parameters $\epsilon_{\mu\tau}$, $\epsilon_{e\mu}$ and $\epsilon_{e\tau}$ appearing in the present work. NSI in the context of atmospheric neutrinos has been studied by various authors [71, 72, 146, 147]. The SK NSI search in atmospheric neutrinos crossing the Earth found no evidence in favour of NSI and the study led to upper bounds on NSI parameters [77] given by $|\epsilon_{\mu\tau}| < 1.1 \times 10^{-2}$, $|\epsilon'| = |\epsilon_{\mu\mu} - \epsilon_{\tau\tau}| < 4.9 \times 10^{-2}$. Although, SK collaboration uses a different normalization (n_d) while writing the effective NSI parameter (see Eq. (6.2)) and hence we need to multiply the bounds mentioned in Ref. [77] by a factor of 3. Also the off-diagonal NSI parameter is constrained $-0.20 < \epsilon_{\mu\tau} < 0.07$ from MINOS data using neutrino and antineutrino beams [75, 148]. In Ref. [149], the global analysis of oscillation data is used to extract allowed ranges of NSI parameters.

6.2 Neutrino oscillation probability in matter with NSI

In this chapter we have tried to write analytical expressions of the probability formula. The purpose of the analytic expressions presented here is to understand the features in the probability in presence of NSI. All the plots presented in this chapter are obtained numerically by solving the full three flavour neutrino propagation equation through Earth using the PREM density profile of the Earth, and the latest values of the neutrino parameters as obtained from global fits (see Table 1.1).

In case of atmospheric neutrinos, one can safely neglect the smaller mass squared difference Δm_{21}^2 in comparison to Δm_{31}^2 since $\Delta m_{21}^2 L/4E \ll 1$ for a large range of values of L and E (especially above a GeV). This "one mass scale dominance" (OMSD) approximation allows for a relatively simple exact analytic computation of the probability (as a function of only three parameters θ_{23} , θ_{13} and Δm_{31}^2) for the case of constant density matter [98]. In

order to systematically take into account the effect of small parameters, the perturbation theory approach is used.

In the ultra-relativistic limit, the neutrino propagation is governed by a Schrödinger-type equation with an effective Hamiltonian

$$\mathcal{H} = \mathcal{H}_{\text{vac}} + \mathcal{H}_{\text{SI}} + \mathcal{H}_{\text{NSI}} \quad (6.5)$$

where \mathcal{H}_{vac} is the vacuum Hamiltonian and $\mathcal{H}_{\text{SI}}, \mathcal{H}_{\text{NSI}}$ are the effective Hamiltonian in presence of Standard Interactions (SI) and non-standard interactions (NSI) respectively.

$$\mathcal{H} = \frac{1}{2E} \left\{ \mathcal{U} \begin{pmatrix} 0 & & \\ & \Delta m_{21}^2 & \\ & & \Delta m_{31}^2 \end{pmatrix} \mathcal{U}^\dagger + A(x) \begin{pmatrix} 1 + \epsilon_{ee} & \epsilon_{e\mu} & \epsilon_{e\tau} \\ \epsilon_{e\mu}^* & \epsilon_{\mu\mu} & \epsilon_{\mu\tau} \\ \epsilon_{e\tau}^* & \epsilon_{\mu\tau}^* & \epsilon_{\tau\tau} \end{pmatrix} \right\} \quad (6.6)$$

where $A(x) = \sqrt{2}G_F n_e(x)$ is the standard CC potential due to the coherent forward scattering of neutrinos and n_e is the electron number density. If we define dimensionless ratios

$$\Delta \equiv \frac{\Delta m_{31}^2}{2E} \quad ; \quad r_\Delta \equiv \frac{\Delta m_{21}^2}{\Delta m_{31}^2} \quad ; \quad r_A \equiv \frac{A(x)}{\Delta m_{31}^2} \quad (6.7)$$

Then the oscillation probability for $\nu_e \rightarrow \nu_\mu$ can be obtained as

$$\begin{aligned} P_{e\mu}^{NSI} &\simeq 4s_{13}^2 s_{23}^2 \left[\frac{\sin^2(1-r_A)\Delta L/2}{(1-r_A)^2} \right] \\ &+ 8s_{13}s_{23}c_{23}(|\epsilon_{e\mu}|c_{23}c_\chi - |\epsilon_{e\tau}|s_{23}c_\omega)r_A \left[\frac{\sin r_A \Delta L/2}{r_A} \frac{\sin(1-r_A)\Delta L/2}{(1-r_A)} \cos \frac{\Delta L}{2} \right] \\ &+ 8s_{13}s_{23}c_{23}(|\epsilon_{e\mu}|c_{23}s_\chi - |\epsilon_{e\tau}|s_{23}s_\omega)r_A \left[\frac{\sin r_A \Delta L/2}{r_A} \frac{\sin(1-r_A)\Delta L/2}{(1-r_A)} \sin \frac{\Delta L}{2} \right] \\ &+ 8s_{13}s_{23}^2(|\epsilon_{e\mu}|s_{23}c_\chi + |\epsilon_{e\tau}|c_{23}c_\omega)r_A \left[\frac{\sin^2(1-r_A)\Delta L/2}{(1-r_A)^2} \right] \end{aligned} \quad (6.8)$$

where we have used $\tilde{s}_{13} \equiv \sin \tilde{\theta}_{13} = s_{13}/(1-r_A)$ to the leading order in s_{13} , and $\chi = \phi_{e\mu} + \delta$, $\omega = \phi_{e\tau} + \delta$ and $s_{ij} = \sin \theta_{ij}$, $c_{ij} = \cos \theta_{ij}$. Only the parameters $\epsilon_{e\mu}$ and $\epsilon_{e\tau}$ enter in the probability expression.

The probability for $\nu_\mu \rightarrow \nu_\mu$ channel is given by

$$\begin{aligned}
P_{\mu\mu}^{NSI} &\simeq 1 - s_{2\times 23}^2 \left[\sin^2 \frac{\Delta L}{2} \right] \\
&\quad - |\epsilon_{\mu\tau}| \cos \phi_{\mu\tau} s_{2\times 23} \left[s_{2\times 23}^2 (r_A \Delta L) \sin \Delta L + 4c_{2\times 23}^2 r_A \sin^2 \frac{\Delta L}{2} \right] \\
&\quad + (|\epsilon_{\mu\mu}| - |\epsilon_{\tau\tau}|) s_{2\times 23}^2 c_{2\times 23} \left[\frac{r_A \Delta L}{2} \sin \Delta L - 2r_A \sin^2 \frac{\Delta L}{2} \right] \quad (6.9)
\end{aligned}$$

where $s_{2\times 23} \equiv \sin 2\theta_{23}$ and $c_{2\times 23} \equiv \cos 2\theta_{23}$. This means that NSI elements in the $\mu-\tau$ sector are completely decoupled from the ν_e [150–152] and the survival probability depends on three parameters $\epsilon_{\mu\mu}, \epsilon_{\mu\tau}, \epsilon_{\tau\tau}$ leading order expression [152].

In order to quantify the impact of NSI, it is useful to define a difference

$$\Delta P_{\alpha\beta} = P_{\alpha\beta}^{SI} - P_{\alpha\beta}^{NSI} \quad (6.10)$$

where $P_{\alpha\beta}^{SI}$ is probability of transition assuming standard interactions (*i.e.* with $\epsilon_{\alpha\beta}$ being set to zero in Eqs. (6.8) and (6.9)) and $P_{\alpha\beta}^{NSI}$ is the transition probability in presence of the NSI parameters. For the different channels that are relevant to our study, the $\Delta P_{\alpha\beta}$ are given below :

$$\begin{aligned}
\Delta P_{e\mu} &\simeq -8s_{13}s_{23}c_{23}(|\epsilon_{e\mu}|c_{23}c_\chi - |\epsilon_{e\tau}|s_{23}c_\omega)r_A \left[\frac{\sin r_A \Delta L/2}{r_A} \frac{\sin(1-r_A)\Delta L/2}{(1-r_A)} \cos \frac{\Delta L}{2} \right] \\
&\quad -8s_{13}s_{23}c_{23}(|\epsilon_{e\mu}|c_{23}s_\chi - |\epsilon_{e\tau}|s_{23}s_\omega)r_A \left[\frac{\sin r_A \Delta L/2}{r_A} \frac{\sin(1-r_A)\Delta L/2}{(1-r_A)} \sin \frac{\Delta L}{2} \right] \\
&\quad -8s_{13}s_{23}^2(|\epsilon_{e\mu}|s_{23}c_\chi + |\epsilon_{e\tau}|c_{23}c_\omega)r_A \left[\frac{\sin^2(1-r_A)\Delta L/2}{(1-r_A)^2} \right]. \quad (6.11)
\end{aligned}$$

$$\begin{aligned}
\Delta P_{\mu\mu} &\simeq |\epsilon_{\mu\tau}| \cos \phi_{\mu\tau} s_{2\times 23} \left(s_{2\times 23}^2 (r_A \Delta L) \sin \Delta L + 4c_{2\times 23}^2 r_A \sin^2 \frac{\Delta L}{2} \right) \\
&\quad - (|\epsilon_{\mu\mu}| - |\epsilon_{\tau\tau}|) s_{2\times 23}^2 c_{2\times 23} \left[\frac{r_A \Delta L}{2} \sin \Delta L - 2r_A \sin^2 \frac{\Delta L}{2} \right]. \quad (6.12)
\end{aligned}$$

For the case of anti-neutrinos, $A \rightarrow -A$ which implies that $r_A \rightarrow -r_A$ while $\Delta \rightarrow \Delta, r_\Delta \rightarrow$

r_Δ . Similarly for IH, $\Delta m_{31}^2 \rightarrow -\Delta m_{31}^2$, which implies $\Delta \rightarrow -\Delta, r_\Delta \rightarrow -r_\Delta, r_A \rightarrow -r_A$ but $\Delta r_A \rightarrow \Delta r_A$. In the present work, for the sake of simplicity, NSI parameters are taken to be real ($\epsilon_{\alpha\beta} = \epsilon_{\alpha\beta}^*$) and also $\delta_{CP} = 0$.

6.3 Neutrino oscillograms in presence of NSI

For a given hierarchy (NH or IH) and best-fit values of the oscillation parameters (as given in Table 1.1), the oscillation probability depends on only two quantities : the neutrino energy E and the zenith angle of the direction of the neutrino ($\cos \theta$). $\cos \theta = -1$ and $\cos \theta = 0$ correspond to vertically upward and horizontal directions respectively. The oscillation pattern can then be fully described by contours of equal oscillation probabilities in the $E - \cos \theta$ plane. We use these neutrino oscillograms of Earth to discuss the effect of neutrino - matter interactions on the atmospheric neutrinos passing through the Earth.

Let us now address the impact of NSI on neutrinos and anti-neutrinos traversing the Earth. To best illustrate the features, we consider only one NSI parameter to be non-zero. In the leading order expression there are only two combinations of the three NSI parameters ($\epsilon_{\mu\tau}, \epsilon_{\mu\mu}, \epsilon_{\tau\tau}$) that appear. Let us discuss them in turn below :

(a) $\epsilon_{\mu\tau} \neq 0; \epsilon_{\mu\mu} = \epsilon_{\tau\tau} = 0$: In Fig. 6.1, we show the corresponding $P_{\mu\mu}^{NSI}$ for the case of NH (top row) and IH (bottom row) and two specific values of the NSI parameter $\epsilon_{\mu\tau}$ consistent with the current bounds. Note that the case of NH and $\epsilon_{\mu\tau} > 0$ is grossly similar to the case of IH and $\epsilon_{\mu\tau} < 0$ (and, similarly, NH and $\epsilon_{\mu\tau} < 0$ vs. IH and $\epsilon_{\mu\tau} > 0$).

From Eq. (6.9), we see that there are two terms proportional to $\epsilon_{\mu\tau}$, one where the oscillation argument is $\sin \Delta L$ and other one with $\sin^2 \Delta L/2$. Thus the first term can be positive or negative depending upon the value of the phase, while the second term is always positive. It is the interplay of these two terms that leads to the features in these plots. The mass hierarchy dependence comes from the first term since we have $r_A \Delta L \sin(\Delta L)$ which changes sign when we go from NH to IH. Near the vacuum dip $\Delta L = (2p + 1)\pi/2$, this term will be dominant. Due to this for NH and $\epsilon_{\mu\tau} > 0$, we see an oscillatory pattern which is a modification of the standard oscillation pattern. For IH and $\epsilon_{\mu\tau} > 0$, the term proportional to $|\epsilon_{\mu\tau}|$ will have a negative overall sign and this leads to a somewhat washout of the oscillation pattern.

The difference between SI and NSI contributions to the probability $\Delta P_{\mu\mu}$ is shown in

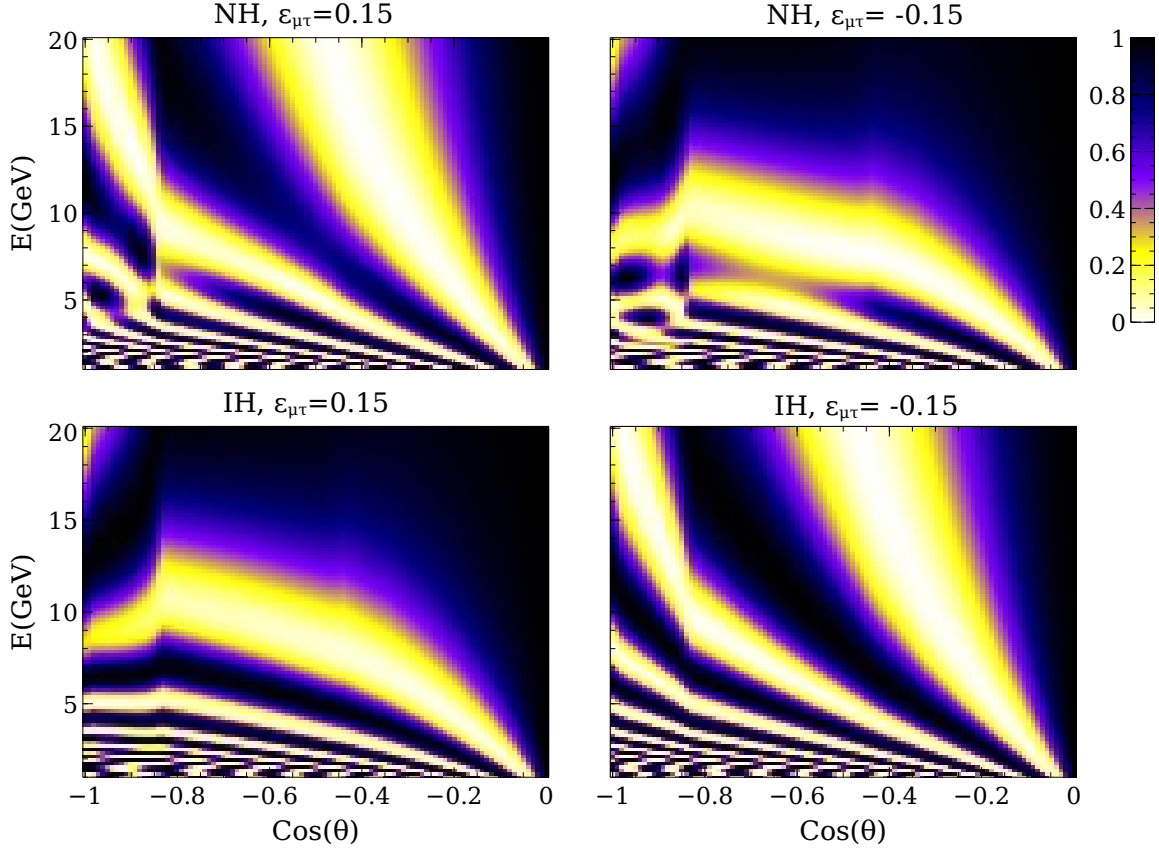


Figure 6.1: Oscillograms of $P_{\mu\mu}$ for NH and IH with non-zero $\epsilon_{\mu\tau}$.

Fig. 6.2. $|\Delta P_{\mu\mu}|$ can be as large as 1 for regions in the core and in mantle for some choice of $\epsilon_{\mu\tau}$ and hierarchy. We also note large changes in probability (the regions where the difference is large $\sim \pm 1$) along the diagonal line.

(b) $\epsilon_{\mu\mu} - \epsilon_{\tau\tau} \neq 0; \epsilon_{\mu\tau} = 0$: This case will correspond to diagonal FP NSI parameter, $\epsilon_{\mu\mu} - \epsilon_{\tau\tau}$. As mentioned above, the $\epsilon_{\mu\mu}$ is tightly constrained (see Eq. (6.4)) and the bound on $\epsilon_{\tau\tau}$ is very loose.

(c) Sub-dominant effects due to $\epsilon_{e\mu}, \epsilon_{e\tau} \neq 0$: Next we discuss how the $\epsilon_{e\mu}$ and $\epsilon_{e\tau}$ affect $\Delta P_{\mu\mu}$. For the case of NH, we compare the cases of non-zero $\epsilon_{\mu\tau}, \epsilon_{e\mu}, \epsilon_{e\tau}$ in Fig. 6.3. From Eq. (6.4), we see that the bounds for $\epsilon_{e\mu}$ and $\epsilon_{\mu\tau}$ are similar 0.33 while that of $\epsilon_{e\tau}$ is rather loose (3.0). It is seen that the other parameters involving the electron sector play only a sub-dominant role in this channel. This can also be understood from the fact that these terms do not appear in the first order expression of $P_{\mu\mu}^{NSI}$ (see Eq. (6.9)) but only appear at second order [150].

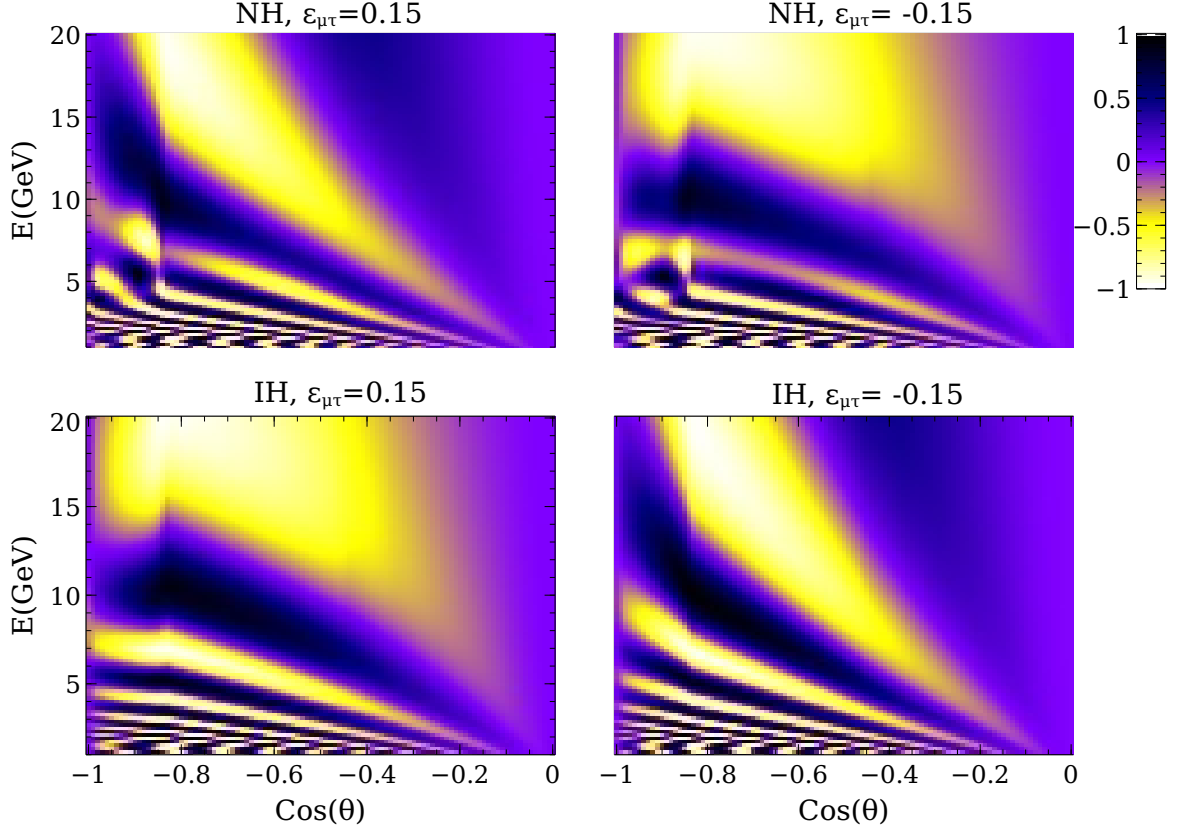


Figure 6.2: Oscillograms of $\Delta P_{\mu\mu}$ with non-zero $\epsilon_{\mu\tau}$.

$\nu_e \rightarrow \nu_\mu$ appearance channel :

In Fig. 6.4, we show the effect of $\epsilon_{\mu\tau}$ on the oscillograms of $\Delta P_{e\mu}$. Since the parameter $\epsilon_{\mu\tau}$ does not appear in the first order expression (Eq. (6.8)), naturally its impact is expected to be small. $|\Delta P_{e\mu}| \simeq 0.3 - 0.4$ only in very tiny regions. We compare the effects due to the three NSI parameters on this channel in Fig. 6.5. Since the parameters $\epsilon_{e\mu}, \epsilon_{e\tau}$ appear in the first order expression (Eq. (6.8)), naturally its impact is expected to be some what more as compared to $\epsilon_{\mu\tau}$.

(a) Subdominant effects due to $\epsilon_{\mu\tau} \neq 0$: In Fig. 6.4, we show the effect of $\epsilon_{\mu\tau}$ on the oscillograms of $\Delta P_{e\mu}$. Since the parameter $\epsilon_{\mu\tau}$ does not appear at all in the first order expression (Eq. (6.8)), naturally its impact is expected to be small. Consequently, $|\Delta P_{e\mu}| \neq 0$ only in very tiny regions and can at best be as large as $0.3 - 0.4$.

(b) Comparison of effects due to $\epsilon_{e\mu} \neq 0, \epsilon_{e\tau} \neq 0$ and $\epsilon_{\mu\tau} \neq 0$: In Fig. 6.5, we compare the effects due to the three NSI parameters for the case of NH, allowing only one of them

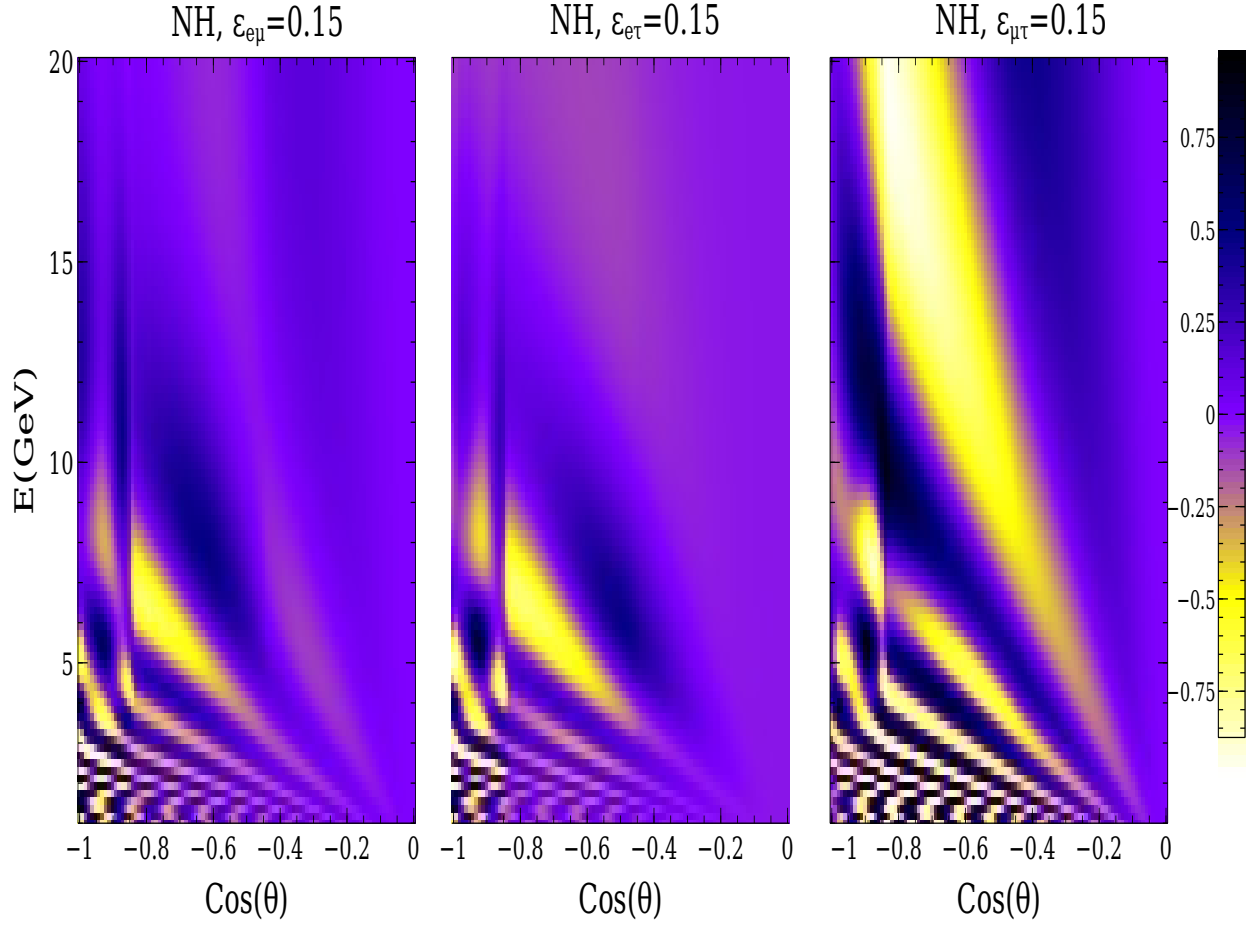


Figure 6.3: Oscillogram pattern of $\Delta P_{\mu\mu}$ with non-zero $\epsilon_{e\mu}, \epsilon_{e\tau}, \epsilon_{\mu\tau}$.

to be non-zero at a time. Since the parameters $\epsilon_{e\mu}, \epsilon_{e\tau}$ appear in the first order expression (Eq. (6.8)), they naturally have a larger impact as compared to $\epsilon_{\mu\tau}$ and, in the favourable situation, $|\Delta P_{e\mu}|$ can be as large as 0.5. This is to be contrasted with $|\Delta P_{\mu\mu}|$ which could take values as large as 1 under favourable conditions. Also, if we look at Eq. (6.8), we note that $\epsilon_{e\mu}$ and $\epsilon_{e\tau}$ appear on equal footing as far as $P_{e\mu}^{NSI}$ is concerned.

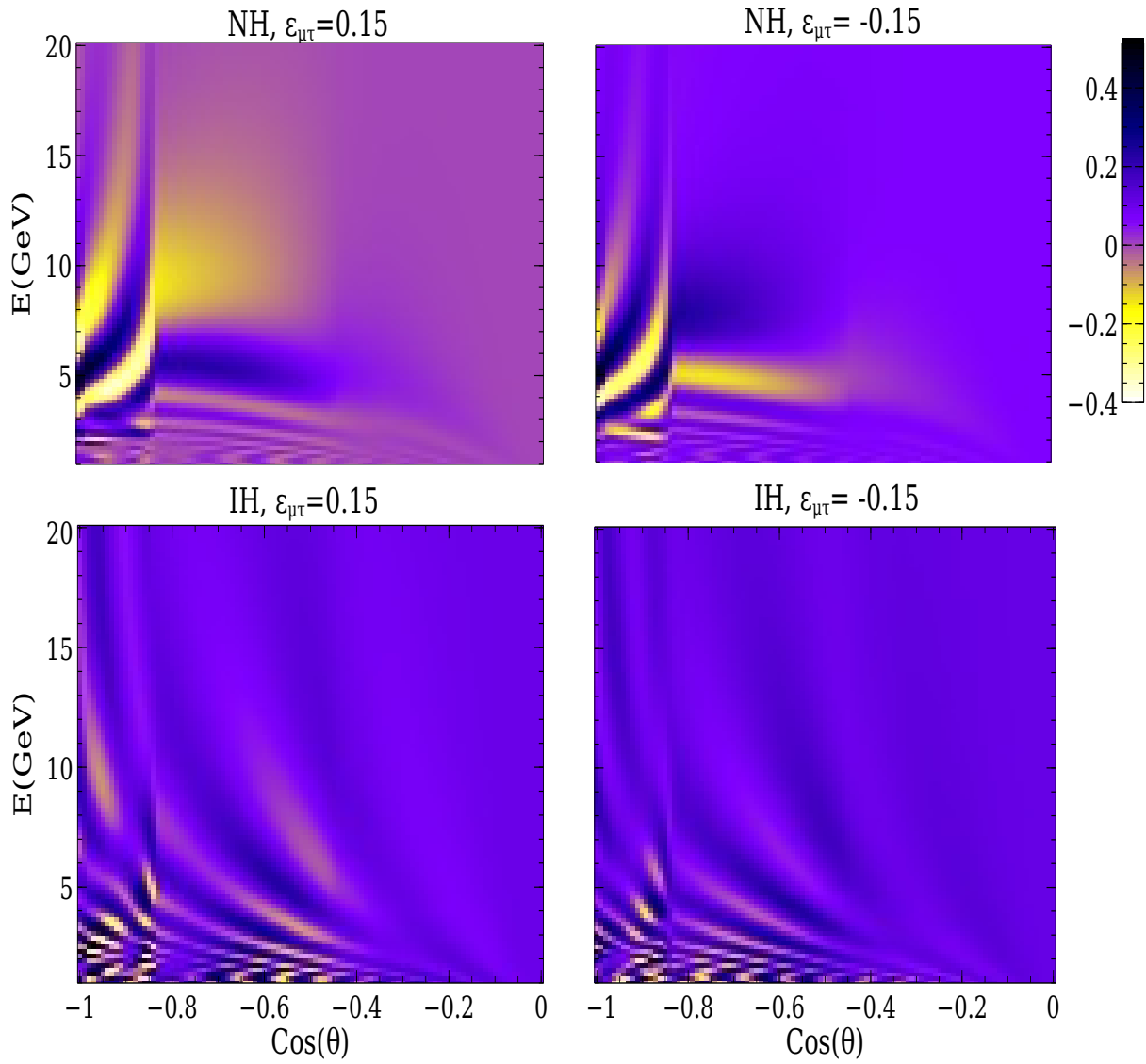


Figure 6.4: Oscillograms of $\Delta P_{e\mu}$ for the NSI parameter $\epsilon_{\mu\tau}$.

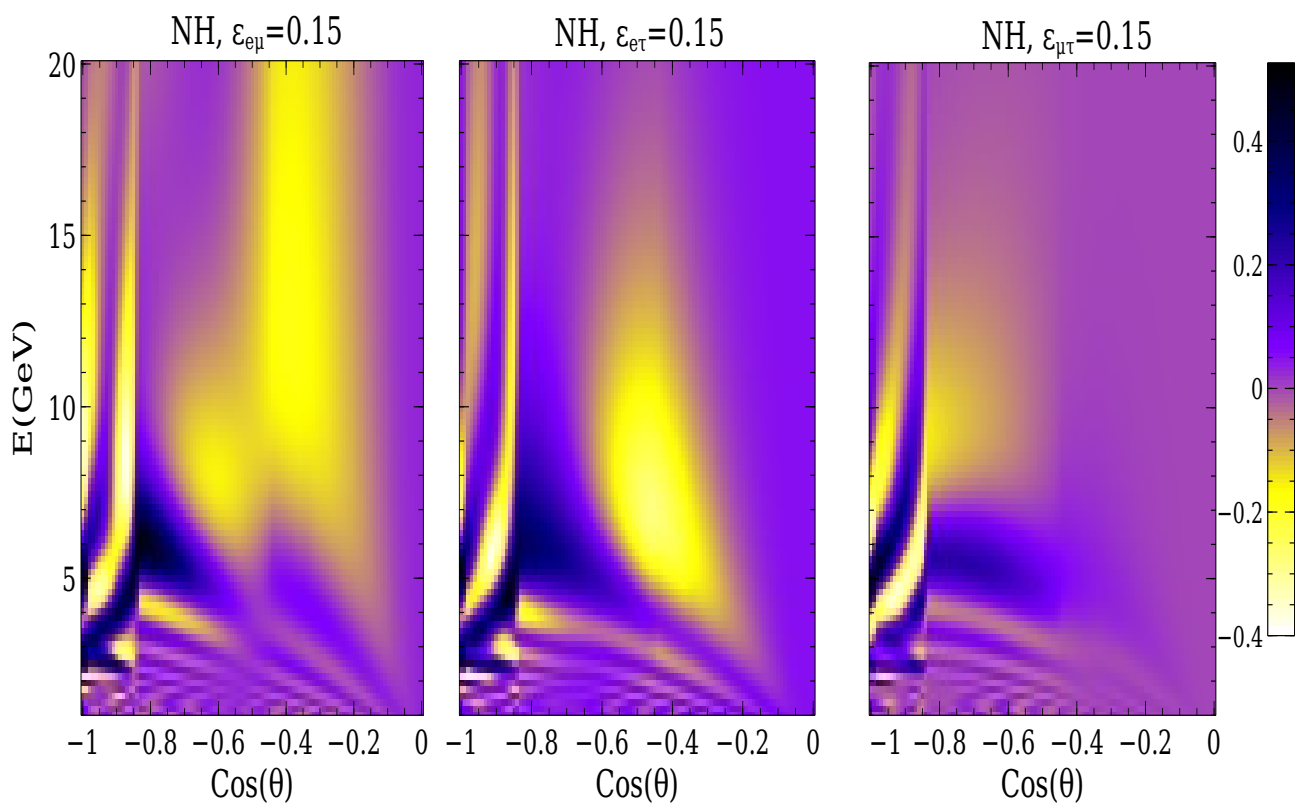


Figure 6.5: The effect of $\epsilon_{e\mu}$, $\epsilon_{e\tau}$, $\epsilon_{\mu\tau}$ on the oscillogram of $\Delta P_{e\mu}$.

6.4 θ_{23} Octant determination in presence of NSI using the muon disappearance channel

If we closely examine the expression for muon neutrino disappearance probability, we note that in vacuum, the two flavour expression depends on $\sin^2 2\theta_{23}$. In matter (in the OMSD approximation) too, the leading order term is proportional to $\sin^2 2\theta_{23}$. This leads to octant degeneracy which means that θ_{23} and $\pi/2 - \theta_{23}$ are indistinguishable. For a given value of $\sin^2 2\theta_{23} = X$, the two degenerate solutions for θ_{23} are,

$$\theta_{23} = \frac{\sin^{-1} \sqrt{X}}{2} \quad \text{or,} \quad \theta_{23} = \frac{\pi}{2} - \frac{\sin^{-1} \sqrt{X}}{2} \quad (6.13)$$

Obviously, for maximal 23 mixing, the two coincide and $\theta_{23} = \pi/4$ uniquely. However for non-maximal ($X \neq 1$) mixing, there is clearly an ambiguity in determining the true value of θ_{23} , since there exist two degenerate solutions : one in the lower octant (LO) and other in the higher octant (HO) (see Eq. (6.13)). From Table. 1.1, we note that there is a hint for the value of $\sin^2 \theta_{23}$ to be non-maximal and the preferred value lies in the HO for both the hierarchies (ignoring that there is a local minima in the LO for the case of NH). The data indicates an average value of $\sin^2 \theta_{23} \sim 0.57$ which leads to $\theta_{23} \simeq 49^\circ$ and the corresponding value of $X = 0.98$. Now for $X = 0.98$, one can have $\theta_{23} \simeq 0.43$ (41°) and $\theta_{23} \simeq 0.86$ (49°) which correspond to $\sin^2 \theta_{23} \simeq 0.43$ and $\sin^2 \theta_{23} \simeq 0.57$ respectively. If we call the true value as $\sin^2 \theta_{23}(true)$, and the false value as, $\sin^2 \theta_{23}(false) = 1 - \sin^2 \theta_{23}(true)$. This leads to degeneracy as $P_{\alpha\beta}(\sin^2 \theta_{23}(true)) = P_{\alpha\beta}(1 - \sin^2 \theta_{23}(true))$.

For atmospheric neutrinos, the resolution of this degeneracy relies on the resonant earth matter effects and using the OMSD formulae (which are valid for a large range of E and L), one notes that for neutrinos (anti-neutrinos), there is a term $\propto \sin^4 \theta_{23} \sin^2 2\tilde{\theta}_{13}$ which is sensitive to the octant and can be large near MSW resonance for NH (IH). For neutrinos and IH (anti-neutrinos and NH), the vacuum oscillation formula holds which has the dominant term depending on $\sin^2 2\theta_{23}$ as well as a sub-dominant θ_{13} dependent term that can aid in the resolution of degeneracy (via a combination $\sin^2 \theta_{23} \cos 2\theta_{23}$). It is therefore natural to investigate the influence of non-zero NSI parameter $\epsilon_{\mu\tau}$ on resolution of this degeneracy.

In Fig. 6.6, we show the $P_{\mu\mu}$ as a function of $\sin^2 2\theta_{13}$ within the allowed range (Ta-

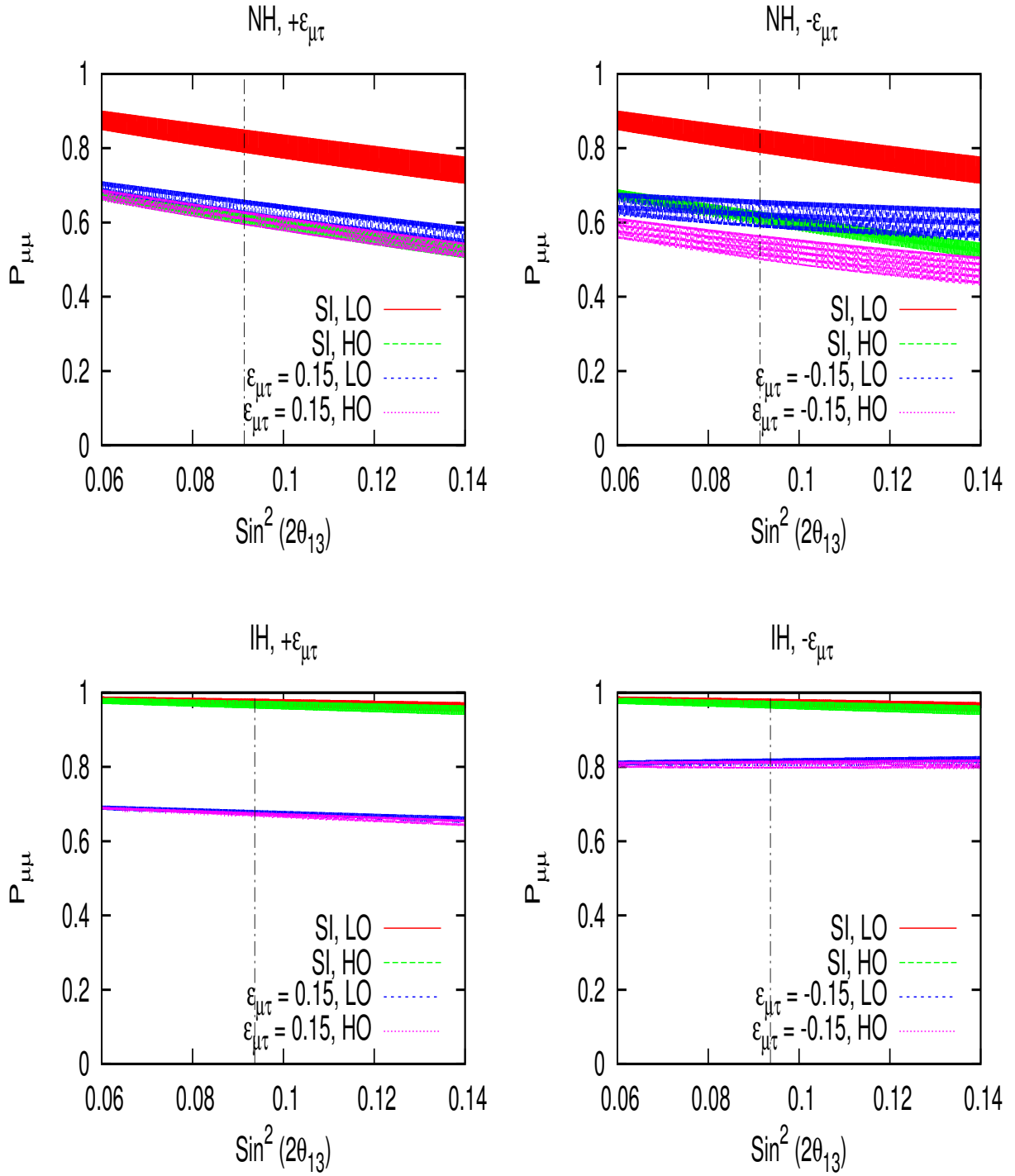


Figure 6.6: $P_{\mu\mu}$ for LO and HO and for NH and IH. Here $L = 5000$ km and $E = 5$ GeV has been taken as input. The width of bands represents variation over $\delta_{CP} \in [-\pi, \pi]$.

ble. 1.1) for $\theta_{23}^{true} = 49^\circ$ and $\theta_{23}^{false} = 41^\circ$. The thickening of curves into bands take into account the variation of δ_{CP} in $[-\pi, \pi]$. The vertical solid line depicts the best-fit value of θ_{13} . We compare the effect of non-zero $\epsilon_{\mu\tau}$ (both signs) for NH and IH respectively. For NH, we see that the curves (red and green) for LO and HO are well separated while for IH the curves for LO and HO overlap in the absence of NSI as expected. If we focus on the vertical line, we note that NSI term can shift the probability from ~ 0.8 to a lower value $\sim 0.6 - 0.65$ for NH, LO and both signs of $\epsilon_{\mu\tau}$. And, NSI, LO (and HO) (blue and magenta) curves overlap with SI, HO (green) for $\epsilon_{\mu\tau} > 0$ while for $\epsilon_{\mu\tau} < 0$, the curves for NSI, LO (blue) barely separate out from NSI, HO (magenta) but still SI, HO curves (green) overlap with NSI, LO (blue). Similarly, for the IH, the probability changes from ~ 1 to a lower value $\sim 0.7 - 0.8$ but the two octants are indistinguishable both in absence and presence of NSI.

Thus, in presence of NSI, the octant determination using matter effects needs to be done more carefully taking into account additional admissible parameters.

6.5 Analysis and Event spectrum

We have generated the atmospheric neutrino events at ICAL detector as mentioned in sec 4.2.1. We have assumed the smearing in energy of neutrino as $\sigma_E = 0.15\sqrt{E}$, angular resolution of the neutrino as $\sigma_\theta = 10^\circ$ and detector efficiency as 85%. We have done our analysis considering simplistic detector properties, such as, neutrino resolutions, efficiencies etc. This is because, our main aim in this chapter is to understand how NSI affects the standard oscillations while propagation. If we can understand the physics without considering complicated detector properties, then later one can use the realistic detector properties. The best fit oscillation parameters have been used as mentioned in Table 1.1. The difference with and without NSI of the ν_μ events using parameters $\epsilon_{\mu\tau}$ and $\epsilon_{\mu e}$ is shown in Fig. 6.7. For ICAL, it is evident that $\Delta N_\mu \simeq \pm 10$ in some of the bins for $\epsilon_{\mu\tau} \neq 0$ while for $\epsilon_{\mu e} \neq 0$, the $\Delta N_\mu \sim \pm 4$. This was expected from the probability level analysis since the leading dependence was through $\epsilon_{\mu\tau}$.

We have followed the statistical technique as mentioned in 4.2.2. We have marginalize χ^2 within the 3σ range as mention in Table 1.1. In our analysis, we have assumed a particular hierarchy, because primary goal of ICAL is to find hierarchy. Hence, when constraints on NSI parameter will be analysed, by that time hierarchy will be known preciously.

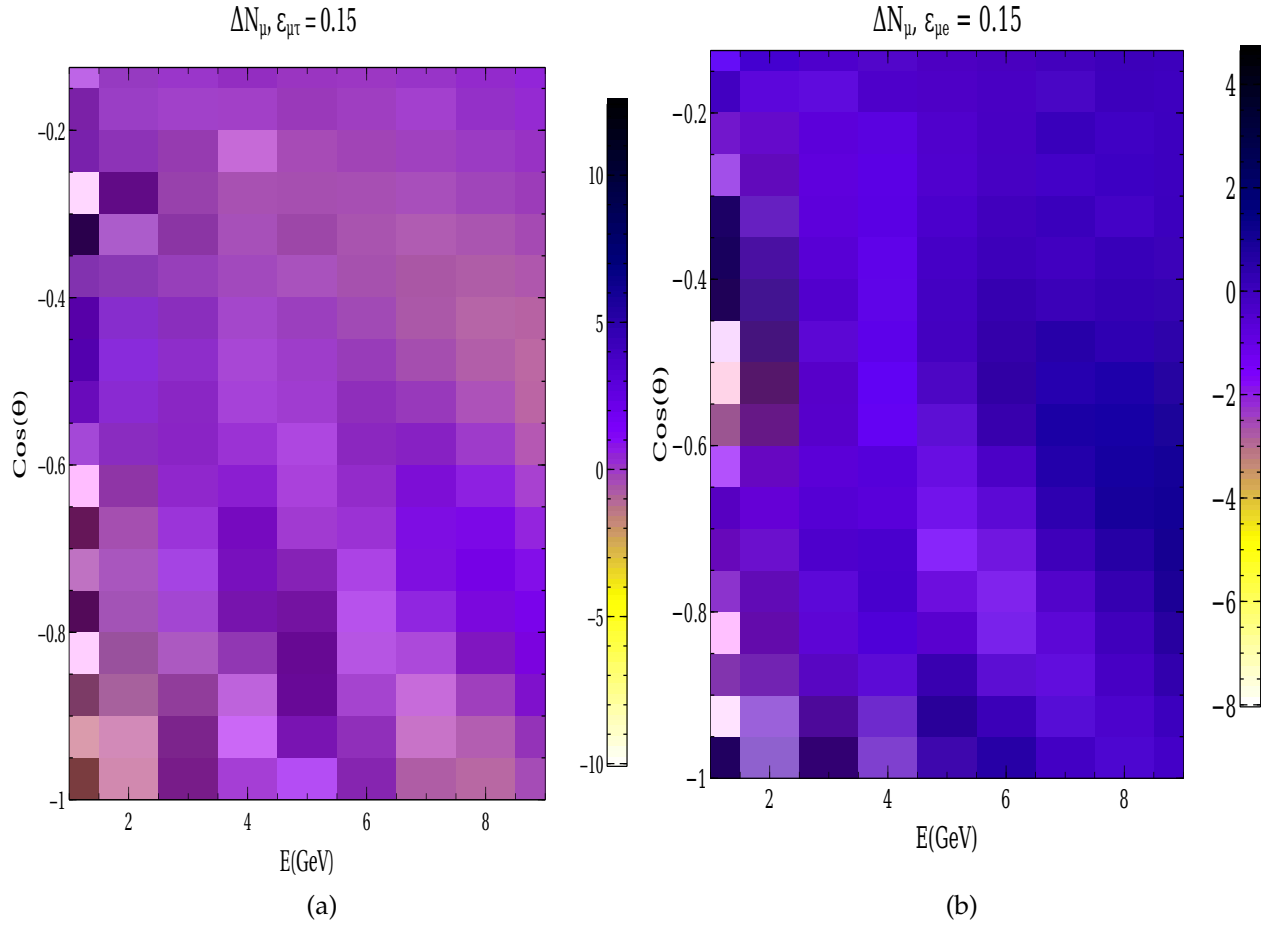


Figure 6.7: The difference with and without NSI of ν_μ (only) events for non-zero $\epsilon_{\mu\tau}$ (left) and $\epsilon_{\mu e}$ (right). All the data are generated for 500 kt-yr of exposure for magnetized ICAL assuming NH as the true hierarchy.

6.6 Constraints on $\epsilon_{\mu\tau}$, $\epsilon_{\mu e}$, $\epsilon_{e\tau}$

We have shown the constraints on $\epsilon_{\mu\tau}$, $\epsilon_{\mu e}$, $\epsilon_{e\tau}$ with ICAL detector of fiducial volume 500 kt-yr. At first, we have taken the limits on these NSI parameters as mentioned in eq. 6.4. We have considered both the positive and negative values. The bounds on $\epsilon_{\mu\tau}$ and $\epsilon_{\mu e}$ are shown in the left and right panel of figure 6.8 respectively. Constraints on $\epsilon_{e\tau}$ is shown in figure 6.9. We have taken other values of NSI parameters as zero, while calculating the constraints on one parameter. This shows that the ICAL will be able to provide best constraints on $\epsilon_{\mu\tau}$. It can be understood easily, because for ICAL dominant channel is $P_{\mu\mu}$

and $\epsilon_{\mu\tau}$ has maximum effect on $P_{\mu\mu}$. The constraints are larger for Inverted hierarchy. This is because the dominant contribution is coming from $P_{\mu\mu}$. If we examine the plots of $\Delta P_{\mu\mu}$ and $\Delta P_{\mu e}$ (Figs. 6.2 and 6.4), we note that there are larger regions in $E - \cos\theta$ parameter space in case of IH than NH for $\Delta P_{\mu\mu}$. It can be noted that the opposite is seen in case of $\Delta P_{\mu e}$ - the regions with large change in probability actually shrink for IH compared to NH. But, since the contribution from $P_{e\mu}$ to N_μ is suppressed by the electron to muon flux ratio for the atmospheric neutrinos and also the maximum possible change is $\sim \pm 0.5$ (which is much smaller than $\sim \pm 1$ for $\Delta P_{\mu\mu}$), this does not nullify the large changes induced due to $P_{\mu\mu}$.

Left panel of figure 6.10 shows the contour in $\epsilon_{\mu\tau} - \epsilon_{\mu e}$ plane. The contour shows the regions in $\epsilon_{\mu\tau} - \epsilon_{\mu e}$ plane for which ICAL can not distinguish between SI and NSI with 90%(green solid) and 95%(red dotted) C.L. respectively. Similar, 6.11 and 6.12 show the regions in $\epsilon_{e\tau} - \epsilon_{\mu e}$ and $\epsilon_{\mu\tau} - \epsilon_{e\tau}$ plane respectively.

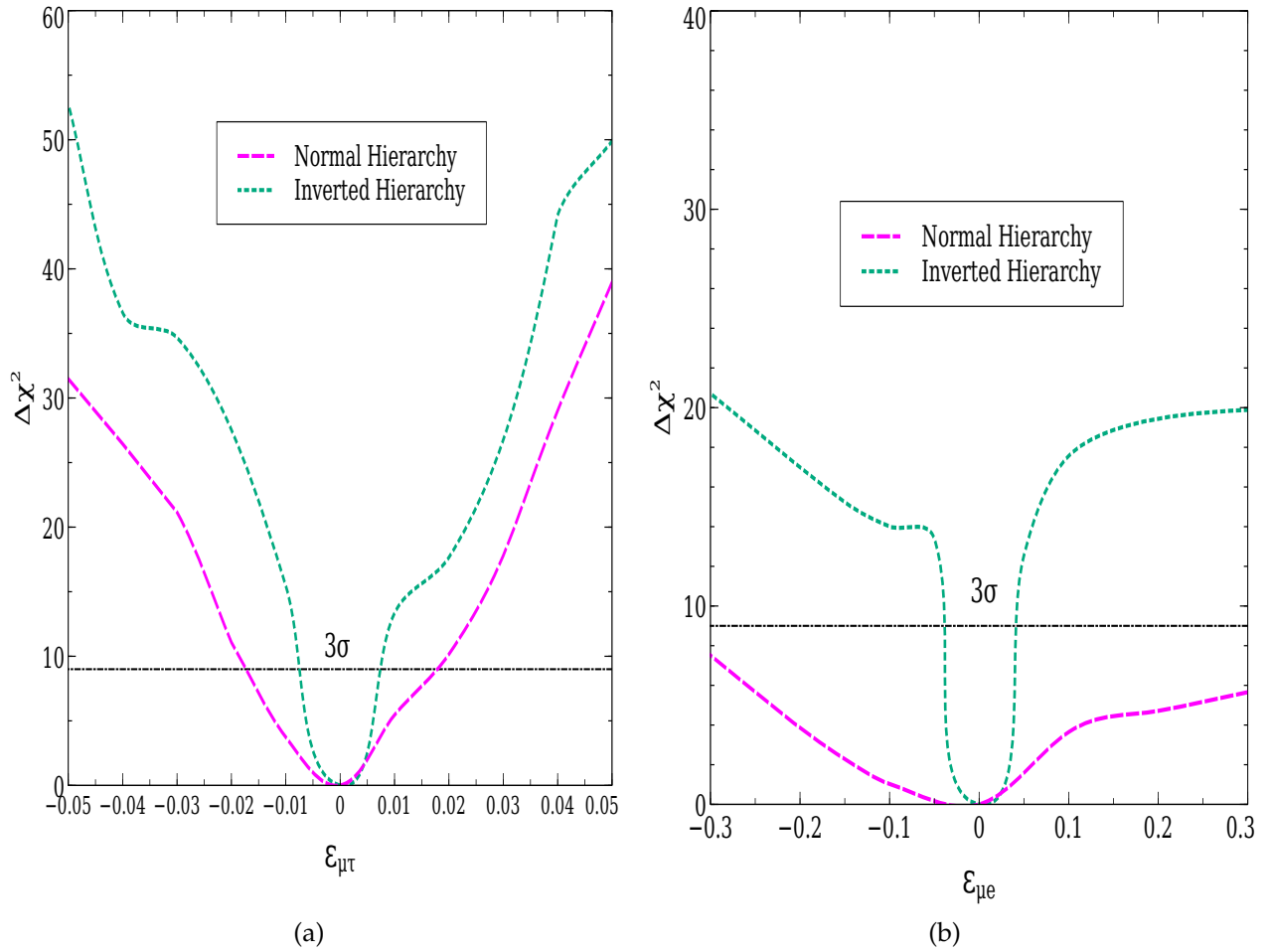


Figure 6.8: Constraints on NSI parameters $\epsilon_{\mu\tau}$ (left) and $\epsilon_{\mu e}$ (right) with ICAL detector for 500 kt-yr fiducial volume. Magenta and green curve are for Normal and Inverted hierarchy respectively.

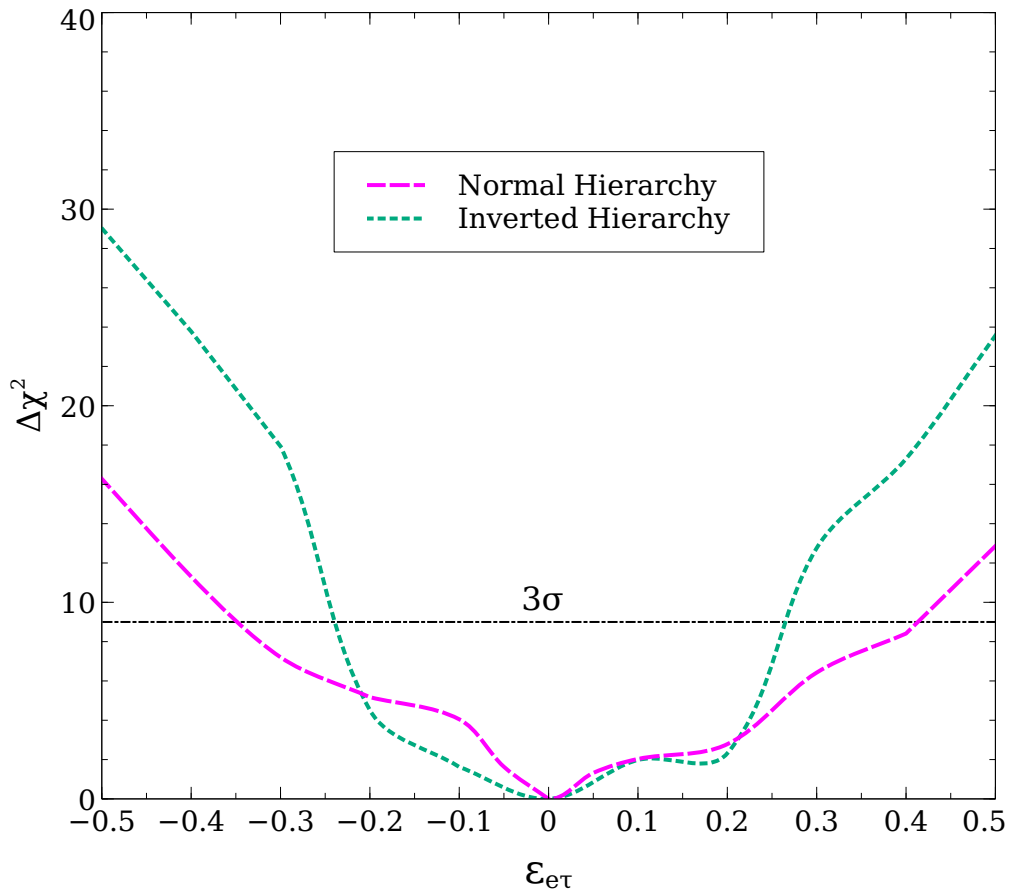


Figure 6.9: Constraints on NSI parameters $\epsilon_{e\tau}$ with ICAL detector for 500 kt-yr fiducial volume. Magenta and green curve are for Normal and Inverted hierarchy respectively.

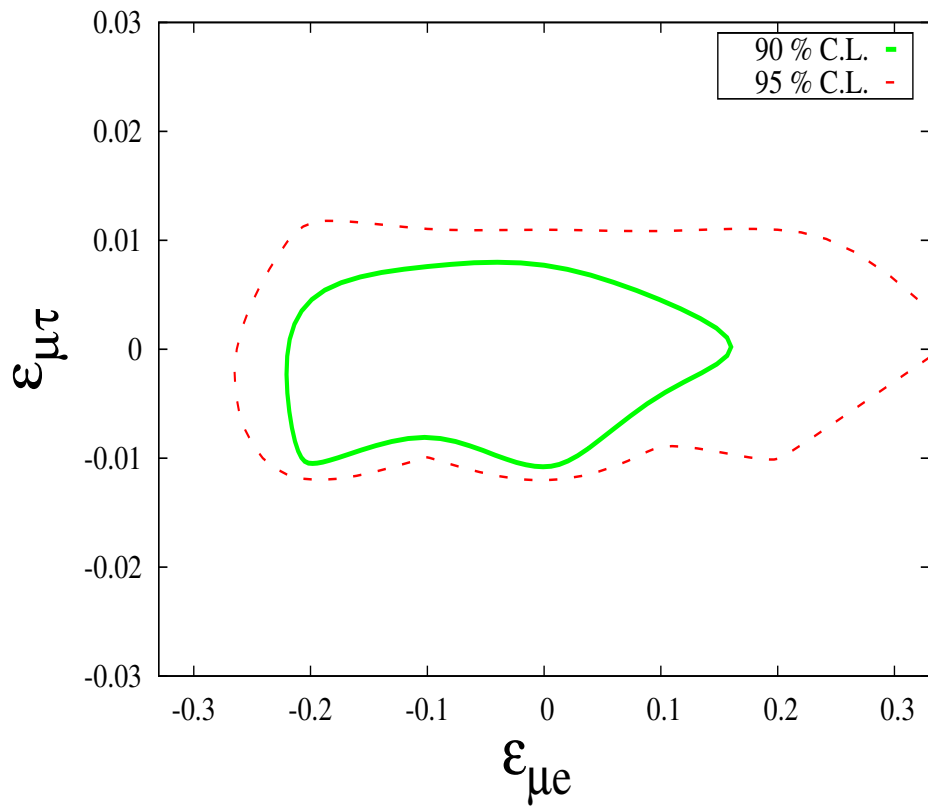


Figure 6.10: Contours of exclusion between SI and NSI in $\epsilon_{\mu\tau}$ - $\epsilon_{\mu e}$ plane with ICAL detector of fiducial volume 500kt-yr. NH is taken as true hierarchy.

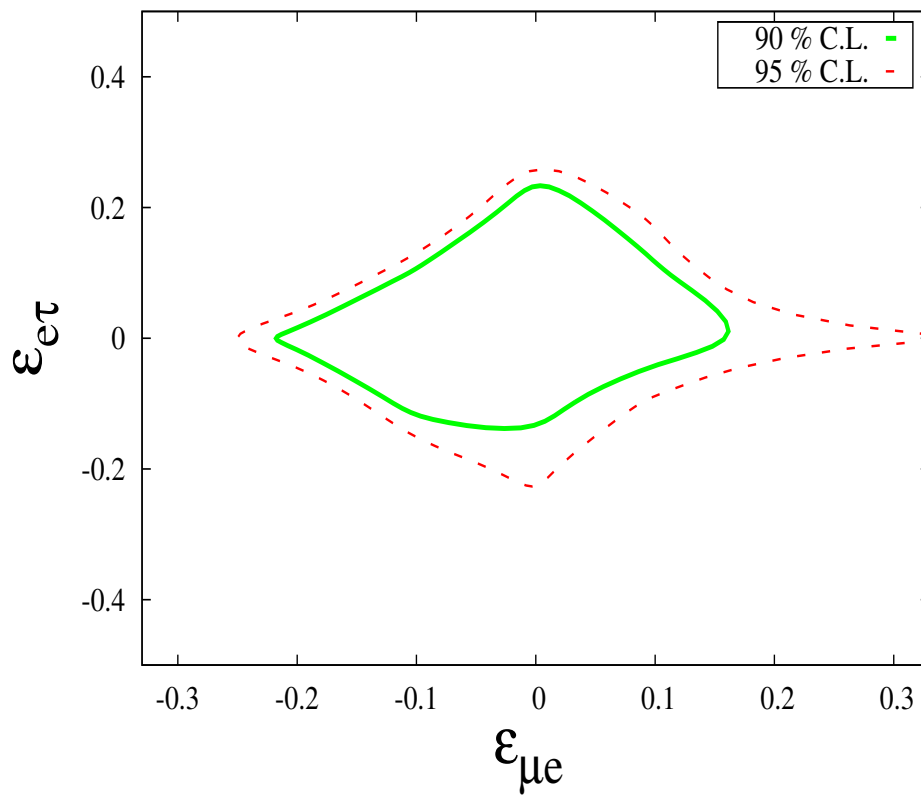


Figure 6.11: Contours of exclusion between SI and NSI in $\epsilon_{e\tau} - \epsilon_{\mu e}$ plane with ICAL detector of fiducial volume 500kt-yr. NH is taken as true hierarchy.

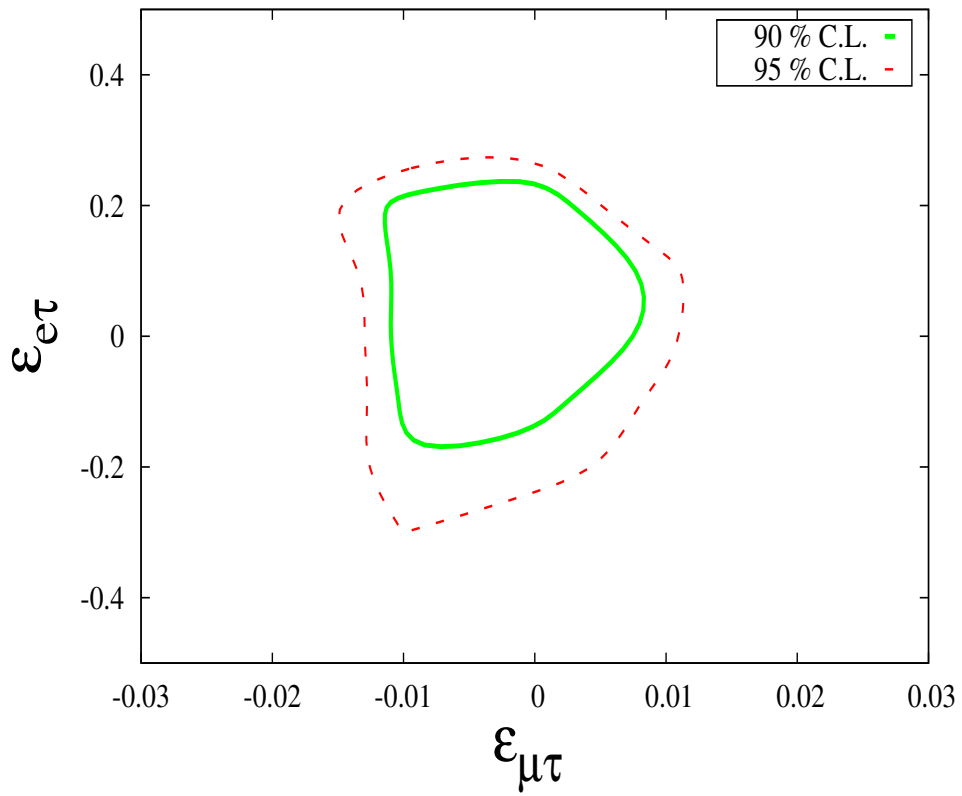


Figure 6.12: Contours of exclusion between SI and NSI in $\epsilon_{\mu\tau}$ - $\epsilon_{e\tau}$ plane with ICAL detector of fiducial volume 500kt-yr. NH is taken as true hierarchy.

Chapter 7

Summary

In this thesis, we have studied the simulation of muons and the sensitivity to new physics for the ICAL detector. Using standard oscillations, we have also shown the possibility of determining the octant of θ_{23} at ICAL in conjunction with T2K and NO ν A data. In new physics searches, we have shown that it is possible to constrain Lorentz/CPT violation in the neutrino sector, and the effect of non-standard interactions on the oscillation pattern of atmospheric neutrinos.

7.1 Summary of simulation of muons

The proposed ICAL detector geometry has been simulated using the GEANT4 package. Muons are the minimum ionizing particle, it generates clean, long tracks inside a detector compared to other leptons. Hence, the muon is the most important detected particle as far as ICAL is concerned. For each energy and angle bin, we propagate 10000 muons uniformly from a vertex position located at the central region of the detector, where the magnetic field is uniform. When the muon passes through the RPC, it gives a signal which is counted as a hit. We have then described how those hits at different layers form a cluster. From all possible clusters, the track finder finds the possible tracklets which are input to the track fitter. A Kalman filter based algorithm is used to fit the tracks based on their bending in the magnetic field. Each muon track is then analysed using momentum resolution, angle resolution, reconstruction efficiency and relative charge identification ef-

efficiency. We carry out the analysis of muon with momentum range from 1-20 GeV/c and direction $\cos(\theta) > 0.35$. We show that momentum resolution is about 9-14%. The reconstruction efficiency is about 80% in all most all the regions of the detector. The direction resolution of muon is very good, it is better than a degree for all angles and momentum greater 4 GeV/C. The excellent direction resolution of muon is one of the most key factor for the study of the neutrino mass hierarchy. The relative charge identification efficiency is about 98% over all the range of momentum and angle.

7.2 Summary of the Octant sensitivity study

In this chapter, we study the possibilities of determining the octant of the atmospheric mixing angle θ_{23} at the ICAL detector, in conjunction with T2K and NO ν A. Although the octant degeneracy conventionally refers to the indistinguishability between θ_{23} and $\pi/2 - \theta_{23}$, we have generalized this to include the whole range of allowed value of θ_{23} in the wrong octant in our analysis.

At first, we present a probability level discussion on the effect of uncertainty in θ_{13} , δ_{CP} and values of θ_{23} in the wrong octant for atmospheric neutrino and long baseline experiment. The following features has been shown in our study: Atmospheric neutrinos which traverse a baseline of 5000 km can lift the intrinsic octant degeneracy in $P_{\mu\mu}$ and the octant degeneracy with θ_{13} and δ_{CP} in $P_{\mu e}$ with the help of strong matter effects. This is because the term $\sin^2 2\theta_{13}^m$ becomes close to 1 at or near matter resonance, and this makes the leading-order term proportional to $\sin^2 \theta_{23}$ ($\sin^4 \theta_{23}$) in $P_{\mu e}$ ($P_{\mu\mu}$) dominate, giving distinct values in the two octants irrespective of the vacuum value of θ_{13} . For smaller baselines, where the matter effect is small, the appearance probability $P_{\mu e}$ displays a degeneracy of the θ_{23} octant with the values of θ_{13} and δ_{CP} due to its dependence on the combination $\sin^2 \theta_{23} \sin^2 2\theta_{13}$ at leading order as well as in its subleading δ_{CP} dependent terms. The disappearance probability $P_{\mu\mu}$ suffers from an intrinsic octant degeneracy between θ_{23} and $\pi/2 - \theta_{23}$ due to being a function of $\sin^2 2\theta_{23}$ at leading order. We also find that after including the improved precision in θ_{13} from the recent reactor results, the octant degeneracy with respect to θ_{13} is greatly reduced.

We then perform a χ^2 analysis of the octant sensitivity for ICAL, T2K/NO ν A and

perform a combined analysis. The ICAL detector gives a 2σ sensitivity to the octant for $\theta_{23} = 39^\circ$ and $\sin^2 2\theta_{13} = 0.1$ for a true normal hierarchy. Combining the NO ν A and T2K data leads to a higher octant sensitivity due to the addition of sensitivities from the two experiments. The major role played in enhancing the octant sensitivity in these experiments is the addition of priors, especially on θ_{13} , which helps in ruling out the degenerate solutions in the wrong octant. After adding priors one can achieve a $\sim 2\sigma$ sensitivity at $\theta_{23} = 39^\circ$ for $\sin^2 2\theta_{13} = 0.1$ and $\delta_{CP} = 0$ for both normal and inverted hierarchies. We have also shown the combined χ^2 data table for all true value of θ_{23} .

To summarize, we show that the improved precision of θ_{13} and the different dependence on θ_{23} in the disappearance and appearance channels and in vacuum and matter probabilities leads to an enhanced octant sensitivity when long baseline and atmospheric neutrino experiments are combined.

7.3 Summary of Lorentz / CPT violation study

In the next chapter we show that a magnetized iron calorimeter like ICAL, with its attributes of good energy and angular resolution for muons and its charge identification capability can be a useful tool in investigating Lorentz invariance violation and CPT violation stemming from physics at higher energy scales, even though its main physics objective may be hierarchy determination.

First, we describe the phenomenological formalism incorporating CPT violation in neutrino oscillations. We define the effective Hamiltonian of the neutrinos in the flavour basis, and add a generic CPT violating term. The effective new Hamiltonian contains six mixing angle and seven phases. It is clear that the results will depend on the mixing angles in the CPT violation sector. We have examined the effects of three different representative sets of mixing angles characterized by 1) small mixing, 2) large mixing and 3) the same mixing as the PMNS mixing.

Before discussing the results of numerical simulations, we have tried to understand the effects at the level of probabilities. We note that the matter target in our case is CP asymmetric, which will automatically lead to effects similar to those induced by the mixing matrix U_b in the CPT violating sector. In order to separate the effects arising due to dynamical CPT violation from those originating due to the CP asymmetry of the earth, it

helps to consider the difference in the disappearance probabilities with U_b effects turned on and off, respectively. We have presented the difference of the probability in the form of oscillogram. We do this separately for ν_μ and $\bar{\nu}_\mu$ events with NH and IH assumed as the true hierarchy. The oscillogram shows several general features. First effects are uniformly small at shorter baselines irrespective of the value of the energy. The qualitative feature that CPT effects are larger at long baselines continues to be manifest even when one incorporates three flavour mixing and the presence of matter, and this is brought out in all the figures. Secondly, as is well-known, matter effects are large and resonant for neutrinos and NH, and for anti-neutrinos with IH. Thus in both these cases, they mask the (smaller) effect of CPT stemming from U_b . Hence for neutrino events, CPT sensitivity is significantly higher if the hierarchy is inverted as opposed to normal, and the converse is true for anti-neutrino events. Finally, effects are largest for cases 3) and 2), and smaller for case 1). The effect is smaller for case 1) is due to the fact that mixing is very small compared to other two. The origin of the difference for the case 2) and 3) is likely due to the fact that CPT violating effects are smaller when θ_{b13} is large.

Using resolutions, efficiencies, errors and uncertainties generated by ICAL detector simulation, we have calculated reliable sensitivities to the presence of CPTV at the ICAL detector. We carry through the mode of looking at the difference between the case when U_b is non-zero and zero respectively to the event and χ^2 levels in our calculations in this chapter. To use the lepton charge identification capability of a magnetized iron calorimeter optimally, we calculate χ^2 from μ^- and μ^+ events separately. Following this procedure, the contribution arising through matter being CPT asymmetric will expectedly cancel for any given zenith angle and energy. We have carried out our calculations for all three representative cases mentioned above. We find that for both types of hierarchy, ICAL should be sensitive to $\delta b_{31} \gtrsim 4 \times 10^{-23}$ GeV at 99% C.L. with 500 kt-yr of exposure, unless the mixing in the CPTV sector is small. As discussed earlier, CP (and CPT) effects due to earth matter asymmetry are subtracted out.

7.4 Summary of Non standard Interaction study

In this chapter, we describe the effect of non-standard neutrino interactions on the neutrino oscillation pattern of atmospheric neutrinos with the help of ICAL detector. First,

we discuss the framework of Non-Standard Interactions(NSI) of neutrinos with the matter fermions. In general, NSI can impact the neutrino oscillation signals via two kinds of interactions, a) Charge current interactions (CC), b) Neutral current (NC) interactions. CC interactions mainly affect processes only at the source and at the detector. On the other hand, the NC interactions affect the propagation of neutrinos, and we focus on this. Then, we discuss the model-independent bounds on NSI parameters. After that, we have derived the analytic expressions of the oscillation probability in presence of NSI. The NSI term has been added as a perturbation to the standard Hamiltonian. We have used "one mass-squared dominant"(OMSD) approximation to understand the features of the probability expressions.

Apart from the oscillation parameters, the neutrino oscillations probability depends on the neutrino energy and the zenith angle of the direction of the neutrinos. Hence, the oscillation pattern can be fully described by contours of equal oscillation probabilities in the $E\text{-}\cos\theta$ plane. We use the neutrino oscillograms to discuss the effect of neutrino matter interactions on the atmospheric neutrino propagation along with NSI parameters.

We show the effect of $\epsilon_{\mu\tau}$, $\epsilon_{\mu e}$, $\epsilon_{e\tau}$ on the oscillation probability. In the case of $P_{\mu\mu}$, the effect of $\epsilon_{\mu\tau}$ is large compared to the other two. In the case of $P_{\mu e}$, since the parameters $\epsilon_{\mu e}$, $\epsilon_{e\tau}$ appear in the first order expressions, its impact is expectedly more as compared to that of $\epsilon_{\mu\tau}$.

In the next section, we have tried to understand the effect of NSI parameters on the determination of octant of θ_{23} at the level of probability. As $P_{\mu\mu}$ has inherent octant degeneracy, we focus on $P_{\mu\mu}$ to understand whether the NSI parameter can improve or make it more difficult to resolve the degeneracy. The plots in this chapter show that while discussing the octant degeneracy resolution, NSI parameters can mimic the opposite octant.

We calculate the constraints on the three NSI parameters. We have calculated $\Delta\chi^2$ value between two sets of data, one of the data set with non zero value of nsi parameter at a time and other set as standard interaction of neutrinos. The study shows that the ICAL will be able to provide better constraints on $\epsilon_{\mu\tau}$ as expected from the probability expressions and from the event plot. Finally, the contours presented show the region in ϵ 's plane for which the ICAL can not distinguish between SI and NSI with 90% and 95% C.L.

In conclusion, the thesis contents the first study of the simulation of muons at the ICAL detector, which is very crucial to achieve the neutrino oscillation physics goals as well as new physics searches. We have shown that 3σ octant sensitivity can be achieved by combining ICAL with T2K and NO ν A data. Besides the standard oscillation physics, we have also shown new physics searches at ICAL. The thesis shows that ICAL can provide significant information on CPT violation and Non-Standard neutrino interactions. The updates and improvements in the simulation of muon and technique of our analysis will improve the results presented in the thesis.

Bibliography

- [1] W. Pauli., "Letter by Wolfgang Pauli to the attendees of the Tübingen conference", From the CERN archive, <http://cdsweb.cern.ch/record/83282>
- [2] O. Hahn and L. Meitner, "Über die absorption der β -strahlen einiger radioelemente," *Physikalische Zeitschrift*, vol. 9, pp. 312-333, 1908.
- [3] J. Chadwick, "Intensitätsverteilung im magnetischen spektrum der β - strahlen von radium b + c," *Verhandlungen der deutschen physikalischen Gesellschaft*, vol. 16, pp. 383-391, 1914.
- [4] Cowan et al. s.l., "Detection of the Free Neutrino: a Confirmation", *Science* 124:3212.103, 1956
- [5] L.M. Lederman et al. s.l., "Observation of the High-Energy Neutrino Reactions and the Existence of Two Kinds of Neutrinos", *Phys. Rev. Lett.* 9:36-44, 1962
- [6] DONuT Collaboration. s.l., "Observation of Tau Neutrino Interactions", *Phys. Lett. B*, 504:218-224, 2001
- [7] T. J. Haines, R. M. Bionta, G. Blewitt, C. B. Bratton, D. Casper, R. Claus, B. G. Cortez and S. Errede *et al.*, "Calculation of Atmospheric Neutrino Induced Backgrounds in a Nucleon Decay Search," *Phys. Rev. Lett.* **57**, 1986 (1986).
- [8] S. P. Ahlen *et al.* [MACRO Collaboration], "Atmospheric neutrino flux measurement using upgoing muons," *Phys. Lett. B* **357**, 481 (1995).
- [9] Hirata KS *et al.*, "Experimental Study of the Atmospheric Neutrino Flux", *Phys. Lett. B* **205**:416 (1988)

- [10] Y. Ashie, et al., "Measurement of atmospheric neutrino oscillation parameters by Super-Kamiokande I", *Phys. Rev. D* **71** 112005 (2005) ;
 Y. Fukuda, et al., "Evidence for Oscillation of Atmospheric Neutrinos", *Phys. Rev. Lett* **81** (1998) 1562-1567
- [11] Q.R. Ahmad et al., "Measurement of the Rate of $\nu_e + d \rightarrow p + p + e^-$ Interactions Produced by B^8 Solar Neutrinos at the Sudbury Neutrino Observatory", *Phys. Rev. Lett* **87** (2001) 071301;
 Q.R. Ahmad et al., "Direct Evidence for Neutrino Flavor Transformation from Neutral-Current Interactions in the Sudbury Neutrino Observatory", *Phys. Rev. Lett* **89** (2002) 011301;
 S.N. Ahmed et al., "Measurement of the Total Active B^8 Solar Neutrino Flux at the Sudbury Neutrino Observatory with Enhanced Neutral Current Sensitivity", *Phys. Rev. Lett* **92** (2004) 181301;
- [12] T. K. Gaisser and M. Honda, "Flux of atmospheric neutrinos," *Ann. Rev. Nucl. Part. Sci.* **52**, 153 (2002) [hep-ph/0203272].
- [13] M. G. Aartsen *et al.* [IceCube Collaboration], "Observation of High-Energy Astrophysical Neutrinos in Three Years of IceCube Data", *Phys. Rev. Lett.* **113**, 101101 (2014) [arXiv:1405.5303 [astro-ph.HE]].
- [14] B. Pontecorvo, Sov., "Neutrino Experiments and the Problem of Conservation of Leptonic Charge", *Phys. JETP* **26**, 984 (1968) [*Zh. Eksp. Teor. Fiz.* **53**, 1717 (1967)]
- [15] Z. Maki, M. Nakagawa and S. Sakata, "Remarks on the Unified Model of Elementary Particles", *Prog. Theor. Phys.* **28**, 870 (1962).
- [16] J. Burguet-Castell, M. Gavela, J. Gomez-Cadenas, P. Hernandez, and O. Mena, "On the Measurement of leptonic CP violation", *Nucl.Phys.* **B608** (2001) 301–318, [<http://xxx.lanl.gov/abs/hep-ph/0103258>hep-ph/0103258].
- [17] E. K. Akhmedov, R. Johansson, M. Lindner, T. Ohlsson, and T. Schwetz, " Series expansions for three flavor neutrino oscillation probabilities in matter", *JHEP* **0404** (2004) 078, [<http://xxx.lanl.gov/abs/hep-ph/0402175>hep-ph/0402175].
- [18] A. Cervera, A. Donini, M. Gavela, J. Gomez Cadenas, P. Hernandez, et al., "Golden measurements at a neutrino factory", *Nucl.Phys.* **B579** (2000) 17–55, [<http://xxx.lanl.gov/abs/hep-ph/0002108>hep-ph/0002108].

- [19] M. Freund, "Analytic approximations for three neutrino oscillation parameters and probabilities in matter", *Phys.Rev.* **D64** (2001) 053003, [<http://xxx.lanl.gov/abs/hep-ph/0103300>].
- [20] K. Kimura, A. Takamura, and H. Yokomakura, "Exact formula of probability and CP violation for neutrino oscillations in matter", *Phys. Lett.* **B537** (2002) 86–94, [<http://xxx.lanl.gov/abs/hep-ph/0203099>].
- [21] L. Wolfenstein, "Neutrino oscillations in matter", *Phys. Rev. D* **17**, 2369 (1978);
S. P. Mikheev and A. Y. Smirnov, "The MSW effect and Solar Neutrinos", *Sov. J. Nucl. Phys.* **42**, 913 (1985) [*Yad. Fiz.* **42**, 1441 (1985)];
S. P. Mikheev and A. Y. Smirnov, *Nuovo Cim. C* **9**, 17 (1986);
V. D. Barger, K. Whisnant, S. Pakvasa and R. J. N. Phillips, "Matter effect on three-neutrino oscillations ", *Phys. Rev. D* **22**, 2718 (1980).
- [22] A. Dziewonski and D. Anderson, "Preliminary reference earth model", *Phys.Earth Planet.Interiors* **25** (1981) 297–356.
- [23] Y. Itow *et al.* [T2K Collaboration], "The JHF-Kamioka neutrino project", [hep-ex/0106019](http://xxx.lanl.gov/abs/hep-ex/0106019).
- [24] Ambats, I. et al. [MINOS Collaboration], NUMI-L-337, FERMILAB-DESIGN-1998-02
- [25] F. P. An *et al.* [DAYA-BAY Collaboration], "Observation of electron-antineutrino disappearance at Daya Bay", *Phys. Rev. Lett.* **108**, 171803 (2012) [[arXiv:1203.1669](https://arxiv.org/abs/1203.1669) [hep-ex]].
- [26] J. K. Ahn *et al.* [RENO Collaboration], "Observation of Reactor Electron Antineutrino Disappearance in the RENO Experiment", *Phys. Rev. Lett.* **108**, 191802 (2012) [[arXiv:1204.0626](https://arxiv.org/abs/1204.0626) [hep-ex]].
- [27] Y. Abe *et al.* [Double Chooz Collaboration], "Reactor electron antineutrino disappearance in the Double Chooz experiment", *Phys. Rev. D* **86**, 052008 (2012) [[arXiv:1207.6632](https://arxiv.org/abs/1207.6632) [hep-ex]].
- [28] D. V. Forero, M. Tortola and J. W. F. Valle, "Neutrino oscillations refitted", [arXiv:1405.7540](https://arxiv.org/abs/1405.7540) [hep-ph].

- [29] J. D. Bjorken and S. D. Drell. Relativistic Quantum Fields. New York, McGraw-Hill, 1965
- [30] R. P. Feynman and S. Weinberg. Elementary particles and the laws of physics. Cambridge University Press, 1987
- [31] M. E. Peskin and D. V. Schroeder. An Introduction to Quantum Field Theory. Westview Press, 1995
- [32] O. W. Greenberg, "CPT violation implies violation of Lorentz invariance", Phys. Rev. Lett. **89**, 231602 (2002) [hep-ph/0201258].
- [33] D. Colladay and V. A. Kostelecky, "CPT violation and the standard model", Phys. Rev. D **55**, 6760 (1997) [hep-ph/9703464].
- [34] D. Colladay and V. A. Kostelecky, "Lorentz violating extension of the standard model", Phys. Rev. D **58**, 116002 (1998) [hep-ph/9809521].
- [35] V. A. Kostelecky and M. Mewes, "Lorentz and CPT violation in the neutrino sector", Phys. Rev. D **70**, 031902 (2004) [hep-ph/0308300].
- [36] N. Arkani-Hamed, S. Dimopoulos, G. R. Dvali and J. March-Russell, "Neutrino masses from large extra dimensions", Phys. Rev. D **65**, 024032 (2001) [arXiv:hep-ph/9811448].
- [37] S. J. Huber and Q. Shafi, "Neutrino oscillations and rare processes in models with a small extra dimension", Phys. Lett. B **512**, 365 (2001) [arXiv:hep-ph/0104293].
- [38] Y. Grossman and M. Neubert, "Neutrino masses and mixings in non-factorizable geometry", Phys. Lett. B **474**, 361 (2000) [arXiv:hep-ph/9912408].
- [39] G. Barenboim and J. D. Lykken, "A model of CPT violation for neutrinos", Phys. Lett. B **554**, 73 (2003) [arXiv:hep-ph/0210411].
- [40] W. M. Yao *et al.* [Particle Data Group], "Review of particle physics", J. Phys. G **33**, 1 (2006).
- [41] C. Leonidopoulos [BELLE collaboration], " B_d^0 anti- B_d^0 mixing and CPT tests at Belle", arXiv:hep-ex/0107001.

- [42] G. W. Bennett *et al.* [Muon ($g-2$) Collaboration], "Search for Lorentz and CPT Violation Effects in Muon Spin Precession", *Phys. Rev. Lett.* **100**, 091602 (2008) [arXiv:0709.4670 [hep-ex]].
- [43] S. R. Coleman and S. L. Glashow, "High-energy tests of Lorentz invariance", *Phys. Rev. D* **59**, 116008 (1999) [hep-ph/9812418].
- [44] V. D. Barger, S. Pakvasa, T. J. Weiler and K. Whisnant, "CPT odd resonances in neutrino oscillations", *Phys. Rev. Lett.* **85**, 5055 (2000) [hep-ph/0005197].
- [45] J. N. Bahcall, V. Barger and D. Marfatia, "How accurately can one test CPT conservation with reactor and solar neutrino experiments?", *Phys. Lett. B* **534**, 120 (2002) [hep-ph/0201211].
- [46] A. Datta, R. Gandhi, P. Mehta and S. U. Sankar, "Atmospheric neutrinos as a probe of CPT and Lorentz violation", *Phys. Lett. B* **597**, 356 (2004) [hep-ph/0312027].
- [47] A. Dighe and S. Ray, "CPT violation in long baseline neutrino experiments: A Three flavor analysis", *Phys. Rev. D* **78**, 036002 (2008) [arXiv:0802.0121 [hep-ph]].
- [48] J. S. Diaz, V. A. Kostelecky and M. Mewes, "Perturbative Lorentz and CPT violation for neutrino and antineutrino oscillations", *Phys. Rev. D* **80**, 076007 (2009) [arXiv:0908.1401 [hep-ph]].
- [49] J. S. Diaz, "Long-baseline neutrino experiments as tests for Lorentz violation", arXiv:0909.5360 [hep-ph].
- [50] A. Samanta, "Probing CPT violation in neutrinos oscillation: A three flavor analysis", *Phys. Lett. B* **693**, 296 (2010) [arXiv:1005.4851 [hep-ph]].
- [51] N. Engelhardt, A. E. Nelson and J. R. Walsh, "Apparent CPT Violation in Neutrino Oscillation Experiments", *Phys. Rev. D* **81**, 113001 (2010) [arXiv:1002.4452 [hep-ph]].
- [52] S. T. Scully and F. W. Stecker, "Testing Lorentz Invariance with Neutrinos from Ultrahigh Energy Cosmic Ray Interactions", *Astropart. Phys.* **34**, 575 (2011) [arXiv:1008.4034 [astro-ph.CO]].
- [53] J. Ellis, H. -T. Janka, N. E. Mavromatos, A. S. Sakharov and E. K. G. Sarkisyan, "Probing Lorentz Violation in Neutrino Propagation from a Core-Collapse Supernova", *Phys. Rev. D* **85**, 045032 (2012) [arXiv:1110.4848 [hep-ph]].

- [54] Koranga, Bipin Singh and Kumar, Vinod and Jha, A., *Int. J. Theor. Phys.* **50** (2011), 2609-2613.
- [55] V. A. Mitsou, "Dark matter searches at LHC", *J. Phys. Conf. Ser.* **335**, 012003 (2011) [arXiv:1104.1149 [hep-ph]].
- [56] I. Motie and S. -S. Xue, "High energy neutrino oscillation at the presence of the Lorentz Invariance Violation", *Int. J. Mod. Phys. A* **27**, 1250104 (2012) [arXiv:1206.0709 [hep-ph]].
- [57] P. W. Gorham, A. Connolly, P. Allison, J. J. Beatty, K. Belov, D. Z. Besson, W. R. Binns and P. Chen *et al.*, "Implications of ultra-high energy neutrino flux constraints for Lorentz-invariance violating cosmogenic neutrinos", *Phys. Rev. D* **86**, 103006 (2012) [arXiv:1207.6425 [astro-ph.HE]].
- [58] S. Chakraborty, A. Mirizzi and G. Sigl, "Testing Lorentz Invariance with neutrino burst from supernova neutronization", *Phys. Rev. D* **87**, 017302 (2013) [arXiv:1211.7069 [hep-ph]].
- [59] T. Katori [LSND and MiniBooNE and Double Chooz Collaborations], "Tests of Lorentz and CPT violation with neutrinos", *PoS ICHEP* **2012**, 008 (2013) [arXiv:1211.7129 [hep-ph]].
- [60] B. Altschul, "Neutrino Beam Constraints on Flavor-Diagonal Lorentz Violation", *Phys. Rev. D* **87**, 096004 (2013) [arXiv:1302.2598 [hep-ph]].
- [61] Z. -K. Guo and J. -W. Hu, "Nucleosynthesis constraint on Lorentz invariance violation in the neutrino sector", *Phys. Rev. D* **87**, 123519 (2013) [arXiv:1303.2813 [astro-ph.CO]].
- [62] E. Borriello, S. Chakraborty, A. Mirizzi and P. D. Serpico, "Stringent constraint on neutrino Lorentz-invariance violation from the two IceCube PeV neutrinos", *Phys. Rev. D* **87**, 116009 (2013) [arXiv:1303.5843 [astro-ph.HE]].
- [63] J. S. Diaz, A. Kostelecky and R. Lehnert, "Relativity violations and beta decay", *Phys. Rev. D* **88**, 071902 (2013) [arXiv:1305.4636 [hep-ph]].
- [64] F. W. Stecker, "Constraining Superluminal Electron and Neutrino Velocities using the 2010 Crab Nebula Flare and the IceCube PeV Neutrino Events", *Astropart. Phys.* **56**, 16 (2014) [arXiv:1306.6095 [hep-ph]].

- [65] J. S. Diaz, "Lorentz and CPT violation in the Neutrino Sector", arXiv:1307.6845.
- [66] F. Rossi-Torres, "Probing Lorentz Invariance Violation with Neutrino Factories", arXiv:1307.0884 [hep-ph].
- [67] J. S. Diaz, A. Kostelecky and M. Mewes, "Testing Relativity with High-Energy Astrophysical Neutrinos", Phys. Rev. D **89**, 043005 (2014) [arXiv:1308.6344 [astro-ph.HE]].
- [68] J. S. Diaz, "Limits on Lorentz and CPT violation from double beta decay", Phys. Rev. D **89**, 036002 (2014) [arXiv:1311.0930 [hep-ph]].
- [69] H. Nunokawa, S. J. Parke, and J. W. Valle, "CP Violation and Neutrino Oscillations," Prog.Part.Nucl.Phys., vol. 60, pp. 338–402, 2008
- [70] S. Davidson, C. Pena-Garay, N. Rius and A. Santamaria, "Present and future bounds on nonstandard neutrino interactions", JHEP **0303**, 011 (2003) [hep-ph/0302093].
- [71] N. Fornengo, M. Maltoni, R. Tomas and J. W. F. Valle, "Probing neutrino nonstandard interactions with atmospheric neutrino data", Phys. Rev. D **65**, 013010 (2002) [hep-ph/0108043].
- [72] M. C. Gonzalez-Garcia and M. Maltoni, "Atmospheric neutrino oscillations and new physics", Phys. Rev. D **70**, 033010 (2004) [hep-ph/0404085].
- [73] A. Friedland, C. Lunardini and M. Maltoni, "Atmospheric neutrinos as probes of neutrino-matter interactions", Phys. Rev. D **70**, 111301 (2004) [hep-ph/0408264].
- [74] N. Kitazawa, H. Sugiyama and O. Yasuda, "Will MINOS see new physics?", hep-ph/0606013.
- [75] J. Kopp, P. A. N. Machado and S. J. Parke, "Interpretation of MINOS data in terms of non-standard neutrino interactions", Phys. Rev. D **82**, 113002 (2010) [arXiv:1009.0014 [hep-ph]].
- [76] W. A. Mann, D. Cherdack, W. Musial and T. Kafka, "Apparent multiple Δm_{32}^2 in muon anti-neutrino and muon neutrino survival oscillations from non-standard interaction matter effect", Phys. Rev. D **82**, 113010 (2010) [arXiv:1006.5720 [hep-ph]].

- [77] G. Mitsuka *et al.* [Super-Kamiokande Collaboration], "Study of Non-Standard Neutrino Interactions with Atmospheric Neutrino Data in Super-Kamiokande I and II", *Phys. Rev. D* **84**, 113008 (2011) [arXiv:1109.1889 [hep-ex]].
- [78] J. A. B. Coelho (MINOS Collaboration), "Search for effects of exotic models in MINOS," (2012), poster presented at the XXVth International Conference on Neutrino Physics and Astrophysics (Neutrino 2012), Kyoto, Japan, June 3-9, 2012.
- [79] A. Aguilar-Arevalo *et al.* [LSND Collaboration], "Evidence for neutrino oscillations from the observation of anti-neutrino(electron) appearance in a anti-neutrino(muon) beam", *Phys. Rev. D* **64**, 112007 (2001) [hep-ex/0104049].
- [80] T. A. Mueller, D. Lhuillier, M. Fallot, A. Letourneau, S. Cormon, M. Fechner, L. Giot and T. Lasserre *et al.*, "Improved Predictions of Reactor Antineutrino Spectra", *Phys. Rev. C* **83**, 054615 (2011) [arXiv:1101.2663 [hep-ex]].
- [81] J. N. Bahcall, P. I. Krastev and E. Lisi, "Limits on electron-neutrino oscillations from the GALLEX Cr-51 source experiment", *Phys. Lett. B* **348**, 121 (1995) [hep-ph/9411414].
- [82] C. Giunti and M. Laveder, "Short-Baseline Active-Sterile Neutrino Oscillations?", *Mod. Phys. Lett. A* **22**, 2499 (2007) [hep-ph/0610352].
- [83] P. A. R. Ade *et al.* [Planck Collaboration], "Planck 2013 results. XVI. Cosmological parameters", *Astron. Astrophys.* (2014) [arXiv:1303.5076 [astro-ph.CO]].
- [84] S.M. Bilenky and S.T. Petcov, *Rev. Mod. Phys.* **59** (1987) 671.
- [85] P. Minkowski, *Phys. Lett.* **B67** (1977) 421; M. Gell-Mann, P. Ramond, and R. Slansky in *Supergravity*, p. 315, edited by F. Nieuwenhuizen and D. Friedman, North Holland, Amsterdam, 1979; T. Yanagida, *Proc. of the Workshop on Unified Theories and the Baryon Number of the Universe*, edited by O. Sawada and A. Sugamoto, KEK, Japan 1979; R.N. Mohapatra, G. Senjanovic, *Phys. Rev. Lett.* **44** (1980) 912.
- [86] M. Fukugita and T. Yanagida, *Phys. Lett.* **B174** (1986) 45.
- [87] A. Morales and J. Morales, *Nucl. Phys. Proc. Suppl.* **114** (2003) 141.
- [88] S.R. Elliot and P. Vogel, *Annu. Rev. Nucl. Part. Sci.* **52** (2002) 115.

- [89] H.V. Klapdor-Kleingrothaus *et al.*, Nucl. Phys. Proc. Suppl. **100** (2001) 309.
- [90] Y. Huang and B. Q. Ma, "Constraints on absolute neutrino Majorana mass from current data", arXiv:1407.4357 [hep-ph].
- [91] M.S. Athar et al., 2006 India-based Neutrino Observatory: Project Report Volume I, <http://www.ino.tifr.res.in/ino/OpenReports/INORReport.pdf>.
- [92] S. Agostinelli et al. " Geant4 - a simulation toolkit", Nucl. Instr. & Meth. in Phys. Res. **A506** (2003) 250-303; <http://geant4.cern.ch/>.
- [93] J.S. Marshall, " A study of muon neutrino disappearance with the MINOS detectors and the NuMI neutrino beam", PhD. Thesis, Univ. of Cambridge (2008).
- [94] E. Wolin and L. Ho, " Covariance Matrices for Track Fitting with the Kalman Filter", Nucl. Instrum. Methods **A329** (1993) 493.
- [95] Super-Kamiokande Collaboration, R. Wendell et al., " Atmospheric neutrino oscillation analysis with sub-leading effects in Super-Kamiokande I, II, and III", *Phys.Rev.* **D81** (2010) 092004, [<http://xxx.lanl.gov/abs/1002.3471>arXiv:1002.3471].
- [96] G. L. Fogli and E. Lisi, "Tests of three flavor mixing in long baseline neutrino oscillation experiments", *Phys.Rev.* **D54** (1996) 3667–3670, [<http://xxx.lanl.gov/abs/hep-ph/9604415>hep-ph/9604415].
- [97] V. Barger, D. Marfatia, and K. Whisnant, "Breaking eight fold degeneracies in neutrino CP violation, mixing, and mass hierarchy", *Phys.Rev.* **D65** (2002) 073023, [<http://xxx.lanl.gov/abs/hep-ph/0112119>hep-ph/0112119].
- [98] R. Gandhi, P. Ghoshal, S. Goswami, P. Mehta, and S. U. Sankar, "Earth matter effects at very long baselines and the neutrino mass hierarchy", *Phys.Rev.* **D73** (2006) 053001, [<http://xxx.lanl.gov/abs/hep-ph/0411252>hep-ph/0411252].
- [99] S. Choubey and P. Roy, "Probing the deviation from maximal mixing of atmospheric neutrinos", *Phys.Rev.* **D73** (2006) 013006, [<http://xxx.lanl.gov/abs/hep-ph/0509197>hep-ph/0509197].
- [100] K. Hiraide, H. Minakata, T. Nakaya, H. Nunokawa, H. Sugiyama, et al., " Resolving theta(23) degeneracy by accelerator and reactor neutrino oscillation experiments", *Phys.Rev.* **D73** (2006) 093008, [<http://xxx.lanl.gov/abs/hep-ph/0601258>hep-ph/0601258].

- [101] R. Gandhi, P. Ghoshal, S. Goswami, P. Mehta, S. U. Sankar, et al., "Mass Hierarchy Determination via future Atmospheric Neutrino Detectors", *Phys.Rev.* **D76** (2007) 073012, [<http://xxx.lanl.gov/abs/0707.1723>arXiv:0707.1723].
- [102] M. Honda, T. Kajita, K. Kasahara and S. Midorikawa, "Improvement of low energy atmospheric neutrino flux calculation using the JAM nuclear interaction model", *Phys. Rev. D* **83**, 123001 (2011) [arXiv:1102.2688 [astro-ph.HE]].
- [103] A. de Gouvea, J. Jenkins, and B. Kayser, "Neutrino mass hierarchy, vacuum oscillations, and vanishing $|U(e3)|$ ", *Phys.Rev.* **D71** (2005) 113009, [<http://xxx.lanl.gov/abs/hep-ph/0503079>hep-ph/0503079].
- [104] S. K. Raut, "Effect of non-zero $\theta(13)$ on the measurement of $\theta(23)$ ", <http://xxx.lanl.gov/abs/1209.5658>arXiv:1209.5658.
- [105] M. Gonzalez-Garcia and M. Maltoni, "Atmospheric neutrino oscillations and new physics", *Phys.Rev.* **D70** (2004) 033010, [<http://xxx.lanl.gov/abs/hep-ph/0404085>hep-ph/0404085].
- [106] G. Fogli, E. Lisi, A. Marrone, D. Montanino, and A. Palazzo, "Getting the most from the statistical analysis of solar neutrino oscillations", *Phys.Rev.* **D66** (2002) 053010, [<http://xxx.lanl.gov/abs/hep-ph/0206162>hep-ph/0206162].
- [107] G. Fogli, E. Lisi, A. Marrone, and D. Montanino, "Status of atmospheric $\nu(\mu)$ — $\nu(\tau)$ oscillations and decoherence after the first K2K spectral data", *Phys.Rev.* **D67** (2003) 093006, [<http://xxx.lanl.gov/abs/hep-ph/0303064>hep-ph/0303064].
- [108] P. Huber, M. Lindner, and W. Winter, "Simulation of long-baseline neutrino oscillation experiments with GLOBES (General Long Baseline Experiment Simulator)", *Comput.Phys.Commun.* **167** (2005) 195, [<http://xxx.lanl.gov/abs/hep-ph/0407333>hep-ph/0407333].
- [109] P. Huber, J. Kopp, M. Lindner, M. Rolinec, and W. Winter, "New features in the simulation of neutrino oscillation experiments with GLOBES 3.0: General Long Baseline Experiment Simulator", *Comput.Phys.Commun.* **177** (2007) 432–438, [<http://xxx.lanl.gov/abs/hep-ph/0701187>hep-ph/0701187].
- [110] M. D. Messier, "Evidence for neutrino mass from observations of atmospheric neutrinos with Super-Kamiokande", (1999).

- [111] E. Paschos and J. Yu, "Neutrino interactions in oscillation experiments", *Phys.Rev.* **D65** (2002) 033002, [<http://xxx.lanl.gov/abs/hep-ph/0107261>].
- [112] **T2K Collaboration**, T. Nakaya, "New results from T2k", 2012. Talk given at the Neutrino 2012 Conference, June 3-9, 2012, Kyoto, Japan, <http://neu2012.kek.jp/>.
- [113] **T2K Collaboration** Collaboration, Y. Itow et al., "The JHF-Kamioka neutrino project", <http://xxx.lanl.gov/abs/hep-ex/0106019>.
- [114] M. Ishitsuka, T. Kajita, H. Minakata, and H. Nunokawa, "Resolving neutrino mass hierarchy and CP degeneracy by two identical detectors with different baselines", *Phys.Rev.* **D72** (2005) 033003, [<http://xxx.lanl.gov/abs/hep-ph/0504026>].
- [115] P. Huber, M. Lindner, and W. Winter, "Superbeams versus neutrino factories", *Nucl.Phys.* **B645** (2002) 3–48, [<http://xxx.lanl.gov/abs/hep-ph/0204352>].
- [116] M. Fechner, "Study of the expected performance of the T2K experiment on $\nu/\mu - \nu/e$ oscillation using data from the K2K experiment" (2006) .
- [117] **T2K Collaboration** Collaboration, I. Kato, "Status of the T2K experiment", *J.Phys.Conf.Ser.* **136** (2008) 022018.
- [118] **NO ν A Collaboration**, R. Patterson, "The no ν a experiment: Status and outlook", 2012. Talk given at the Neutrino 2012 Conference, June 3-9, 2012, Kyoto, Japan, <http://neu2012.kek.jp/>.
- [119] S. K. Agarwalla, S. Prakash, S. K. Raut, and S. U. Sankar, "Potential of optimized NO ν A for large θ_{13} and combined performance with a LArTPC and T2K", <http://xxx.lanl.gov/abs/1208.3644> [arXiv:1208.3644](https://arxiv.org/abs/1208.3644).
- [120] W.Pauli,"Exclusion principle, Lorentz group and reflection of space-time and charge", London, Pergamon Press, 1955
- [121] G.Grawert et al., *Fortschr. Phys.* **7** 291 (1959).
- [122] For a review and a comprehensive and historical list of references on the CPT theorem, see
I. S. Tsukerman, "CPT invariance and neutrino physics", [arXiv:1006.4989](https://arxiv.org/abs/1006.4989) [hep-ph].

- [123] V. A. Kostelecky and S. Samuel, "Spontaneous Breaking of Lorentz Symmetry in String Theory", *Phys. Rev. D* **39**, 683 (1989).
- [124] G. Amelino-Camelia *et al.*, *Nature*, **393**, 763 (1998); D. Sudarsky *et al.*, *Phys. Rev. D* **68**, 024010 (2003); J. Alfaro *et al.*, *Phys. Rev. Lett.* **84**, 2318 (2000).
- [125] M. R. Douglas and N. A. Nekrasov, "Noncommutative field theory", *Rev. Mod. Phys.* **73**, 977 (2001) [hep-th/0106048].
- [126] V. A. Kostelecky, "Gravity, Lorentz violation, and the standard model", *Phys. Rev. D* **69**, 105009 (2004) [hep-th/0312310].
- [127] V. A. Kostelecky and M. Mewes, "Lorentz and CPT violation in neutrinos", *Phys. Rev. D* **69**, 016005 (2004) [hep-ph/0309025].
- [128] R. Abbasi *et al.* [IceCube Collaboration], "Search for a Lorentz-violating sidereal signal with atmospheric neutrinos in IceCube", *Phys. Rev. D* **82**, 112003 (2010) [arXiv:1010.4096 [astro-ph.HE]].
- [129] Y. Abe *et al.* [Double Chooz Collaboration], "First Test of Lorentz Violation with a Reactor-based Antineutrino Experiment", *Phys. Rev. D* **86**, 112009 (2012) [arXiv:1209.5810 [hep-ex]].
- [130] J. S. Díaz, T. Katori, J. Spitz and J. M. Conrad, "Search for neutrino-antineutrino oscillations with a reactor experiment", *Phys. Lett. B* **727**, 412 (2013) [arXiv:1307.5789 [hep-ex]].
- [131] L. B. Auerbach *et al.* [LSND Collaboration], "Tests of Lorentz violation in anti- $\nu(\mu) \rightarrow$ anti- $\nu(e)$ oscillations", *Phys. Rev. D* **72**, 076004 (2005) [hep-ex/0506067].
- [132] A. A. Aguilar-Arevalo *et al.* [MiniBooNE Collaboration], "Test of Lorentz and CPT violation with Short Baseline Neutrino Oscillation Excesses", *Phys. Lett. B* **718**, 1303 (2013) [arXiv:1109.3480 [hep-ex]].
- [133] P. Adamson *et al.* [MINOS Collaboration], "Search for Lorentz invariance and CPT violation with muon antineutrinos in the MINOS Near Detector", *Phys. Rev. D* **85**, 031101 (2012) [arXiv:1201.2631 [hep-ex]].

- [134] B. Rebel and S. Mufson, "The Search for Neutrino-Antineutrino Mixing Resulting from Lorentz Invariance Violation using neutrino interactions in MINOS", *Astropart. Phys.* **48**, 78 (2013) [arXiv:1301.4684 [hep-ex]].
- [135] T. Akiri, "Sensitivity of atmospheric neutrinos in Super-Kamiokande to Lorentz violation", arXiv:1308.2210 [hep-ph].
- [136] D. Mattingly, "Modern tests of Lorentz invariance", *Living Rev. Rel.* **8**, 5 (2005) [gr-qc/0502097].
- [137] D. Casper, "The Nuance neutrino physics simulation, and the future", *Nucl. Phys. Proc. Suppl.* **112**, 161 (2002) [hep-ph/0208030].
- [138] A. Chatterjee, K. K. Meghna, K. Rawat, T. Thakore, V. Bhatnagar, R. Gandhi, D. Indumathi and N. K. Mondal *et al.*, "A Simulations Study of the Muon Response of the Iron Calorimeter Detector at the India-based Neutrino Observatory", *JINST* **9**, P07001 (2014) [arXiv:1405.7243 [physics.ins-det]].
- [139] A. Chatterjee, D. Choudhury, R. Gandhi, P. Mehta, "Testing non standard neutrino matter interactions in atmospheric neutrino propagation", In preparation
- [140] T. Ohlsson, "Status of non-standard neutrino interactions", *Rept. Prog. Phys.* **76**, 044201 (2013) [arXiv:1209.2710 [hep-ph]].
- [141] A. Pilaftsis and T. E. J. Underwood, "Electroweak-scale resonant leptogenesis", *Phys. Rev. D* **72**, 113001 (2005) [hep-ph/0506107].
- [142] K. J. Healey, A. A. Petrov and D. Zhuridov, "Nonstandard neutrino interactions and transition magnetic moments", *Phys. Rev. D* **87**, no. 11, 117301 (2013) [arXiv:1305.0584 [hep-ph]].
- [143] J. R. Bhatt, B. R. Desai, E. Ma, G. Rajasekaran and U. Sarkar, "Neutrino Condensate as Origin of Dark Energy", *Phys. Lett. B* **687**, 75 (2010) [arXiv:0911.5012 [hep-ph]].
- [144] C. Wetterich, "Inflation, quintessence, and the origin of mass", arXiv:1408.0156 [hep-th].
- [145] C. Biggio, M. Blennow and E. Fernandez-Martinez, "General bounds on non-standard neutrino interactions", *JHEP* **0908**, 090 (2009) [arXiv:0907.0097 [hep-ph]].

- [146] P. Huber and J. W. F. Valle, "Nonstandard interactions: Atmospheric versus neutrino factory experiments", *Phys. Lett. B* **523**, 151 (2001) [hep-ph/0108193].
- [147] M. C. Gonzalez-Garcia, M. Maltoni and J. Salvado, "Testing matter effects in propagation of atmospheric and long-baseline neutrinos", *JHEP* **1105**, 075 (2011) [arXiv:1103.4365 [hep-ph]].
- [148] P. Adamson *et al.* [MINOS Collaboration], "Search for flavor-changing non-standard neutrino interactions by MINOS", *Phys. Rev. D* **88**, no. 7, 072011 (2013) [arXiv:1303.5314 [hep-ex]].
- [149] M. C. Gonzalez-Garcia and M. Maltoni, "Determination of matter potential from global analysis of neutrino oscillation data", *JHEP* **1309**, 152 (2013) [arXiv:1307.3092].
- [150] T. Kikuchi, H. Minakata and S. Uchinami, "Perturbation Theory of Neutrino Oscillation with Nonstandard Neutrino Interactions", *JHEP* **0903**, 114 (2009) [arXiv:0809.3312 [hep-ph]].
- [151] P. Coloma, A. Donini, J. Lopez-Pavon and H. Minakata, "Non-Standard Interactions at a Neutrino Factory: Correlations and CP violation", *JHEP* **1108**, 036 (2011) [arXiv:1105.5936 [hep-ph]].
- [152] J. Kopp, M. Lindner, T. Ota and J. Sato, "Non-standard neutrino interactions in reactor and superbeam experiments", *Phys. Rev. D* **77**, 013007 (2008) [arXiv:0708.0152 [hep-ph]].